Advanced tomographic image reconstruction algorithms for Diffuse Optical Imaging

Alejandro Vidal-Rosas

Automatic Control and

Systems Engineering Department

University of Sheffield

A thesis submitted for the degree of

Philosophiae Doctor

Supervisor:

Prof. Daniel Coca

Sheffield, U. K. 2019

Dedicated to

To my wife Yessica and my children Leonardo and Elizabeth, for all the happiness that you brought to this adventure.

To my parents: Elías Vidal Castro and Gloria Rosas Rosete, and to Ernesto, Carmen, Gloria and Alberto, for all the advices that you gave me to growth in my personal and professional life.

Acknowledgements

My gratitude to Professor Daniel Coca, I could not have finish this work without his advice and support during this adventure. Thank you Daniel.

I would like to thank to Doctor Tim Chico and Professor John Mayhew, for considering me in the projects that improved the contributions achieved in this thesis.

To all my dear friends: Pablo, Toñito, Mario, Ariel, Matei, Aldo, Carlos, Miriam, Pepe, Laura, Edgar "El Maza", Rafael "El Robbie", Mandy, Laura, Faedon, Guillermina, Steve, many thanks for all the funny moments, the laughs and the talks that we had. Also to my friends in Mexico: Karina, Melissa, Cinthia and Eder, thank you for your encouragement and your support.

And finally, I want to thank to Luis Alberto, Faby, Maria de la Paz, Lizbeth, Oscar, uncles Sergio and Juan, my aunt Malena and my great-aunt Elisa, she is over 100 years and she is still working hard every day.

Abstract

Diffuse Optical Imaging is relatively new set of imaging modality that use infrared and near infrared light to characterize the optical properties of biological tissue. The technology used is less expensive than other imaging modalities such as X-ray mammography, it is portable and can be used to monitor brain activation and cancer diagnosis, besides to aid to other imaging modalities and therapy treatments in the characterization of diseased tissue, *i. e.* X-ray, Magnetic Resonance Imaging and Radio Frequency Ablation.

Due the optical properties of biological tissue near-infrared light is highly scattered, as a consequence, a limited amount of light is propagated thus making the image reconstruction process very challenging. Typically, diffuse optical image reconstructions require from several minutes to hours to produce an accurate image from the interaction of the photons and the chormophores of the studied medium. To this day, this limitation is still under investigation and there are several approaches that are close to the real-time image reconstruction operation.

Diffuse Optical Imaging includes a variety of techniques such as functional Near-Infrared Spectroscopy (fNIRS), Diffuse Optical Tomography (DOT), Fluorescence Diffuse Optical Tomography (FDOT) and Spatial Frequency Domain imaging (SFDI). These emerging image reconstruction modalities aim to become routine modalities for clinical applications. Each technique presents their own advantages and limitations, but they have been successfully used in clinical trials such as brain activation analysis and breast cancer diagnosis by mapping the response of the vascularity within the tissue through the use of models that relate the interaction between the tissue and the path followed by the photons.

One way to perform the image reconstruction process is by separating it in

two stages: the forward problem and the inverse problem; the former is used to describe light propagation inside a medium and the latter is related to the reconstruction of the spatio-temporal distribution of the photons through the tissue. Iterative methods are used to solve both problems but the intrinsic complexity of photon transport in biological tissue makes the problem time-consuming and computationally expensive.

The aim of this research is to apply a fast-forward solver based on reduced order models to Fluorescence Diffuse Optical Tomography and Spatial Frequency Domain Imaging to contribute to these modalities in their application of clinical trials. Previous work showed the capabilities of the reduced order models for real-time reconstruction of the absorption parameters in the brain of mice. Results demonstrated insignificant loss of quantitative and qualitative accuracy and the reconstruction was performed in a fraction of the time normally required on this kind of studies.

The forward models proposed in this work, offer the capability to run three-dimensional image reconstructions in CPU-based computational systems in a fraction of the time required by image reconstructions methods that use meshes generated using the Finite Element Method. In the case of SFMI, the proposed approach is fused with the approach of the virtual sensor for CCD cameras to reduce the computational burden and to generate a three-dimensional map of the distribution of tissue optical properties.

In this work, the use case of FDOT focused on the thorax of a mouse model with tumors in the lungs as the medium under investigation. The mouse model was studied under two- and three- dimension conditions. The two-dimensional case is presented to explain the process of creating the Reduced-Order Models. In this case, there is not a significant improvement in the reconstruction considering

NIRFAST as the reference. The proposed approach reduced the reconstruction time to a quarter of the time required by NIRFAST, but the last one performed it in a couple of seconds. In contrast, the three-dimensional case exploited the capabilities of the Reduced-Order Models by reducing the time of the reconstruction from a couple of hours to several seconds, thus allowing a closer real-time reconstruction of the fluorescent properties of the interrogated medium.

In the case of Spatial Frequency Domain Imaging, the use case considered a three-dimensional section of a human head that is analysed using a CCD camera and a spatially modulated light source that illuminates the mentioned head section. Using the principle of the virtual sensor, different regions of the CCD camera are clustered and then Reduced Order Models are generated to perform the image reconstruction of the absorption distribution in a fraction of the time required by the algorithm implemented on NIRFAST.

The ultimate goal of this research is to contribute to the field of Diffuse Optical Imaging and propose an alternative solution to be used in the reconstruction process to those models already used in three-dimensional reconstructions of Fluorescence Diffuse Optical Tomography and Spatial Frequency Domain Imaging, thus offering the possibility to continuously monitor tissue obtaining results in a matter of seconds.

Contents

List of Figures

.

List of Tables

Chapter 1

Introduction

The first medical imaging modalities to achieve great success were based on the use of X-rays. Techniques such as projection radiographs and fluoroscopy were extensively used before the advent of the digital computer that allowed the development of imaging modalities such as X-ray Computed Tomography (X-ray CT), Magnetic Resonance Imaging (MRI) and Ultrasound.

Magnetic Resonance Imaging (MRI) uses radio-frequency waves to reconstruct anatomic images based on the different susceptibility properties of tissue. Unlike X-ray imaging that uses dangerous ionizing radiation, MRI use non-ionizing radiation with the disadvantage that a scan can last up to 90 minutes and also patients with pacemakers or metal objects can not be examined. Ultrasound imaging uses high frequency sound waves to visualize internal body structures. Its instrumentation is compact, mobile, inexpensive and exhibits very low risks compared to X-ray that produces ionizing radiation and has the potential risk of harm healthy tissue [1, 2].

The use of light to interrogate tissue is an alternative to the aforementioned imaging modalities, either in the visible or near-infrared spectrum, with the current technology is possible to visualize the interaction of the photons with

biological tissue. Unlike X-rays, photons do not present a straight path in biological tissue and hence light distribution is modelled using sophisticated methods, such as Monte Carlo simulations [3, 4], the Radiative Transfer Equation (RTE) [5], the Diffusion Approximation (DA) [6, 7].

The models used to describe light propagation and the methods used to perform the reconstruction depend on the application, *i.e.* it is not recommended to use the Diffusion Approximation in small samples or void-like mediums due to it is unable to predict light propagation on those mediums. In these cases, Monte-Carlo models and the Radiative Transfer Equation are recommended to be implemented, although the solution is expected to be complex and time-consuming. To solve the limitations imposed by each DOI reconstruction method, hybrid techniques have been proposed such as the radiative-diffusion models proposed by Tarvainen *et. al.*, 2005 [8] and Ren *et. al.*, 2004 [9].

1.1 Introduction to Diffuse Optical Imaging techniques

Over the last three decades, Diffuse Optical Imaging (DOI) techniques have emerged as a new medical imaging modality that provides a cheaper alternative to functional MRI, to aid in the diagnosis and detection of cancer, analyse wounds recovery and develop. It uses harmless Near-Infrared (NIR) light to analyse biological tissue [10, 11, 12]. With the time, Diffuse Optical Imaging techniques has been able to perform complex test such as breast cancer diagnosis and fetal brain activation using spectroscopy and Diffuse Optical Tomography [13]. Furthermore, with the aid of fluorescent markers and bioluminescence it has been possible to understand biological underlying processes from deep tissue [14].

Near-infrared spectroscopy (NIRs) is an imaging technique that is sensitive to tissue function and composition. This technique is used to quantify blood composition, water and adipose content, and epithelial tissue [15]. In principle, NIRs has a poor spatial resolution because it recovers both superficial and internal information. By adding more measurement positions, it is possible to obtain topograms from the areas where the biological activity is occurring and obtain temporal and spatial images of them. This imaging technique is known as NIR topography [16] and it could be considered the base reference to more advanced optical imaging techniques.

Diffuse Optical Tomography (DOT) is an imaging method that enhances the capabilities of NIR topography by spatially quantifying the absorption and scattering optical properties of a medium. Typically, the absorption parameter is used to characterize physiological changes from a specific tissue volume, such as brain activity [17]. This due to the strong dependence of absorption to changes to blood oxygenation [18].

To improve DOT imaging capabilities it is possible to use external fluorescent markers in a technique known as fluorescence diffuse optical tomography (FDOT). In most cases, the fluorescent marker increase the absorption by concentrating it in areas with high vascularity, such as tumoral tissue. In other cases, the marker is excited and the fluorescent reaction is reconstructed such as the studies carried out by Sevick-Muraca&Burch, 1994 [19] and Chang, *et. al.*, 1997 [20] that studied the response of both absorption and re-emitted photons from a fluorescent marker injected into the tissue, furthermore providing mathematical descriptions of the absorption and the fluorescent response.

The advantages that optical imaging methods offer over other imaging modalities are: fast data acquisition, portability, compactness and very significantly, the

technology is non-invasive, which allows in vivo functional imaging of important biological processes such as muscle oxygenation and brain activation, several DOT techniques and applications were compiled in the review offered by Gibson *et. al.*, 2005 [11, 21].

An insight of mathematical models used to successfully simulate light propagation and perform image reconstructions through the software package NIRFAST given by Dehghani, *et. al.*, 2008 [22]; an alternative package to NIRFAST is TOAST++ described in the paper of Schweiger&Arridge, 2014 [23]..Both packages consist of a set of libraries for Finite Element computation and different inverse solvers to perform image reconstructions.

The large set of available Diffuse Optical Imaging technologies and reconstructions techniques allow the visualization of light tissue interactions through the scattering, absorption and fluorescence from endogenous and exogenous tissue elements. These optical properties are used to reveal information of the structure, molecular function, physiology and biochemistry of tissue [24].

Is important to note that NIR light is highly scattered in biological tissue, as a result, light propagation does not follow a straight line from sources to detectors. Therefore, traditional back-projection algorithms, used in CT have limited application. Furthermore, the image reconstruction process is known to be non-linear and ill-posed; consequently, sophisticated reconstruction methods are required [25].

Several approaches have been proposed to model light transport in tissue, such as Monte Carlo simulations [26, 27], the radiative transfer equation (RTE) [28] or the diffusion approximation (DA) [29]. MC and RTE models are considered the most accurate methods to describe light propagation; however,

they are computationally expensive and time-consuming being necessary the use of supercomputer to model light propagation and then perform the image reconstruction from [3, 8].

The diffusion approximation is less computationally demanding than RTE and MC simulations, and it is widely employed for biological tissue image reconstructions [30, 31]. The disadvantage of using DA is that it fails to accurately describe light propagation on small geometries, regions near to the sources and in the presence of void-like domains such as the Cerebrospinal Fluid (CSF) in the brain, or the synovial liquid in finger joints [5].

1.2 Diffuse Optical Tomography

Diffuse optical tomography is a biomedical imaging modality that reconstruct the intrinsic optical properties, such as absorption and scattering, from a highly scattering medium. Rather than using X-rays, magnetic fields or radio waves, DOT uses light to obtain 3D images of the optical properties from deep tissue [32, 29].

Due to the natural optical contrast between abnormal and normal tissue, DOT has a great potential in medical diagnosis areas, for example in oncology and neurophysiology [33, 34, 35]. With the new advances of computational capabilities and progresses made in sensing components, DOT applications have started to spread and to generate other sub-modalities such as High-Density DOT which considers a larger number of sources and detectors that not long ago was not even possible due to technological limitations [36].

As mentioned before, DOT applicability tends to be limited by the computational capabilities that the user accounts for to perform the image reconstruction.

A trade-off between image quality, reconstruction accuracy, size resolution and time is necessary to define prior to start the reconstruction process. For this reason, research groups around the globe actively work in suitable ways to outcome the intrinsic limitations that DOT presents.

1.3 Fluorescence Diffuse Optical Tomography

The use of molecular probes to target biological events made it possible to quantify clinical images with high resolution and specificity [37], ranging from molecular level to whole tissue samples [38]. Moreover, fluorophore interactions with tissue allowed 3D image reconstructions over time, known as four-dimensional imaging [39].

Fluorescence Diffuse Optical Tomography (FDOT) has received particular attention due to the development of fluorescent dyes, enabling non-invasive studies of gene expression, protein interactions and cellular processes with microscopic and molecular resolution levels [40]. FDOT has been used in small animal experiments to monitor the progression of diseases and biological processes [10, 41, 42].

Fluorescence Diffuse Optical Tomography (FDOT) exploits the presence of fluorophores inside a medium. This allows depth biological tissue examination with an enhanced contrast compared to standard DOT [43]. It has been used in brain imaging studies [44, 45] and breast cancer studies [46, 47, 48].

Compared to DOT, the use of a fluorescent marker allowed to improve the signal-to-noise ratio of the background and the absorption parameters. Besides, it exploited other features given by the intrinsic properties of the exogenous markers allowing analyse specific biological interactions. But FDOT shares

similar limitations with DOT related to the performance and time required for reconstructions.

1.4 Spatial Modulated Light Imaging

Spatial modulated light imaging or spatial frequency-domain imaging is a novel approach that can perform fast, wide-field non-invasive spectroscopy and DOT reconstructions. This approach uses spatial frequencies and angular shifts to improve the capabilities of continuous wave illumination sources [49, 50]. This technique offered the advantage to allow the generation of wide-view images due to the use of CCD cameras and wide sources of illumination.

Clinical applications of this imaging method involve tissue characterization to aid monitoring burn wounds [51], assessing vascular abnormalities [52] among other experiments carried out to characterize tissue considering topographic imaging. Planar imaging and look-up tables are normally used to describe depth tissue, with limited information about the precise location of the events investigated, although some attempts to perform 3D reconstruction have been carried out on small animals [53]. and tissue-like models known as "phantoms" [54] with results that demonstrated the clinical applicability of this novel imaging modality.

1.5 Motivation

Diffuse optical imaging techniques have the potential to aid in the detection and monitoring of vascular related diseases and oncology. In addition, optical imaging instrumentation is harmless, portable, easy to use and inexpensive. However, several limitations hinder their clinical application; such as the relatively low spatial resolution and the complex reconstruction process which

is computationally expensive and time-consuming.

The algorithmic approaches to accelerate computation have focused on the use of adaptive meshing schemes [55, 56, 57] and multigrid meshes [58, 59] have been proposed. But these approaches require careful design in the interface tissue regions, making it difficult their application. Alternatively, model reduction schemes have been employed to simplify the high-dimensional simulation models obtained after FEM discretization [60] by using B-splines [61] and wavelets to compress the stiffness matrix [62, 63].

To speed-up the reconstruction time, Vidal-Rosas [64, 65] developed a real-time 3D image reconstruction technique based on the reduced order models approach for Diffuse Optical Tomography. The proposed method generate numerical models based-on information gathered from the target medium. The models make use of signal processing and system identification techniques to create a reduced-order model that describe the light propagation into the tissue.

The reduced-order model generated is loaded into an iterative reconstruction technique, thus the application of reduced order models derived from data to solve the forward and inverse problems in DOT has been demonstrated and validated using both numerical and experimental studies involving complex 3D geometries. The results obtained were similar to those obtained using the standard approach that considers light propagation through a Finite Element Method (FEM) mesh, but in a fraction of the time.

Extending the reconstruction capabilities of the reduced order models method could benefit other optical imaging modalities, such as FDOT where the computational burden is even higher due to the light propagation model used in the image reconstruction process. In order to accurately resolve the fluorescent

properties of a fluorescent marker injected into depth tissue, it is important to first resolve the endogenous optical properties of the target medium. Neglecting these optical properties is possible, but further operations are required to prepare the signals prior to the reconstruction process adding more complexity to the problem.

In the same way, spatial frequency domain imaging (SFDI) require precise models to describe the path followed by the photons inside the tissue but being recorded by the pixels of a CCD camera, thus making it a complex task if we consider that each pixel of the camera is a sensing position. Models that could potentially describe this behaviour could be too complex to solve, thus limiting the applicability of SFDI for real-time three-dimensional reconstructions.

We aim to contribute to overcome the aforementioned limitations by the use of the reduced-order models approach in both optical imaging modalities FDOT and SFDI. The proposed approach is intended to be used in 3D application where the precise location of anomalies, either fluorescent or due to the absorption parameters, from depth tissue is a requirement. In the specific case of SFDI we generate the models considering a virtual sensor technique that is intended to further reduce the complexity without compromising the quality of the image.

1.6 Aims and contributions

The aim of this research project was to develop and apply advanced tomographic image reconstruction algorithms for diffuse optical imaging techniques that reduce the reconstruction time without compromising the quality of the image, the accuracy of the objects reconstructed and further enhance the applicability of this imaging modality.

The main contribution is the development of the reduced-order models (ROM) approach as an alternative light propagation model to typical iterative image reconstruction schemes based on the Finite Element Method that typically consider the mesh of the whole medium to perform the reconstruction. This approach maps directly the optical properties to the measured light which drastically reduces the reconstruction time.

Two diffuse optical imaging modalities were selected for the development of ROM approach: Fluorescence Diffuse Optical Tomography (FDOT) and Spatial Frequency Domain (SFD) imaging. These two imaging modalities are considered emerging techniques with enormous potential in the aid of neurological and oncology studies, as well as in the monitoring of post-surgical procedures and small animal research.

For the FDOT case, the proposed ROM approach is formulated to avoid the coupled diffusion equations used to describe the fluorescent light propagation through biological tissue which require the solution of the endogenous optical properties, thus reducing the reconstruction process by only focusing in the remitted light generated by the fluorescent marker.

To implement the Reduced-Order models approach into SFDI, it was also used the concept of virtual sensor in order to image reconstruct the optical properties of a 3-Dimensional medium using a CCD camera and a spatially modulated light source. The idea behind the virtual sensor considers that several camera pixels can be considered to form a single measuring point. Otherwise, each pixel on the CCD camera works as a measuring position, thus making it too complex to perform 3D reconstruction. The use of the virtual sensor avoids this difficulty, thus aiding another contribution to the present work.

In both cases, the main contributions are in the reduction of the time required for the 3D image reconstruction and that the simplicity of Reduced-Order models can be implemented directly over already existent image reconstruction packages such as NIRFAST.

1.7 Organization and structure of the thesis

The present chapter introduced the motivation and the importance of the research stated in the present work. The remaining chapters are organized as follows:

Chapter 2 depicts the literature review of diffuse optical imaging instrumentation including frequency domain, time-domain and continuous wave. This chapter provides an overview of source-detector configurations available and generally used in optical imaging applications with their advantages and limitations.

Chapter 3 formulates the forward and inverse problems for Diffuse Optical Tomography (DOT) and Fluorescence Diffuse Optical Tomography (FDOT), summarizing the key mathematical models used on light propagation and the algorithms that perform optical image reconstructions. This chapter mainly focuses in the Diffusion Approximation (DA) to the Radiative Transfer Equation (RTE) due to the present work focuses on relatively large tissue volumes for the experiments.

Chapter 4 introduces the method to train a numerical model based on the Reduced-Order Models (ROM) approach for DOT applications using data generated by numerical simulations. The trained model is a simplified representation of how the light propagated through the tissue. The estimated models are then used to perform the image reconstruction of the absorption parameter from an anomaly contained within a highly scattered medium.

Chapter 5 presents the extension of the ROM approach in the reconstruction of anomalies targeted with a fluorescent agent. The numerical model is trained to target the fluorescence from the marker contained within depth anomalies instead of the endogenous absorption parameters of the medium. It is demonstrated the imaging capabilities for reconstructing in a fraction of a time the anomalies embedded within a complex three-dimensional medium.

In Chapter 6 is presented the ROM reconstruction capabilities for the characterization of tissue using a spatial frequency modulated light source and the theory of virtual sensor when using a CCD camera instead of optical fibres. In this case, the numerical model is trained to consider several layers of tissue to further recover the optical properties from depth tissue volume. The target medium is the section of a human head consisting of skin, muscle, bone and then brain. In this case, the successful application of the ROM approach was achieved due to the use of the virtual sensor that further reduced the number of models to be trained.

Chapter 7 provides the conclusions for the thesis which summarizes the benefits that the proposed method has to offer within the Diffuse Optical Imaging field. Specifically its implementation within the NIRFAST package with application in Fluorescence Diffuse Optical Tomography and Spatial Frequency Domain Imaging.

1.8 Published articles and posters

Vidal-Rosas, A., Vidal-Rosas, E.E., Coca, D., Fluorescence image reconstruction of lung tumours in a mouse model, congress paper Innovation Match MX, 6-8 of April, 2016.

Vidal-Rosas, A., Vidal-Rosas, E.E., Coca, D., Fluorescence Diffuse Optical Tomography using Reduced Order Models. Poster for the ACSE symposium 16 of October, 2015.

Vidal-Rosas, A., Vidal-Rosas, E.E., Coca, D., Fluorescence Diffuse Optical Tomography using Reduced Order Models. Poster for the ACSE symposium 28 of November, 2014.

Vidal-Rosas, A., Vidal-Rosas, E.E., Coca, D. Real-time Fluorescence Diffuse Optical Tomography of brain haemodynamics. (In preparation, target journal: Journal of Biomedical Optics).

.

Chapter 2

Diffuse Optical Imaging instrumentation

2.1 Introduction

First clinical studies involving light transillumination were reported by Richard Bright in 1831 for hydrocephalus (build-up of fluid in the brain) and intra-ventricular haemorrhage studies. In 1843, Thomas B. Curling used the same transillumination principle and published a treatise of fluid in testis disease known as hydrocele [21].

Further transillumination studies were performed by Cutler in 1929 who observed breast lesions by projecting light from an electric lamp to the breast [66]. Although it was demonstrated the valuable aid light imaging could offer for clinical diagnosis, this technique was difficult to interpret and it caused overheating on the patient's skin and was later abandoned [67].

Early in the 1970s, technological advances and the use of near-infrared illumination allowed the introduction of diaphanography (light scanning) for optical mammography studies [68]. Later in 1977, Jobsis published the paper that introduced near infrared spectroscopy to study brain oxygenation and haemodynamics [69], thus opening the road to the appearance of a variety of Diffuse Optical

Imaging techniques that ranged from the analysis to microscopic level to whole tissue examinations.

Several optical equipment started to be used for diagnosis and research applications during the 90s [70]. These offered non-invasive, easy examination and cost-effective instrumentation; however, technical limitations, poor resolution and the lack of physical models to describe and quantify light propagation, prevented these devices from reaching clinical practice. But those limitations didn't stop the growing research community in attempting to take optical imaging equipment to clinical applications being mammography [71] and brain imaging [72] the main fields of interest.

Although clinical applications were severely limited, during this decade progresses made in both computational and near-infrared (NIR) technologies [73]. Improved light sources and detectors that enhanced the light generation and measurement process. In the same way, advanced computers gave to researchers the opportunity to implement more demanding algorithms [5, 31, 74].

Besides, researchers explored alternative solutions to simplify light propagation models by understanding the physics that govern the path followed by photons, as an example, Egger *et. al.*, 2010 [75] proposed a set of coupled diffusion equations to model fluorescence-tissue interaction that neglected the intrinsic fluorescence that a highly scattered medium presents, thus reducing the complexity of the light propagation model.

The above mentioned improvements on data collection, and the combination of computers with advanced mathematics and algorithms allowed great advances of Diffuse Optical Imaging (DOI) methods such as functional NIR spectroscopy (fNIRS) by enhancing the analyses wavelength to improve tissue characteri-

zation [76], Diffuse Optical Tomography (DOT) allowing the study of more complex mediums [11] and Fluorescence Diffuse Optical Tomography (FDOT) by developing new fluorophores and instruments to precisely describe re-emission interactions [77, 78].

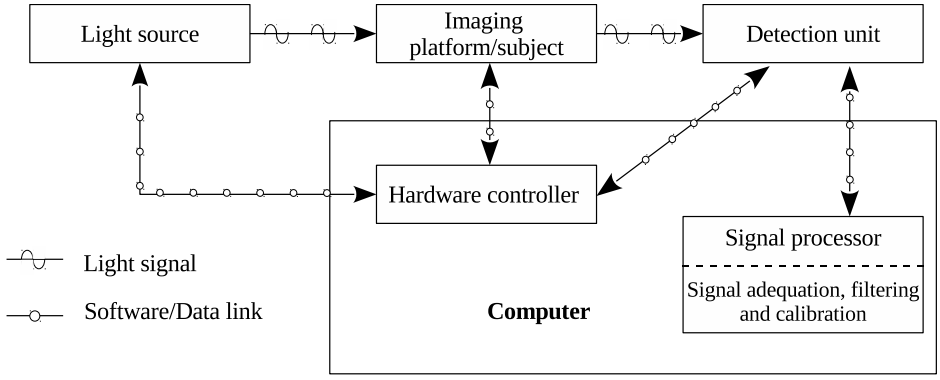

Figure 2.1: Data acquisition for continuous wave instrumentation.

In general, DOI instrumentation consists of an illumination source, a detection unit, an imaging platform, a hardware controller and a signal processor system, as shown in Fig. 2.1. It is widely accepted that the light source, the imaging platform and the detection unit are independent instruments [79]. The signal processor is a system with software capabilities for measurement filtering, calibration, light propagation modeling and image reconstruction algorithms. The hardware controller is either part of the computer or an independent specific instrument [80].

Other design consideration could be used to describe DOI instrumentation, but still the different modules described in Fig. 2.1 are potentially assumed to remain. For instance, if an external hardware controller or the signal processor are outside of the main computer, they still would require signals coming from the computer to match the operation required.

Diffuse Optical Imaging instrumentation can be classified in two ways. The

first class, referred as imaging domains, focuses on the type of illumination source and the corresponding detection method. The second class, defined as geometry measurements, considers the arrays of sources and detectors placed on a target medium regarding the illumination technology used [80].

2.2 Types of Diffuse Optical Imaging Systems

Depending on the type of sources and detectors used to produce intensity measurements and the type of processing applied to the information obtained, DOI instrumentation is classified in three domains: Continuous Wave (CW), Time Domain (TD) and Frequency Domain (FD) systems.

If a system is coupled with another medical imaging modality or is the result of the combination of two optical systems, the obtained instrumentation is called an hybrid optical system, which could offer several advantages but also is expected to increase the complexity and the costs of such implementation.

2.2.1 Continuous Wave systems

Continuous wave systems, or steady-state domain (SSD) systems, use a continuous light source to illuminate a target medium and then measure the transmitted or reflected light intensity. The detected light is attenuated by absorption and scattering events inside the medium. Figure (2.2) shows a schematic of the CW operation.

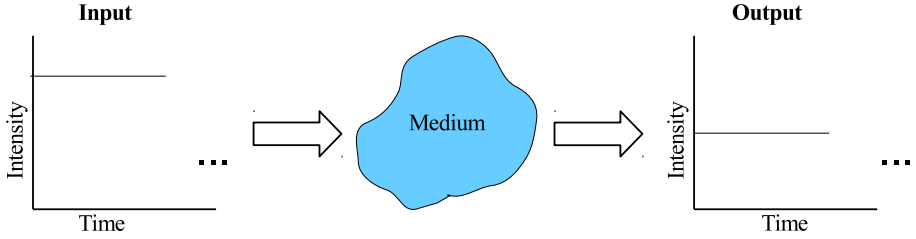

Figure 2.2: Data acquisition for continuous wave instrumentation.

CW instrumentation provides the highest data acquisition rate among DOI systems allowing real-time studies of haemodynamic changes in tissue with high temporal resolution [81]; it is widely used in clinical applications due to its simplicity in terms of its electronics, easier construction and the associated cost is lower, compared with the other two modalities [82, 83].

Limitations associated to CW measurement of intensities are [11]:

- Measurements are more sensitive for tissue immediately below the surface, making it difficult to reconstruct depth tissue, for example, brain image reconstructions are highly contaminated with skin systemic response and also affected by skull thickness and cerebrospinal fluid (CSF) [84, 85].
- Intensity measurements are affected by optode-tissue coupling effects from the presence of hair, skin color variation, changes in position and pressure from the optode against the target medium [11], these two statements are also true for the Frequency Domain (FD) and Time Domain (TD), but due to the additional information it is possible to reduce these effects [86].
- Theoretical studies demonstrated that absorption and scattering parameters can't be decoupled due to cross-talk effects [87], although Pei *et.al.* [88] experimentally found that using a normalized-constraint algorithm and *a priori* information it is possible to separate both coefficients using CW measurements,
- One major limitation of CW instrumentation is the difficulty to perform fluorescence lifetime reconstruction [74], but several alternatives have been proposed such as the introduction of a normalization of the fluorescence with excitation measurements as suggested by Corlu *et. al.* [47].

Theoretical demonstration of the cross-talk effect showed that simultaneous reconstructions of absorption and scattering parameters were not possible using

only intensity information [87]. However, it was demonstrated by Pei *et. al.*, 2001 [88] that this limitation could be overcome by the use of a normalized-constraint algorithm that used relative measurements based on the use of the normalized difference method [89]. The proposed method assumes that the anomalies are small anomalies close to the background values, thus limiting its application to larger anomalies. However, it offered several advantages when a single parameters is targeted, for example: the reconstruction is less sensitive to tissue-probe effects, minimize the impact of quality differences among measurements and inaccurate model considerations.

Despite the above mentioned limitations, CW systems became a powerful and widely used imaging modality, this due to computational advancements and improvements in the reconstruction algorithms such as the use of constrained solutions, incorporation of *a priori* information through regularization and normalization techniques [88]. Besides, its lower cost and reduced complexity allows the development of systems with numerous sources and detectors [90].

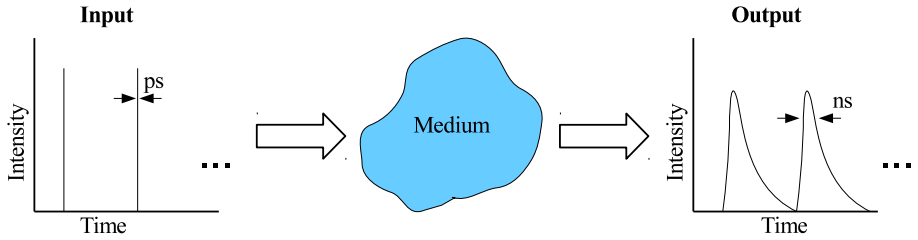

Figure 2.3: Data acquisition for time domain instrumentation.

2.2.2 Time-Domain systems

The temporal point spread function (TPSF) is the distribution of photons from a short duration pulse of light transmitted through a scattering medium [72]. Time-domain (TD) use pulsed light delivered to the medium in the order of picoseconds. After traveling deeper inside the tissue, the TPSF is broadened to

a few nanoseconds before it is measured by the detectors as illustrated in Fig. 2.2.1 [10].

TD systems provide better depth sensitivity and a higher spatial resolution compared to CW systems, due to the capability of TD instrumentation to suppress early arriving photons allowing to exploit the late arriving photons with depth information, opposite to CW instrumentation that only measures the intensity of transmitted/reflected light [91].

By applying a Fourier transform, the TPSF can be converted into the frequency domain (FD), where the amplitude and the phase are the equivalent to intensity and photons time of flight. This conversion is useful in the implementation of simpler image reconstruction techniques due to data types and the FD diffusion equation [92]. However, FD platforms are limited by the number of modulation frequencies used, thus the full content of the time-domain system is not exploited. In consequence, by using the information of higher-order moments of the TPSF improve the quality over FD instruments [93].

Laser technology is frequently used in TD instrumentation because it generates stable and narrow width pulses of light, but they are complex to implement and costly. More recently, the use of commercial high-performance LEDs have increased the interest and the applications of TD systems, due to the simplicity and low cost related to LED technology, compared with laser set-ups [80].

In both cases, the light is measured using a photon multiplier tube (PMT) or for more sensitive applications, multi-channel photon multiplier (MCH-PMT). PMTs/MCH-PMT provide high sensitivity, short rise time and excellent linearity, but also have a complex circuitry, bulky size and noticeable aging effects. Temperature control is required on applications that require PMT to reduce

"black noise" generated by the heat of the PMT and to increase the operation and life-time of the sensing elements.

An alternative to PMT is the avalanche photo-diode (APS), also known as solid-state PMT, which is mainly used in limited space and low power consumption applications, with a trade-off in the sensitivity obtained [80, 94]. Applications that require a high spatial resolution frequently make use of either an intensified coupled charge device (ICCD) or an electron-multiplication CCD (EMCCD) [94].

Time-domain applications that require a high spatial resolution frequently make use of either an intensified coupled charge device (ICCD) or an electron-multiplication CCD (EMCCD). Both ICCD and EMCCD basically consist of an amplification stage that intensifies the detected light that is later passed to a CCD camera which records the enhanced image [94].

First applications of TD systems were in the study of fluorescence reported by Hundley in 1967 [95]. Late in the 1980s, TD systems were used in spectroscopy to estimate concentrations of oxygenated haemoglobin (HbO_2) and de-oxygenated haemoglobin (Hb) [96], also in the estimation of myoglobin by fitting the measured reflectance decay to the Beer-Lambert law [97]. An important contribution from TD systems was demonstrating that the diffusion equation accurate predicts light propagation in a scattering medium [98].

Time-domain systems clinical application include mammography and cancer studies [99, 71, 100], adult brain imaging [101, 102], study of functional infant brain activity [103], fluorescence DOT aiming to improve signal-to noise ratio by reconstructing the emitted time of flight of the fluorescent agent [104, 105, 106] and small animals research for the development of new TD hardware and

algorithms [32]. These applications were related to the study of oxygenated and de-oxygenated blood, but other pilot experiments include the study of main tissue components such as lipid, bone and collagen [107].

The disadvantages related to TD systems are their elevated cost and complex implementation, compared with FD and CW domains [108]. In addition, TD measurements are noisier and exhibit chromatic aberration effects, which is a failure to focus all the light from the same point and is caused by the refractive index of the lens elements that varies with the wavelength. This effect results in further distortion of objects close to the boundaries [31], thus requiring extensive and careful calibrations to obtain accurate reconstructions [93].

Furthermore, PMTs require their own cooling and power supply system, making them cumbersome and increasing their cost. Another limitation is the low measurement speed due to the single-photon counting of photons that requires a large-area, low noise and efficient detectors. Thus limiting the number of clinical and real-time application [90].

2.2.3 Frequency-Domain systems

Frequency domain (FD) instrumentation is a variation of TD technology which acquires data using an amplitude modulated source, in the order of megahertz. Figure 2.4 shows the operation of FD instrumentation that exploits the effects produced by absorbers and scatterers in the amplitude and the phase from the transmitted light through a medium to obtain the optical property distribution.

Temporal resolution of FD reconstructions strongly depends on the frequency chosen, contrary to TD systems that achieve the highest resolution by considering all the available frequencies due to the photon counting capabilities of TD

instrumentation [109]. Whereas TD measurements can be equivalently expressed in the frequency domain, the latter has the advantage that sources and detector are less expensive [11].

Numerical models fitted using FD measurements have a better chance in determining global distributions of absorption and scattering than in a CW case. However, FD is less robust than CW due to its reduced signal-to-noise ratio (SNR) at high frequencies [110]. In the other hand, FD image reconstructions are more straightforward than TD, frequently requiring only one modulation frequency in the measurements for the image reconstruction [41].

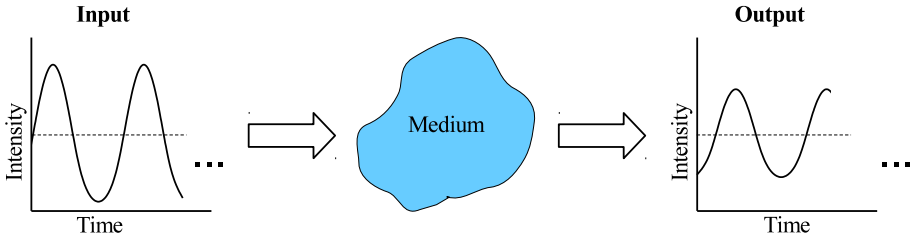

Figure 2.4: Data acquisition for frequency domain instrumentation.

The development of FD instrumentation was possible due to the advances made on fluorescence spectrometers, known as fluorometers [111]. The progress of fluorometers towards tissue spectrometers came after the development of laser technology and techniques for signal processing, allowing the use of the Fast Fourier Transform (FFT) to analyses modulated measurements [112].

After the demonstration that the diffusion equation described light propagation in tissue accurately, analytical solutions in different geometries were obtained and optical properties were calculated by fitting the analytical solution to modulation and phase measurements from tissue-like models (phantoms) and in-vitro experiments [113, 114, 115].

FD systems became popular thanks to the use of LEDs, instead of more

expensive lasers or arc lamps, LEDs offered a wide spectral distribution (from 500nm to 900nm), easy modulation, a stable output, safety (low optical power) and reduced cost [116]. A comparison in the performance of LEDs and lasers showed that both technologies produce similar results with small variations in their baseline and stability [117]. LED technology has revolutionized the way how light is generated and offer a low cost solution to DOI applications that can be rapidly constructed on lab conditions and further passed into a line production, different to laser technology that require certifications and permits that further limit is applicability.

Typically, a modulation frequency of 100 MHz is used in FD instruments, corresponding to the Fourier spectrum of time-domain measurements at one frequency. This operation limits the content information available in FD systems and reducing the quality of the image reconstruction. This limitation can be overcome by using several modulation frequencies, up to at least 1 GHz, which increase the information content of FD instrumentation and becoming comparable to TD systems [118].

Clinical applications of frequency-domain instrumentation include: planar and tomographic optical mammography that improve the visibility of vasculature and breast lesions [119, 120], functional brain imaging ranging from small animals to human adults [35, 121, 122] and fluorescence diffuse optical tomography where FD instrumentation aims to improve the image reconstruction resolution [56, 123, 124]. Frequency domain offer a trade-off between TD and CW instrumentation attracting researchers and commercial investors, but it is still required a high specialization to operate such equipment, also is expensive, compared with CW, thus FD systems are used as a reference more than a front-end application.

2.2.4 Hybrid systems

In order to enhance the capabilities of DOI instrumentation different groups created multi-modal or hybrid systems. These hybrid systems can make use of other imaging modalities such as MRI, X-ray, ultrasound or be a combination of the above DOI domains.

Examples of hybrid systems coupled to other imaging modalities are: fluorescent-ultrasound device used for prostate guided-biopsies [125, 126], fluorescent-MRI equipment developed for *in vivo* atherosclerosis studies, *in vitro* experiments to characterize tissue and to perform small animals studies [127, 128, 129]. Fluorescence DOT has also presented some hybrid systems, as an example, the fluorescence-X-ray system proposed by Ale *et. a.* [130] used to target subcutaneous and lung tumors using high spatial sampling of photons over complete angle projections.

In contrast, examples of hybrid system which combine other domains are a frequency/continuous wave device used for three-dimensional breast imaging, such as the one proposed by Culver *et. al.* [131] that uses a CW system able to operate as a frequency domain, thus adding the capabilities of FD or TD to the simplicity of a CW instrument [132]. Another examples is the FD-CW system proposed by Madsen *et. al.* that offered the capability to study the optical properties of the uterus [133].

These hybrid systems, although more complex with respect to single optical imaging devices, offer the capability to experimentally exploit the physical limits that a single instrumentation or technique has to offer. The strongest use that the research community has with respect to these systems is when they are combined with other medical imaging modalities to obtain more information about tissue

under investigation in a single test, instead of performing separated studies that could change the expected results.

2.3 Diffuse Optical Imaging geometries

In this section, optical imaging is classified considering the source-detector measurement setup used to acquire data measurements referred as the imaging geometry. There are three main categories that can be used to generalize all the possible source-detector arrangements:

- point measurements,
- Topographic mapping,
- Tomographic imaging.

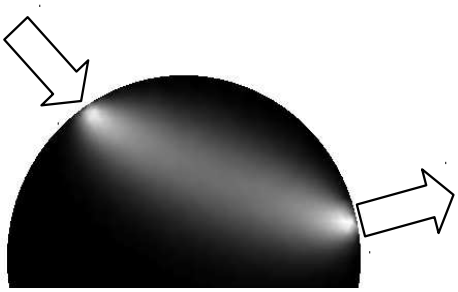

Figure 2.5: Diagram of a single-point measurements set-up in a scattering medium that produce a probability density function (PDF) with a distinctive "banana-shape" profile.

2.3.1 Single-point measurements

This is the simplest system design used to quantify changes in the underlying tissue and involves a single source-detector set-up. Because of the limited number of available measurements, this configuration can not determine the spatial distribution of optical parameters. Figure 2.5 presents a single source-detector pair and the sensitivity of intensity measurements to changes in the absorption coefficient of the medium.

The "banana-shape" structure presented in Fig. 2.5 is the result of changes in the states of photons that propagate through a scattering medium. The position and the likely outcome of these changes can be interpreted as a probability density function (PDF) for the light entering and exiting the medium [134].

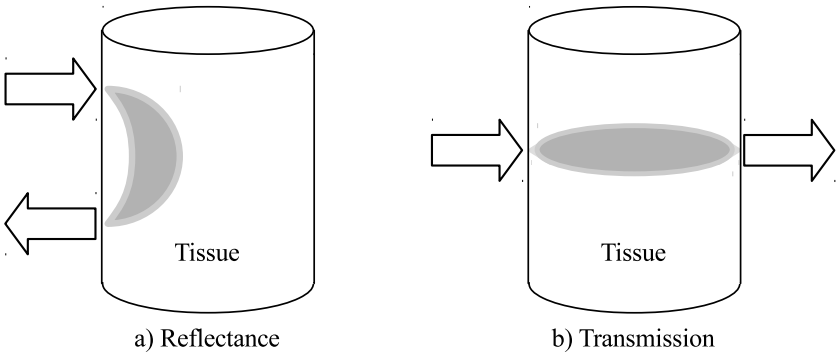

Figure 2.6: Single-point measurement: a) reflectance and b) transmission methods with their corresponding banana-shape structures.

The banana profile strongly depends on the source-detector separation, the shape of the medium and the optical property coefficients. Increased absorption and scattering values, reduce both intensity measurements and penetration depth which affect the quality of a reconstructed image [109].

Single-point measurements are used in near-infrared spectroscopy (NIRS) for the estimation of oxy-haemoglobin and deoxy-haemoglobin concentrations in brain, limbs [17] and breast tissue characterization [15, 135]. In brain studies, the method is referred as functional near-infrared spectroscopy (fNIRS) because it is used for the functional monitoring of brain haemodynamics due to stimuli i.e., visual, motor or somatosensory stimulation [136].

Single point measurements are acquired either by reflection or transmission, as depicted in Fig. 2.6 [17], with a typical source-detector separation of 3cm that allows a light propagation within the tissue of approximately of 1.5cm, which is the half of the distance separation of the source and the detector [137].

In the case of fNIRS, it is recommended an inter-optode separation up to 4.5cm and no less than 2.5cm, this is because brain activity is about 2cm from the surface [136, 138]. Although shorter inter-optode distances have been reported for skin and subcutaneous studies [139].

2.3.2 Topographic mapping

By utilizing an array of multiple optodes in reflectance mode, the optical property distribution of the volume under this array can be mapped. This technique is known as optical topography (OT), or multichannel NIRS [140], because it projects the optical property distribution from multiple source-detector measurements, or channels, onto a two-dimensional (2D) plane.

OT offers a good temporal resolution due to the high data acquisition rate, also near-infrared light depth penetration is approximately the half of the source-detector distance separation [137]. Due to these capabilities, main clinical application are in the imaging of neonatal and adult brain activation [141, 140].

This technique has a low spatial resolution due to source-detector separation and the limited number of available channels [136]. To improve this limitation, different source-detector arrays have been proposed as shown in Fig. 2.7, which illustrates three source-detector configurations used for brain imaging.

Topographic measurements create better maps of optical properties in areas where activation is expected. The grid [142] and rectangular [137] arrays, shown in Fig. (2.7a) and Fig. (2.7b), respectively, have been used in the monitoring of visual, dorsal frontal and inferior frontal cortical areas. The circle arrangement in Fig. 2.7c was reported for imaging human cortex motor stimulation [143]. There exist other source-detector arrangements depending on the tissue under

investigation and the considerations that the research group takes into account for their experiments.

This technique is highly sensitive to optode-tissue coupling variations and requires the calibration of each individual detector. Additionally, problems arise depending on the acquisition protocol, i.e., serial acquisition (one source at a time, all detectors) can produce a spatially varying image and simultaneous acquisition (all sources on) requires information of each source contribution to each detected signal [109].

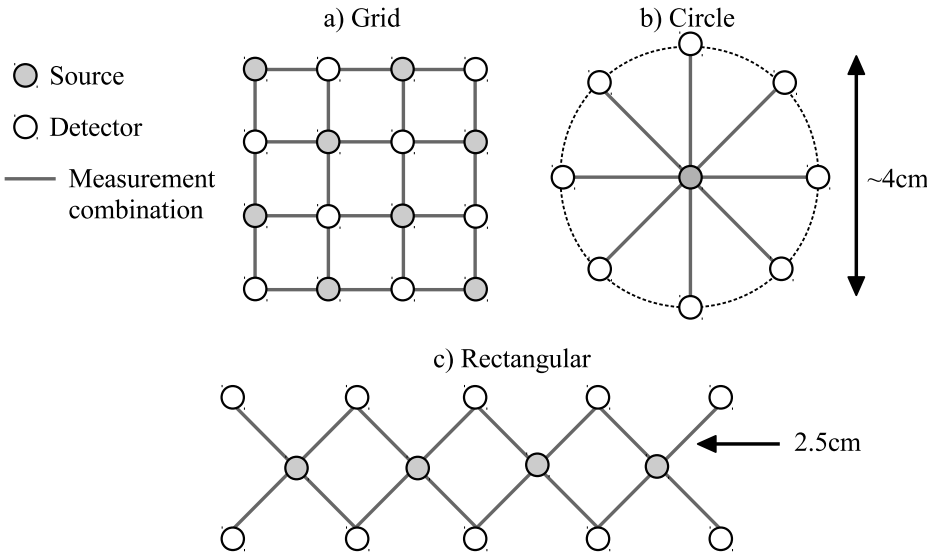

Figure 2.7: Examples of source-detector arrays used for optical topography [142, 143] .

2.3.3 Tomographic imaging

Tomographic techniques utilize source-detector arrays to measure the light that has traveled deep into a medium in order to obtain an image of the optical property distribution. Figure (2.8) presents two of the main tissue geometries used by research groups for producing tomographic images.

The slab geometry, Fig. (2.8a), approximates the volume tissue to a slab or an

infinite half-space and is used for fast image reconstructions. Clinical applications using this geometry are breast diseased tissue characterization [144, 145, 146, 100], cardiovascular studies [147], functional brain imaging and tissue monitoring [148, 149, 84, 150].

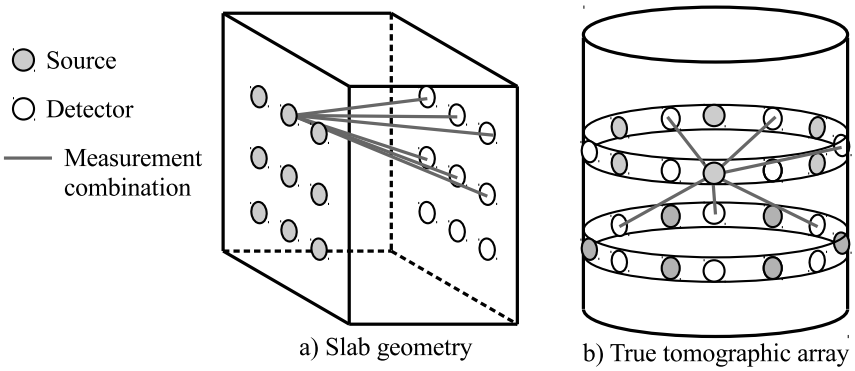

Figure 2.8: Tissue geometries used for tomographic studies of breast and brain tissues.

True tomography, Fig. (2.8b), provides the best spatial resolution by the use of a dense array of probes and overlapping measurement combinations of the sample. However, they are experimentally complex requiring additional probe adjustments and quality assurance of the signals. Clinical applications include brain and breast imaging [151, 152, 153], finger joint studies and small animals research [154, 5, 39].

The accuracy of a tomographic reconstruction depends on the source-detector configuration used to acquire data measurements, despite of the selected geometry. For instance, slab geometries lack depth information from trans-illuminated photons, thus affecting the accuracy of the reconstructed image. Figure (2.9) illustrates the more common source-detector configurations used for both the slab and the tomographic geometries.

A comparison of the effects of these configurations and the quality of the reconstructions is presented in [155]. Systems that utilize all sources to illuminate

simultaneously the medium can acquire data in parallel allowing higher frame rates. However, attenuation effects for distances of 2.5 and 4.5 cm, also detectors require good dynamic range and low noise characteristics [35].

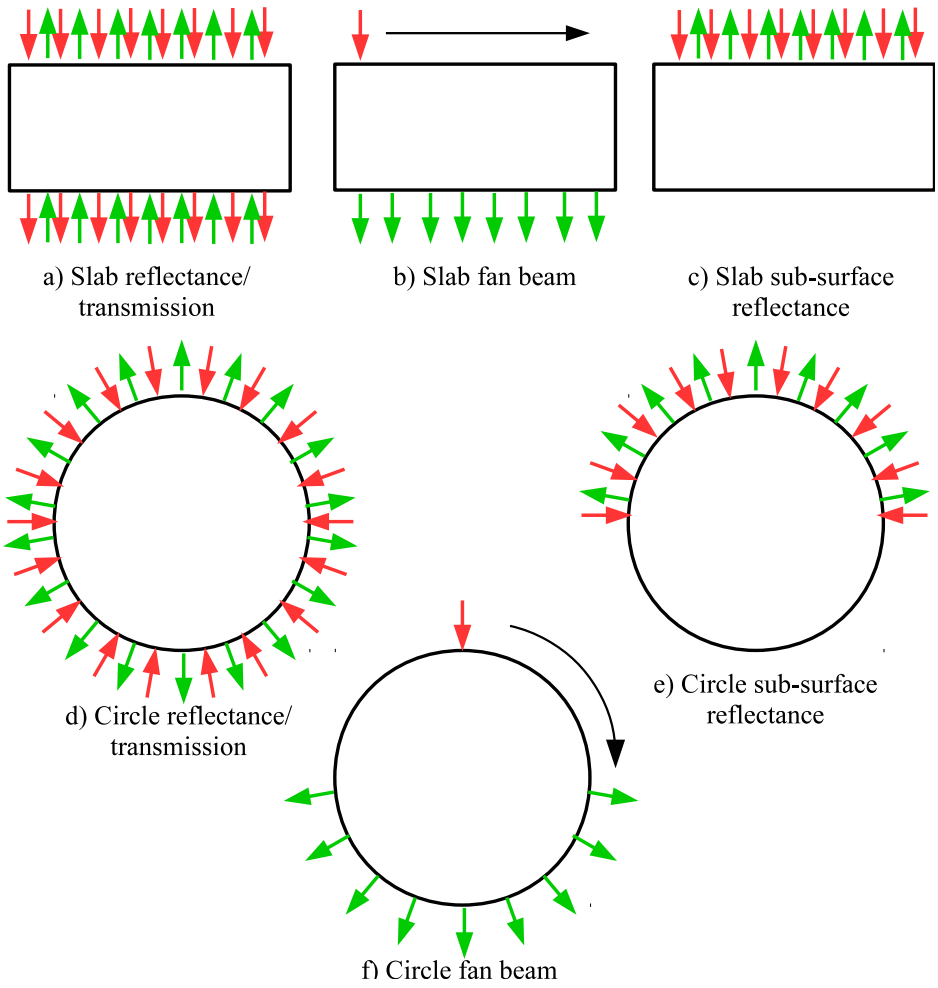

Figure 2.9: Schematic of the different source-detector configurations for the slab and the circle geometries. (a) Slab reflectance/transmission mimics x-ray mammography allowing the use of less sensitive and more stable detectors [131], but tissue characterization requires additional considerations due to lack of symmetry, (b) slab fan beam normally allows the use of CCD cameras which are highly stable and robust, thus providing image with a modest decrease of quality [72], (c) slab sub-surface reflectance is the simplest arrangement and allows the use of analytic reconstruction, but provides the lowest resolution [156], (d) circle reflectance/transmission provides the highest quality image reconstruction and is one of the most used configuration for tomographic imaging being used by several groups to imaging complex volumes [35, 39, 157, 158], (e) circle sub-surface reflectance which is simpler, robust and less expensive, it provides accurate images of tissue sections but has low resolution [82] and (f) circle fan beam is a simplified version of the full reflectance/transmission with a slightly decrease in image quality and has been normally used to experiments on small animals [154, 159, 160].

2.4 Conclusions

The range of diffuse optical imaging instrumentation currently available is a large array of imaging domains, geometries and source-detector configurations that have been successfully used in clinical applications for mammography, brain imaging, monitoring wounds recovery and also in the development of cancer treatments by studies carried out on small animals. Although several of these instruments are still under development, some DOI have reached commercial applications ranging from molecular to organ size studies.

Which system domain between CW, TD and FD is better, there is not a clear answer. CW systems are more affordable and easy to implement, but they lack the sensitivity and spatial resolution that FD and TD systems can provide. But due to the reduced complexity and lower cost that CW offers, this domain has been widely used and improved by using models that better describe light propagation or by being coupled with other imaging modalities. In contrast, TD instrumentation offers the richest information for tissue characterization, but is the more complex and expensive instrumentation to implement. In this sense, FD could be considered the trade-off between cost and information quality, but it is not as widely used as CW instrumentation. The selection of the correct DOI instrument depends on the application, with important consideration in the data type required, the target geometry, detection method, space constrains, reconstruction process, complexity construction and costs.

From the point of view of the author, Continuous Wave has the advantages over the other two modalities due to its simplicity and because the initial investment is not as high as the other two modalities, this modality allows to enthusiast researchers on the field of Diffuse Optical Imaging to have a real feel of

its potential applications. Besides, considering the progresses of the computers, optical devices and the capability to fuse CW with other modalities through software of hardware, improve the chances of further implementation among groups working with other imaging modalities or even research fields other than the clinical applications here mentioned.

Chapter 3

Light transport models and image reconstruction

3.1 Introduction

The mathematical formulation for modeling light propagation is governed by spatial and time scales. The spatial scale goes from Maxwell equations at the microscopic scale, radiative transport equation in the mesoscopic level and the diffusion equation, that neglects the interference effects of wave propagation, at the macro-scale level [161].

To describe light absorption and scattering events in biological tissue is important to consider the main components that affect light propagation: chromophores such as haemoglobin, bilirubin, cytochrome and melanin pigments, porphyrins and exogenous chromophores such as photosensitive markers used for diagnostic and therapeutic trials [162, 163], resulting in that the tissue-light interaction is a complex that requires an correct application of multiple disciplines such as electronics, signal processing, data management, mathematical/statistical modeling and some knowledge of biomedical practices.

Another factor to consider for light propagation within tissue is the range of temporal responses that go from femto/picoseconds (normally studied by TD systems), through nanoseconds for diffuse photon waves (FD systems), to milliseconds (CW systems) that allow less demanding hardware and lower costs and also where most of the relevant physiological responses can be obtained [164].

This chapter provides an overview of the mathematical models used to describe light propagation through biological tissue. Theoretical and numerical methods used to solve the so called forward problem over two- and three-dimensional geometries are depicted. The chapter guides the reader to the main methods used to estimate light propagation and justifies the use of the Diffusion Equation which is solved using the Finite Element Method which is the base for the Reduced Order Models formulation.

3.2 Formulation of the forward problem

The forward problem involves the computation of the photon fluence function, $\Phi(r) \in \Omega$, over a domain of interest Ω and the corresponding measurements, $y(\xi) \in \partial\Omega$, on the boundary $\partial\Omega$ for a given distribution of optical parameters $u(r)$ and light sources $\mathbf{s}(\xi)$.

Considering S source positions $\mathbf{s}_i \in \partial\Omega$ $(i = 1, ..., S)$ and D detector locations $\mathbf{d}_j \in \partial\Omega$ $(j = 1, ..., D)$ that produce a total of $y_{i,j}$ measurements. Then, the forward problem is the relationship between the optical tissue properties and measurements for each source-detector configuration described by

$$y(\vec{i}, j) = P_{i,j}(u(r)) \tag{3.1}$$

where $P(\cdot) : U \rightarrow Y$ is the operator from the space of optical parameters U into the space of measurements Y [12]. A number of approaches have been used in the past to solve the forward problem given by equations Eq. (3.1) is described

in the following sections.

3.2.1 Modeling light propagation using stochastic methods

This kind of models utilize probabilistic algorithms to model light intensity distributions inside a tissue volume. Considering that photon propagation randomly depends on factors such as size and concentration of particles, wavelength and refraction index, then absorption and scattering events can be described using stochastic models and probability density functions.

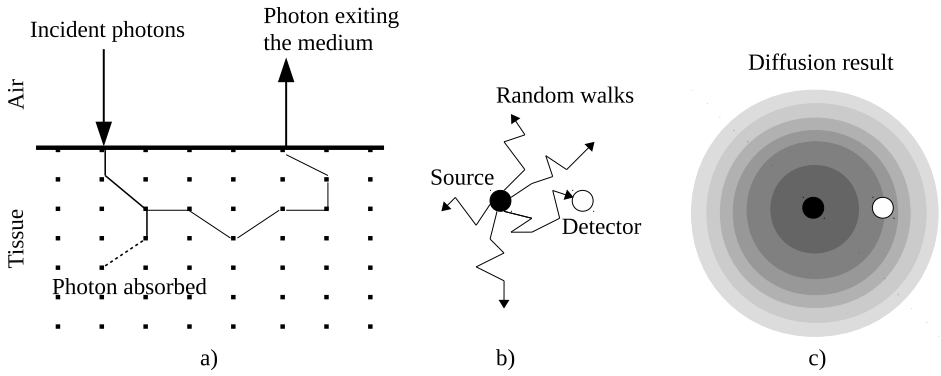

Figure 3.1: Schematic of light propagation considering stochastic methods. a) Example of the random path of photons with absorption and scattering events, b) stochastic processes launched from a source that generates a probability distribution and c) diffusion resulted from a stochastic simulation at $t = t_{end}$

Stochastic models simulate the random path that photons take inside a target medium. Each photon is "traced" as it travels through the medium; at every interacting point the photon is assumed to deposit a fraction of its probabilistic weight, as absorbed energy, to emerge from the interaction with a different weighting factor. The scattering effect is represented by a change in the direction of movement of the photon.

As is shown in Fig. 3.1, after several interactions a photon is either absorbed or it leaves the medium where some of them are measured by a detector. It is necessary to simulate numerous photons in the order of 10^6 to obtain the average

distribution of the photons through the medium [165].

Monte-Carlo (MC) simulation is a stochastic method widely used to solve various physical problems including light propagation through biological tissue. The stochastic model is constructed from the expected values of certain random variables that are equivalent to physical quantities to be determined. The expected values are estimated by averaging multiple independent samples from the random variables introduced [27, 166].

Due to Monte Carlos simulations accurately describe photon propagation through tissue, this approach is used as a reference for validating other approaches, such as light propagation models based on the diffusion equation and the Radiative Transfer Equation [167].

Other stochastic approaches include the Random walk technique that uses a lattice to discretize the medium and a random number algorithm with rules to move from one sampling point to another point [168, 169, 170]. Markov chain models is an stochastic approach which discretizes the medium using pixels and uses a Markov property (probability of moving forward, backward, rightway or leftway) to transition out of the pixel[171]. Stochastic methods are highly accurate, but practical limitations arise due to these require simulating photons in the order of millions to obtain meaningful information to describe light propagation [172].

To allow the use of stochastic solutions, researches started developing methods to accelerate them, for example the use of scaling methods that use baseline simulations that are later scaled to fit a different medium, perturbation MC methods which is similar to the previous one but assumes that optical properties are close to the baseline, hybrid methods that use a diffuse approximation to

reduce the computational load or parallel computation methods that benefit from the advances in computer technology [3].

3.2.2 Analytical methods for modeling light propagation

This approach employs Green's function to solve the diffusion equation (DE) [173], it offers the best description for light propagation in an entire medium, but its application is mostly limited to imaging simple and homogeneous geometries with a single perturbation [174].

Geometries commonly utilized in analytical solutions are: the infinite medium, used for light propagation on phantom and *in vitro* experiments, the semi-infinite medium, employed in topographic imaging [143], and the slab geometry used in layered tissue studies [175].

However, the DE has limitations to describe light propagation with short source-detector separations (typically in the range of 20—40mm) given in the CW configuration. Also, in the TD case: early arrived photons are discarded because DE validity depends on photons that have suffered several scattered events before their measurement.

Analytical solutions have been proposed to overcome DE limitations. Paasschens *et. al.* [176] presented an exact solution to the time-domain RTE using a path-integral method for two and four dimensions and an interpolation for three dimensions. This solution although accurate considered an infinite geometry that was difficult to implement under practical conditions.

As an alternative RTE solution, and taking the work of Paasschens as the starting point, Martelli, *et. al.* [177] proposed an heuristic analytical solution to the RTE for practical applications in the biomedical field. This solution allowed

its application on geometries such as slabs but it is limited to the use of matching liquid to carry out correct measurements.

Theoretically, analytical solutions could be considered an accurate and direct solution to obtain light propagation, but the complexity of biological tissue makes difficult the formulation of analytical solutions.

3.2.3 Describing light propagation using numerical methods

Imaging techniques based on numerical methods have the potential to overcome the limitations that analytical and stochastic models show, with an acceptable balance between the quality and the time required to obtain the light distribution within a medium.

Numerical models are widely used for biological tissue imaging because they are suitable to model light propagation through complex, more realistic geometries and heterogeneous media. Also, they facilitate the combination of near-infrared imaging methods with other clinical imaging systems such as MRI or X-ray, due to the possibility of discretize the latter into meshes that can be used to describe light propagation.

Finite Difference Method (FDM)

This numerical method is used for the solution of Partial Differential Equations (PDE) [178]. The method involves the discretization of the medium using a regular grid where complex geometries are shaped considering the internal points of the grid. Points outside of the desired shape are set to an absorption value in the order of the thousands.

This method has been demonstrated that its results agree in accuracy with other approaches such as Monte Carlo and analytic solution [179]. But due to the simplicity of the Finite Element Method when dealing with complex geometries, the FDM is not to an approach commonly used in DOT applications. Although it has been used to obtain light distributions in human brain [180] and rat's head [181].

Finite Element Method (FEM)

This is one of the preferred methods for solving the diffusion equation (DE) in optical imaging applications. The method projects the PDE into a system of differential equations on finite dimensional space using a set of basis functions, or interpolation functions, on a mesh [182].

It has been used for solving both the RTE and DE models [182, 183, 184]. It is widely use in DOT and FDOT image reconstructions because it enables easy handling of irregular geometries [157].

Finite Volume Method (FVM)

This is a method used to represent and evaluate partial differential equations. Similar to the finite difference and the finite element methods, this method calculate values at discrete places within a meshed geometry. The name of the method comes from the small volume surrounding each node in the mesh [178]

Due to the finite volume method conserve energy in a discrete sense it has been widely used to solve the RTE in optical tomography reconstructions [185, 9]. It offers high degree of mesh adaptation which is useful to model complex geometries; consequently, it is computational demanding [186].

Boundary Element Method (BEM)

It has showed better performance than FEM for large scale geometries [187, 188, 189], but it fails to model light propagation in complex heterogeneous domains due to the complexity of the boundaries found between the interfaces of the tissue [190].

In the following section is introduced the key models used to describe light propagation through biological tissue. Also, is presented the discretization of the diffusion equation using the Finite Element Method discretization, which is the numerical method adopted in this thesis for solving the forward problem.

3.3 Mathematical models of light transport in biological tissue

Light propagation models are representations of the interactions between the light particles and the inhomogeneities of the medium. Any proposed model requires the accurate estimation of changes in the inward, absorbed and emitted energy fluxes and the resulted outward intensities.

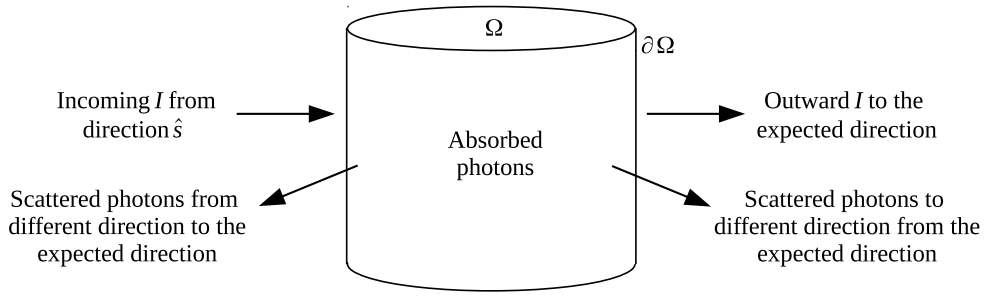

Figure 3.2: Interaction between the light and a scattering medium.

3.3.1 Radiative Transfer Equation

It is widely accepted that light propagation in turbid media can be precisely described by the Radiative Transfer Equation (RTE), also known as Boltzmann equation [12, 191].

In order to describe this model, consider a volume Ω and boundary $\partial\Omega$ centered in $\vec{r} \in \mathbb{R}^n$ (n=2,3), a light package with propagation direction $\hat{s} \in \mathbb{S}^{n-1}$, a time $t \in \mathbb{R}$ and a propagation speed $c \in \mathbb{R}$, as illustrated in Fig. (3.2).

The change of radiance energy $I(\vec{r}, \hat{s}, t)$ in the direction $\hat{s}$ is equal to the loss of energy due to absorption events and scattered light to other directions, plus the inward energy from the scattered light from other directions $\hat{s}'$ and the energy of a light source at position $\vec{r}$ at time $t \in [0, T]$. The energy balance in the time domain can be expressed as

$$\frac{1}{c}\frac{\partial}{\partial t} I(\vec{r}, \hat{s}, t) + \hat{s} \cdot \nabla I(\vec{r}, \hat{s}, t) + (\mu_a + \mu_s) I(\vec{r}, \hat{s}, t) = \mu_s \int_{\mathbb{S}^{n-1}} p(\hat{s}, \hat{s}^{'}) I(\vec{r}, \hat{s}', t) d^2\hat{s}^{'} + q(\vec{r}, \hat{s}, t) \quad (3.2)$$

and in the frequency domain by [9]

$$\frac{i\omega}{c} I(\vec{r}, \omega, \hat{s}) + \hat{s} \cdot \nabla I(\vec{r}, \omega, \hat{s}) + (\mu_a + \mu_s) I(\vec{r}, \omega, \hat{s}) = \mu_s \int_{\mathbb{S}^{n-1}} p(\hat{s}, \hat{s}^{'}) I(\vec{r}, \omega, \hat{s}') d^2\hat{s}^{'} + q(\vec{r}, \omega, \hat{s}) \quad (3.3)$$

where $I(r, \hat{s}, t/\omega)$ is the radiance or angular flux of photons, with units [W $\cdot$ cm^{-1} sr^{-1}], at position r with direction $\hat{s}$ at time t or modulation frequency ω, and $\mathbb{S}^{n-1}$, the unit circle when n=2 or the unit sphere when $n = 3$ [184, 192].

Other parameters in the RTE are the speed of light c, absorption coefficient μ_a and scattering coefficient μ_s, both with units cm^{-1}. $q(r, \hat{s}, t/\omega)$ is the source term and $p(\hat{s}, \hat{s}^{'})$ denotes the scattering phase function, which in DOT, it is usually

given by the Henyey-Greenstein function [157, 193]

$$p(\cos\theta) = \frac{1-g^2}{4\pi(1+g^2-2g\cos\theta)^{3/2}} \quad \text{in} \tag{3.4}$$

where θ is the angle formed between $\hat{s}$ and $\hat{s}'$. g is the anisotropy factor used to characterize the angular distribution of tissue scattering.

From the angular density of photons $I(\vec{r},\hat{s},t)$ it is possible to define two quantities used to describe the behaviour of photons:

- The intensity or photon fluence, $\phi(\vec{r},t)$, in units W $\cdot$ cm $^{-}2$ given by
$$\phi(\vec{r},t) = \int_{\mathbb{S}^{n-1}} I(\vec{r},\hat{s},t)d\hat{s}. \tag{3.5}$$
- The photon current, $\vec{J}$, expressed as $(\vec{r},t)$
$$\vec{J}(\vec{r},t) = \int_{\mathbb{S}^{n-1}} I(\vec{r},\hat{s},t)\hat{s}d\hat{s}, \tag{3.6}$$
the photon current is the physical quantity measured at the tissue surface with units W $\cdot$ cm $^{-}2$ [5].

The RTE ignores the electromagnetic and particle properties from the light, but it is sufficient accurate to to model light propagation through small geometries and low scattering regions such as the cerebrospinal fluid. However, it is difficult to solve in complex geometries and the time required can be equivalent as solving a MC simulation [194].

3.3.2 Diffusion Approximation to the Radiative Transfer Equation

The Diffusion Approximation (DA) to the RTE can be obtained from Eq. (3.3) by assuming a scattering function $f(\hat{s},\hat{s}')$ independent of the absolute angle, slow changes in photon flux and an isotropic source [12, 11, 109]. In the frequency domain it is given by

$$-\nabla\cdot\kappa(r)\nabla\phi(r,\omega)+\mu_a(r)\phi(r,\omega)+\frac{i\omega}{c}\phi(r,\omega)=q_0(r,\omega) \tag{3.7}$$

where $\phi(r,\omega)$ is the photon density at position r and direction $\hat{s}$, μ_a is the absorption coefficient. The diffusion coefficient is $\kappa = \frac{1}{3(\mu_a + \mu_s^{'})}$ where $\mu_s^{'} = \mu_s(1-g)$ is the reduced scattering coefficient that indicates the probability form for the photon diffusion, μ_s the scattering coefficient and g is the anisotropic factor.

Typical values found in biological found in biological tissue are $5 < \mu_s^{'} < 20\ cm^{-1}$, $0.01 < \mu_a < 1\ cm^{-1}$ and $0.7 < g < 0.9$ [195]. The reciprocal of $\mu_s^{'}$ is the transport mean free path (mfp) and represents the distance that a photon can travel before losing all information regarding its entry direction.

The diffusion approximation predicts accurately light propagation for tissue thickness greater than 10 mfp and $\mu_a/\mu_s^{'} << 1$ [17]; however, it fails to accurately describe photon transport in regions close to sources, detectors, boundaries, regions with low scattering and low absorption values, and void-like regions such as cerebrospinal fluid [181].

3.3.3 Boundary conditions

The Robin boundary condition (RBC), also referred as partial-current or Type III boundary condition, is the most widely boundary condition used in DOI. It represents the physical model of a non-scattering medium (air) surrounding the media and models the optical fluence at point ξ in the boundary $\partial\Omega$ on which some fraction of the fluence exits and does not return.

The RBC is given by [183]

$$\phi(\xi) + 2A(\hat{s})\kappa(\xi) \cdot \nabla\phi(\xi) = 0, \qquad \xi \in \partial\Omega \tag{3.8}$$

where $(\hat{s})$ is the unit vector normal to the surface and A is the refractive mismatch coefficient which accounts for the air-tissue contact.

There are two algorithms to calculate parameter A in Eq. (3.8). Based on Fick's law, Groenhuis *et al.* [196, 197] derived the expressions

$$R \approx -1.4399n^{-2} + 0.7099n^{-1} + 0.6681 + 0.0636n \tag{3.9}$$

$$A = \frac{1+R}{1-R} \tag{3.10}$$

where n is the refractive index of the medium. The refractive index at the external boundaries is generally assumed to be equal to free space, then $n_2 = n_{air} = 1$ [22].

Based on Fresnel's laws, Keijzer *et al.* [198] derived a solution given by

$$A = \frac{\frac{2}{1-R_0} - 1 + |\cos\theta_c|^3}{1 - |\cos\theta_c|^2} \tag{3.11}$$

where $\theta_c = \arcsin n_1/n_2$ is the angle of total internal reflection for photons moving from a region with refractive index n_1 to a region with refractive index n_2 and

$$R_0 = \frac{(n_1/n_2 - 1)^2}{(n_1/n_2 + 1)^2}. \tag{3.12}$$

Considering a refractive index $n_1 = 1.4$ for biological tissue [199, 200], it is obtained $A_G = 3.25$ and $A_K = 2.74$ for the Groenhuis and Keijzer approaches, respectively. Farrel *et al.* [201] compared both algorithms and found that the Groenhuis method is slightly more accurate than the Keijzer method.

Exist other boundary conditions, such as the Dirichlet boundary condition (Type I) that specifies the field Φ at an extended surface on the medium and the Neumann Boundary Condition (Type II) that defines the flux at the boundary as $-D\nabla\Phi\cdot\hat{n}$ [183]. Both of these conditions are mathematically simple to implement, but they are less realistic than the RBC [202].

The zero boundary condition, that equals to zero the total diffuse flux inwardly directed at the surface by not considering reflection effects, and the

extrapolated boundary condition in which the diffuse intensity is equal to zero at an extrapolated boundary outside the turbid medium are other boundary conditions used to describe light on the boundary of the medium [7, 203].

Hielscher *et. al.* [204] studied the importance of a good choice of boundary conditions and stated that the partial-current and the extrapolated boundary conditions presented a close agreement between their results. On the contrary, the ZBC although been the simplest to implement is physically incorrect.

3.3.4 Modelling sources and detectors

The source term q_0 in the DE is considered isotropic, which means it is independent from the direction of $\hat{s}$, and there are two strategies for modelling it [199]:

i *Collimated source* (CS): It models a collimated beam pencil produced by an isotropic point source located at $d = 1/\mu_s^{'}$ below the surface as [201]

$$q_0(r) = q\delta(r - r_0) \tag{3.13}$$

where q_0 is the intensity of the δ-shaped source located at point r_0. A CS produces accurate results at large mfp distances from the source (i.e. distances $>$ 0.5cm typically).

ii *Diffuse source* (DS): It describes a diffuse photon current illuminating the boundary segment $\partial\Omega_{DS} \subset \partial\Omega$ where the source is located. It can be incorporated directly into the boundary condition as [191]

$$\phi(\xi) + 2A\hat{\mathbf{n}}\kappa(\xi) \cdot \nabla\phi(\xi) = -4q_s w(\xi) \tag{3.14}$$

where q_s is the source intensity, w is a weighting function and $\hat{\mathrm{n}}$ is the outward normal at $\xi \in \partial\Omega$.

Considering a collimated source with RBC and $\omega = 0$, Eq. (3.7) is reduced to

the continuous wave diffusion equation

$$-\nabla \cdot \kappa(r)\nabla\phi(r) + \mu_a(r)\phi(r) + \phi(r) = q_0(r) \quad r \in \Omega \tag{3.15}$$

$$\kappa(\xi)\frac{\partial\phi(\xi)}{\partial\hat{\mathbf{n}}} + \frac{1}{2A}\phi(\xi) + \frac{1}{2A}\phi(\xi) = 0 \quad \xi \in \partial\Omega \tag{3.16}$$

where $\hat{\mathbf{n}}$ is the normal normal vector to the surface at the $\partial\Omega$. Assuming a refractive index $n_1 = 1.4$ for photon migration at the air-tissue interface [205, 200, 206], it is found $A = 3.25$ using the Groenhuis algorithm.

The operator that describes detector measurements is given by [207, 208, 201]

$$\Gamma(\xi) = -\kappa(\xi)\hat{\mathbf{n}} \cdot \nabla\phi(\xi) \tag{3.17}$$

this equation is also known as the Fick's law and relates the measurable outward flux Γ to the photon density ϕ inside the medium[209].

3.3.5 Solution of the diffusion equation using the Finite Element Method

The Finite Element Method (FEM) is the most commonly numerical technique used for the solution of the DE in diffuse optical imaging. This section introduces the basis to one of the key approaches used on this work and in the diffuse optical imaging methodology.

As stated in Section 3.2.3 there exist other numerical methods, but FEM offers a good trade-off between flexibility to describe complex geometries and computational implementation with several programs used to generate FEM meshes with biomedical applications such as ScanIP-FE [210], COMSOL multiphysics [210, 211] and NIRFAST [22].

It consists of a continuous domain Ω discretized into E finite number of non-overlapping elements joined by N vertex nodes. The weak form of the Galerkin

method is used to solve Eq. (3.15) and proceeds as follows. A solution for ϕ exists if exists a solution for

$$\int_{\Omega} \Psi(r) \left\{ \nabla \cdot \kappa(r) \nabla - \mu_a(r) c - \frac{\partial}{\partial t} \right\} \phi(r,t) d\Omega = - \int_{\Omega} \Psi(r) q_0(r,t) d\Omega \tag{3.18}$$

where Ψ is a function from a test space that satisfies the same boundary condition of ϕ. By integrating Eq. (3.18) by parts

$$\begin{aligned} \int_{\Omega} \kappa(r) \nabla \Psi(r) \cdot \nabla \phi(r) + \mu_a(r) \Psi(r) \phi(r) d\Omega \\ = \int_{\Omega} \Psi(r) q_0(r) d\Omega + \int_{\partial\Omega} \Gamma(r) \Psi(r) d(\partial\Omega). \end{aligned} \tag{3.19}$$

By assuming that Ψ and all its first derivative are integrable over Ω, Eq. (3.19) can be solved considering that the photon fluence $\phi(r)$ and the outward flux Γ can be approximated with the piece-wise polynomial functions

$$\mathbf{\Phi}^h(r) = \sum_{j=1}^{N_{int}} \phi_j \psi_i(r) \tag{3.20}$$

$$\mathbf{\Gamma}^h(r) = \sum_{j=1}^{N_{bnd}} \Gamma_j \psi_i(r) \tag{3.21}$$

where ψ_j are known basis functions. Further, the formulation in Eq. (3.21) only considers the ψ_j centred on boundary nodes ordered as $j = 1, 2, ..., N_{bnd}$.

Then, the weak formulation is given by

$$\begin{aligned} \int_{\Omega} \kappa(r) \nabla \psi_j(r) \cdot \nabla \mathbf{\Phi}^h(r) + \mu_a(r) \psi_j(r) \mathbf{\Phi}^h(t) d\Omega \\ = \int_{\Omega} \psi_j(r) q_0(r) d\Omega + \int_{\partial\Omega} \psi_j(r) \mathbf{\Gamma^h(r)} d(\partial\Omega) \end{aligned} \tag{3.22}$$

that can be expressed in matrix form as

$$[\mathrm{K}(\kappa) + \mathrm{C}(\mu_a)] \mathbf{\Phi} = \mathrm{Q} + \beta \tag{3.23}$$

with entries

$$\mathbf{K}_{i,j} = \int_{\Omega} \kappa(r) \nabla \psi_j(r) \cdot \nabla \psi_i(r) d\Omega \tag{3.24}$$

$$\mathbf{C}_{i,j} = \int_{\Omega} \mu_a(r) \psi_j(r) \psi_i(r) d\Omega \tag{3.25}$$

$$\mathbf{Q}_{i,j} = \int_{\Omega} \psi_j q_0(r) d\Omega \tag{3.26}$$

$$\beta_i = \int_{\partial\Omega} \psi_j(r)\Gamma(r)d\partial\Omega \tag{3.27}$$

$$\mathbf{\Phi} = [\Phi_1, \Phi_2, ..., \Phi_N]^T \tag{3.28}$$

where $i, j = 1, 2, ..., N$ and N is the number of nodes in the FEM mesh.

The matrices have been chosen to have limited support. Thus, matrices K and C are sparse matrices since they have non-zero entries where N_i and N_j are vertices of the same element. Matrix β has non-zero entries where a node is on the boundary $\partial\Omega$, these nodes are termed as *boundary nodes*, N_{bnd} and the remaining are the *internal nodes* N_{int} [202].

FEM mesh resolution is important in the solution of both the forward and inverse problems. Normally, dense meshes (high number of nodes) are used to solve the forward problem in order to obtain numerical accuracy of light propagation. Yalavarthy *et. al.* [212, 213] investigated the impact that the number of nodes and showed that high resolution meshes provide the most accurate and numerically stable solutions.

Inverse meshes are coarse (low number of nodes) and are designed to reduce the number of unknowns, but they need to be designed with enough nodes in order to produce good resolution. Yalavarthy *et. al.* [212] demonstrated that 2,000 nodes provide a good trade-off between mesh resolution and computation time for DOT imaging.

For practical Finite Element Method (FEM) implementation, in this work is used the software NIRFAST (Near Infrared Fluorescence and Spectral Tomography), developed at Dartmouth College and University of Birmingham, dedicated to DOI medical applications. It contains a set of toolboxes for Diffuse Optical Tomography (DOT), Fluorescence DOT and NIR spectroscopy [214, 22].

A detailed explanation of FEM discretization and conditions required to perform it is out the scope of this work, but in the work presented by Medina-Vazquez [215] can be found the discretization of the diffusion equation to its FEM representation. This could be used as a starting point to propose a different FEM discretization by analysing the limitations of the basis function used on the study.

3.4 Light transport model for Fluorescence Diffuse Optical Tomography

Fluorescence Diffuse Optical Tomography (FDOT) is an emerging image modality which uses excitable fluorescent dyes. The emitted light from the fluorophores is measured and then the spatio-temporal distribution of the fluorescent bolus is reconstructed [216].

Calculation of fluorescence light transport in tissue requires the solution of the following coupled diffusion equations [43, 75, 217]

$$-\nabla\cdot[\kappa_x(r)\nabla\phi_x(r,\omega)]+\left[\mu_{ax}(r)+\mu_{af}(r)+\frac{i\omega}{c}\right]\phi_x(r,\omega)=-q_0(r,\omega) \quad (3.29)$$

$$-\nabla\left[\kappa(r)\nabla\phi_{fl}(r,\omega)\right]+\left[\mu_{am}(r)+\frac{i\omega}{c}\right]\phi_{fl}(r,\omega)=\phi_x(r,\omega)\eta\mu_{af}(r)\frac{1-i\omega\tau(r)}{1+[\omega\tau(r)]^2} \quad (3.30)$$

where subscripts x and m indicate the excitation λ_x and emission λ_m wavelengths [nm], respectively, and fl is the fluorescence emission at λ_m $\phi_{x,fl}(r,\omega)$ are the fluence rates, $q_0(r,\omega)=q\delta(r-r_0)$ is the source term with intensity q and $\delta(r-r_0)$ the Dirac function at point r_0, ω is the modulation frequency, $\mu_{a(x,m)}$ the absorption coefficient and the diffusion equation is given by [75]

$$\kappa_{x,m}=\frac{1}{3(\mu_{a(x,m)}+\mu_{af}+\mu_{s(x,m)}^{'})} \quad (3.31)$$

where $\mu_{s(x,m)}^{'}=\mu_s(1-g)$ is the reduced scattering coefficients, $\mu_{s(x,m)}$ is the scattering coefficient and g is the anisotropy factor.

The fluorescent parameters are the fluorophore absorption coefficient $\mu_{af}(r)$, the lifetime τ and the fluorescent yield $\eta\mu_{af}(r)$ which incorporates the fluorophore quantum efficiency

$$\eta = \frac{\text{number of photons emitted}}{\text{number of photons absorbed}}.$$

The fluorophore quantum efficiency η depends on the type of fluorescent agent used, the chemical environment and the fluorophore absorption. The latter parameter depends on the fluorophore concentration

$$\mu_{af} = 2.3\varepsilon C_f \tag{3.32}$$

where ε is the extinction coefficient with unit [μM^{-1} mm^{-1}] and C_f is the concentration of the fluorophore inside the medium in [μM] [217, 208].

The term $(1 - i\omega\tau(r))/(1 + [\omega\tau(r)]^2)$ on the right hand side of Eq. (3.30) was derived from the Fourier transformation of a single exponential decay defined by

$$F(t) = F_0 \frac{1}{\tau} e^{t/\tau} \tag{3.33}$$

where $F_0 = C_f(r)\eta$ is the initial fluorescent bolus with concentration C_f at position r [108, 98]. The absorption coefficients in Eq. (3.29) and Eq. (3.29) are assumed to be different at the excitation and emission wavelengths, due to the tissue chromophore spectral absorption dependence [206].

The continuous wave form of the fluorescence diffusion equation is derived by assuming $\omega = 0$ in Eq. (3.29) and Eq. (3.30), this is expressed as

$$-\nabla \cdot \kappa_x(r)\nabla\phi_x(r) + [\mu_{ax}(r) + \mu_{af}(r)]\phi_x(r) = q_0(r) \tag{3.34}$$

$$-\nabla\kappa_m(r)\nabla\phi_{fl}(r) + \mu_{am}(r)\phi_{fl}(r,\omega) = -\phi_x(r,\omega)\eta\mu_{af}(r), \tag{3.35}$$

where the last term in Eq. (3.30) is neglected; as a result, CW measurements cannot reconstruct the fluorescence lifetime τ.

3.4.1 Simplified fluorescence transport model

The coupled partial differential equations given by Eq. (3.29) and Eq. (3.30) accurately describe the interaction of light, tissue and the presence fluorescent effects at both wavelengths. The problem with this model is presented when is required a discretization due to the coupling effects of the fluorescent parameters.

One solution is by considering the fluorophore concentration C_f to be sufficiently small, then, it is possible to neglect its effects on the diffusion equation. With this assumption, the diffusion coefficient in Eq. (3.31) is reduced to

$$\kappa_{x,m} = \frac{1}{3(\mu_{a(x,m)} + \mu^{'}_{s(x,m)})}. \tag{3.36}$$

By neglecting C_f contribution in Eq. (3.29) and considering Eq. (3.36), the excitation field ϕ_x becomes independent from the concentration. Therefore, the fluorescent diffusion equation for the CW case is reduced to

$$-\nabla\kappa_x(r)\nabla\phi_x(r) + \mu_{ax}(r)\phi_x(r) = q_0(r,\omega) \tag{3.37}$$

$$-\nabla\kappa_m(r)\nabla\phi_{fl}(r) + \mu_{am}(r)\phi_{fl}(r) = \phi_x(r)\eta\mu_{af}(r), \tag{3.38}$$

that produces accurate light propagation calculations and also facilitates the treatment of the inverse problem [218].

Boundary condition and fluence measurements in FDOT

The RBC in the fluorescent case considering is given by [219, 55]

$$\phi_x(\xi,\omega) + 2A\hat{\mathbf{n}}\cdot\kappa_x(\xi)\nabla\phi_x(\xi,\omega) + q_0(r,\omega) = 0 \tag{3.39}$$

$$\phi_m(\xi,\omega) + 2A\hat{\mathbf{n}}\cdot\kappa_m(\xi)\nabla\phi_m(\xi,\omega) = 0 \tag{3.40}$$

where the parameters are equivalent to those formulated in Eq. (3.8) for DOT. The term $q_0(r)$ in Eq. (3.39) accounts for the excitation light source at the boundary.

The outward flux is computed using the Fick's law [207, 208, 201]

$$\Gamma_{x,m} = -\kappa_{x,m}\hat{\mathbf{n}} \cdot \nabla\phi_{x,m}(\xi). \tag{3.41}$$

As mentioned before, the NIRFAST software package was used to solve Eq.(3.37), Eq. (3.38) and Eq. (3.41). The main computation steps involved in solving the excitation and emission equations are as follows: [219, 220]

1. Calculate light propagation using Eq. (3.37) with light source and optical properties at the excitation wavelength λ_x.
2. Determinate the fluorescence photon field by solving Eq. (3.38) with optical properties at the emission wavelength at λ_m and the excitation photon field as the source.
3. Estimate boundary light measurements using Eq. (3.41).

3.4.2 Finite Element Method formulation for FDOT

The FEM formulation for FDOT light propagation is obtained by approximating $\phi_{x,fl}$ by the piecewise continuous polynomial function $\phi^h_{x,fl} = \sum_{j=1}^{N} \phi_{x,fl}\psi_j$. Then, the FDOT coupled diffusion equation can be expressed as

$$(\boldsymbol{K}_x(\kappa) + \boldsymbol{C}_x(\mu_{ax}) + \boldsymbol{F}_x)\,\boldsymbol{\Phi}_x = \mathbf{Q}_0 \tag{3.42}$$

$$(\boldsymbol{K}_m(\kappa) + \boldsymbol{C}_m(\mu_{am}) + \boldsymbol{F}_m)\,\boldsymbol{\Phi}_{fl} = -\boldsymbol{Q}_m \tag{3.43}$$

where the entries for the matrices are

$$\begin{aligned}
\boldsymbol{K}_{(x,m)_{i,j}} &= \int_\Omega \kappa_{x,m}(r)\nabla\psi_i(r) \cdot \nabla\psi_j(r)d\Omega \\
\boldsymbol{C}_{(x,m)_{i,j}} &= \int_\Omega \mu_{a_{x,m}}(r)\nabla\psi_i(r) \cdot \nabla\psi_j(r)d\Omega \\
\boldsymbol{F}_{(x,m)_{i,j}} &= \frac{1}{2A}\int_{\partial\Omega} \nabla\psi_i(r) \cdot \nabla\psi_j(r)d\partial\Omega
\end{aligned} \tag{3.44}$$

with the source vector

$$\boldsymbol{Q}_0 = \int_\Omega \nabla\psi_i(r)q_0(r)d^n r. \tag{3.45}$$

where the excitation source term is defined as a Gaussian distribution in order to match the optical fibre at the source-tissue coupling point.

By assuming an isotropic source located one mfp inside the medium, the fluorescence source at the emission wavelength is given by

$$\boldsymbol{Q}_{m_i} = \int_{\Omega} N_i(r)[\phi_x(r)\eta\mu_{af}(r)] \tag{3.46}$$

distributed throughout the domain.

Detailed information about the FEM discretization above presented can be found in:

- The work of Schweiger *et. al.* 1993 [182] presents the solution of the Diffusion Equation on time-domain using the Finite Element Method (FEM) through piecewise-linear basis functions and the Galerkin method for its implementantion. The proposed numerical solution is further used in a modified Newton-Raphson approach to perform the reconstruction.

- In a later contribution from Schweiger *et. al.* 1995 [199] is analyzed the FEM approach considering boundary effects by refining the mesh close to it and comparing different boundary conditions by extending the work made by Farrel *et. al* 1992 [201]. A further analysis is made to the use of collimated and diffuse sources and how to model these in a numerical based model.

- Davis *et. al.* 2007 [219] presented the discretization of the fluorescent diffusion equation under a frequency domain framework expressed as a system of linear algebraic equations. Sources are modelled using a Gaussian and at one scattering distance inside the medium. In this work is also considered the use of spatial prior in the model to spatially guide the solution to improve the reconstruction.

- In a later work, Zhu *et. al.* 2011 [221] extended the FEM model to describe TD fluorescent light propagation with an error 0.22% compared to a MC simulation. The FEM model has a similar structure than the FD and CW models. The approach was proposed to properly track earl photon arrivals and the exploit the advantages of TD systems on three-dimensional geometries.

3.5 Image reconstruction approaches

Typically, image reconstruction techniques require a forward model used to describe the geometry and a baseline or initial guess of optical properties. By a proposed reconstruction approach, the optical properties in the forward model are updated by an optimization process using experimental measured data. The process ends once a solution is found or the optimization process is stopped by a given condition.

In Diffuse Optical Imaging, the image reconstruction process is known as solving the inverse problem, it involves the estimation of the optical parameters for a given set of light sources q and measured data Γ detected on the boundary of the medium $\partial\Omega$. Essentially, the solution to the inverse problem is described by

$$u(r) = P^{-1}(\Gamma). \tag{3.47}$$

where $u(\cdot)$ represents the optical properties of the medium and P^{-1} is the inverse operator of P which describe the light propagation. The inverse problem is known to be non-linear and ill-posed; traditional solution methods include singular value decomposition (SVD) and iterative methods [149].

In the following section are presented some of the approaches used to solve

the inverse problem, such as the perturbation method that introduces the use of the Jacobian or sensitivity matrix **J**. Later, it is introduced the iterative scheme that the present work uses for the image reconstruction process.

3.5.1 Perturbation approach to the inverse problem

This method proposed by Arridge *et. al.* [134, 209], assumes that the optical properties of the target medium are the perturbations $\Delta\mu_a$ and $\Delta\kappa$ to the absorption, μ_a and diffusion, κ, parameters of the background. An important consideration to use this approach is that the optical parameters of the perturbation must be close to the values of the background medium [180].

Considering the following diffusion equation as the background medium

$$\nabla \cdot \kappa(r)\nabla\phi(r) - \mu_a(r)\phi(r) = q(r), \tag{3.48}$$

by assuming that the optical parameters of the target medium are close to the background, light distribution of the target is equal to the light intensity of the background medium plus a perturbation:

$$\begin{aligned} &\nabla \cdot (\kappa(r) + \Delta\kappa(r))\nabla(\phi(r) + \Delta\phi(r)) \\ &-(\mu_a(r) + \Delta\mu_a(r))(\phi(r) + \Delta\phi(r)) = q(r) \end{aligned} \tag{3.49}$$

substrating Eq. (3.48 from Eq. (3.49) yields to

$$\nabla \cdot [\kappa(r)\nabla\Delta\phi(r) + \Delta\kappa(r)\nabla\phi(r) + \Delta\kappa(r)\nabla\Delta\phi(r)] = 0.$$

Barbour, *et al.* [222] proposed a linearisation, which is valid for optical parameters of a target medium that are close to a reference medium, that neglects the second-order perturbation terms in Eq. (3.50), so that

$$\begin{aligned} \nabla \cdot \kappa(r)\nabla\Delta\phi(r) - \mu_a(r)\Delta\phi(r) + [\Delta \cdot (\Delta\kappa(r)\nabla\phi(r) - \mu_a(r)\phi(r)] \\ = \nabla \cdot (\kappa(r)\nabla\Delta\phi(r)) - \mu_a(r)\Delta\phi(r) + q'(r). \end{aligned} \tag{3.50}$$

By considering $\Delta\mu_a$ and $\Delta\kappa$ to be sufficiently small, it results that light

propagation is still modelled by the diffusion equation. A formulation that describes the difference in the measurements $\Delta\Gamma$ due to a perturbation is

$$\Delta\Gamma = \mathbf{J}\Delta u \tag{3.51}$$

where Δu can be either $\Delta\mu_a$ or $\Delta\kappa$.

Equation (3.51) provides an image reconstruction formulation called *perturbation method* which relates the measurement difference $\Delta\Gamma = \Gamma_{target} - \Gamma_{background}$ between predicted and experimental measurements to the difference between target optical parameters (unknown) and known optical parameters of a reference medium.

Matrix **J** is usually constructed using numerical methods and is referred as the Jacobian or sensitivity matrix of the forward problem [12]. Other approaches for constructing **J** involve the use of an infinite space geometry in which an analytical expression can be formulated or by a Monte Carlo simulations [223]. The formulation of the Jacobian using numerical models is normally used due to the ability of being directly implemented on computational solvers.

Using a numerical image reconstruction, the aim is to find the inverse of the Jacobian matrix given in Eq. (3.51). Approaches such as the Algebraic Reconstruction Technique (ART), the Simultaneous Iterative Reconstruction Technique [114] and the Simultaneous Algebraic Reconstruction Technique [222] can be used for the inversion process.

Other approaches make use of subspace algorithms where Eq. (3.51) is treated as a least square problem expressed as

$$E = ||\Delta\Gamma - \mathbf{J}\delta u||^2, \tag{3.52}$$

where conjugate gradient methods have been used to solve the inverse problem with a superior performance in the estimation of both the spatial location and

the magnitude of the optical properties [88, 224].

Image reconstructions based on the perturbation method are less time-consuming and relatively easy to implement, but require that the target anomalies need to be close to the background, otherwise, the error is expected to be large due to the solution is made typically in one step.

3.5.2 Iterative image reconstruction

To improve the image reconstruction capabilities of perturbation methods, it is formulated necessary the use of iterative schemes that minimize the error between reconstruction steps. For these class of methods, the inverse problem is formulated as an non-linear problem where an objective function given by

$$\chi = \frac{1}{2}\sum_{j=1}^{S}\sum_{i=1}^{M}(\Gamma_i(j) - \hat{\Gamma}_i(j)) \tag{3.53}$$

where Γ are the experimental measurements and $\hat{\Gamma}$ the calculated data, $i \in 1, ..., S$ denotes the i-th measurement from source $j \in 1, ..., M$ and S and M indicate the number of sources and detectors, respectively.

Due to the ill-condition of the inverse problem and the complexity of the geometries found in biological tissue, it is normally solved using iterative non-linear optimization methods such as the Newton method [225] and the Levenberg-Marquard (LM) [33, 226].

Model Based Iterative Image Reconstruction (MOBIIR) techniques are iterative image reconstruction methods based on perturbation formulation [227, 181]. Thus assuming that the target optical properties, $u = [\mu_a, \mu_s^{'}]$, are a small perturbation to an estimated optical property distribution u_{est}.

From the distribution of optical properties, predicted measurements $\Gamma_{Pred} =$

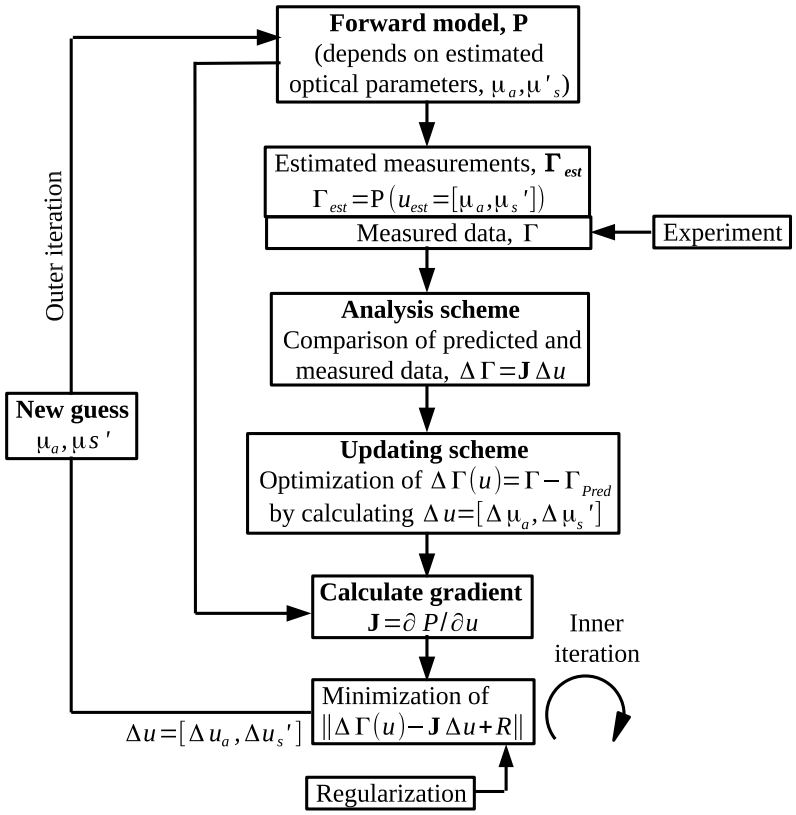

Figure 3.3: Model Based Iterative Image Reconstruction scheme (MOBIIR) based based on perturbation methods.

$P(u_{est})$ are generated and then analysed considering experimental data Γ obtained from the boundary of the target medium. It is important to consider a calibration procedure due to a variety of parameters that might affect the experimental measurements such as, source-detector separation, boundary imperfections, changes in source intensities, gain of detectors or the presence of hair [11, 228].

If the estimated optical properties u_e are close to the target distribution u, the following Taylor's expansion can be performed:

$$\Gamma = P[u_e] + P'[u_e](u - u_e) + (u - u_e)^T P''[u_e](u - u_e) + \cdots \tag{3.54}$$

where P' and P'' are the first- and second- order derivatives of the forward model for the optical parameters u. The matrix representation of P' is referred as the Jacobian or weight function $\mathbf{J}$ and P'' is known as the Hessian H of the problem.

By defining the difference between experimental and predicted measurements as $\Delta\Gamma = \Gamma - \Gamma_{Pred}$ and the difference between the target and estimated optical properties as $\Delta u = u - u_{est}$ Eq. (3.54) becomes:

$$\Delta\Gamma = \mathbf{J}[u_{est}]\Delta u + \Delta u^T H[u_{est}]\Delta u + \cdots . \tag{3.55}$$

If we neglect second-order terms in Eq. (3.55), the problem is reduced to the solution of a set of linear equations for Δu given by

$$\Delta u = \mathbf{J}^{-1}[u_{est}]\Delta\Gamma, \tag{3.56}$$

knowing Δu and the reference medium u_{est} allows the calculation of the target optical properties $u = \Delta u + u_{est}$ corresponding to the reconstructed image. Figure (3.3) depicts the image reconstruction process where the continuous update of u_{est} is represented in the outer iteration.

The Jacobian matrix is ill-conditioned and performing its inverse is computationally demanding. Therefore, the inverse of the Jacobian is usually treated as an optimization problem where the functional

$$\chi(\Delta u) = \|\mathbf{J}[u_{est}]\Delta u - \Delta\Gamma\| \tag{3.57}$$

is minimized. This minimization process is referred in Fig. (3.3)as the inner iteration. Introducing a regularization term in the inner iteration constrains the solution of Δu by making the Jacobian matrix more diagonally dominant [180].

Other approaches used by MOBIIR are Conjugate Gradient (CG)-based methods [180, 149], illustrated in Fig. (3.4). In a similar way as the perturbation based approach, (CG)-based methods make use of a forward model to generate predicted measurements Γ_{Pred} and an analysis scheme that compares this predicted data with experimental measurements Γ.

In CG-based methods, the difference between the predicted Γ_{Pred} and experimental Γ measurements is defined by an objective function χ, i.e. a least

square error norm $\chi(u) \sim (\Gamma - \Gamma_{Pred}(u))^2$. It is necessary a regularization term to reduce the ill posed form of the problem. By defining χ, no linearisation is required [180].

The minimization of the objective function is divided in two stages:

1. The gradient of χ is calculated as $d\chi(u)/du$, which is different to the Jacobian used in the perturbation method.
2. An iterative minimization is performed in the direction given by the gradient, which is labelled as the inner iteration in Fig (3.4). This step is performed several times until a minimum of $\chi(u)$ is found and a new optical distribution u is used to calculate a different gradient. The process stops once a set of optical parameters u is found that produces the smallest $\chi(u)$.

The conjugate gradient method is used because it is known to be efficient and accurate for large dimensional problems, using a low and predictable memory usage, requiring only the function and the gradient values at each iteration, and it updates the optical values before calculating the Jacobian [229].

The procedures above mentioned use FEM to estimate the detector measurements in each iteration, as a consequence, these methods are computationally expensive and time consuming. Some efforts have been made to increase the speed by reducing the mesh size, without compromising the accuracy [182, 230, 231].

Another problem regarding Jacobian-based methods is that they are highly dependant on the initial guess, as a result, the image reconstruction solution tend to converge to a local minimum instead to the true optical values. This problem has been addressed by incorporating *a priori* information, for example, it has

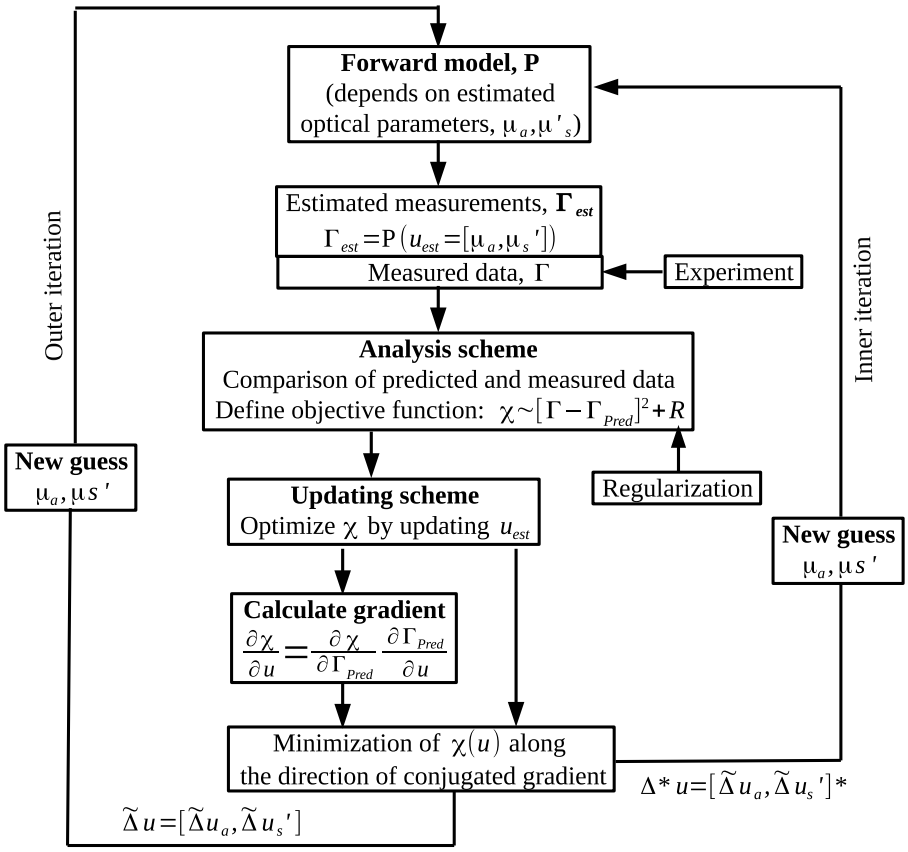

Figure 3.4: Model Based Iterative Image Reconstruction scheme (MOBIIR) based based on conjugated gradient methods.

been shown that by incorporating anatomical information derived from MRI, the quality of the image is significantly improved [232, 233].

3.5.3 Jacobian calculation

For inverse solvers based-on optimization such as Newton-Raphson or Conjugate Gradient methods, the Jacobian calculation is an important task. The Jacobian represents the sensitivity for a source-detector pair to changes of the optical parameters at each node. For this reason, it is also known as the sensitivity or weight matrix in diffuse optical tomography theory [157].

The Jacobian is calculated using numerical methods such as the Finite Element Method, where the simplest procedure in to perturb each node or element

and obtain the limit with respect of the perturbation, this involves the calculation of the DE at each node which is time consuming [182]. Another approach is to directly differentiate the FEM matrices after discretization with respect to the optical parameters [183].

A more efficient and accurate approach for the calculation of the Jacobian is by the use of the reciprocity theorem [209], which applied to light diffusion states that the output flux of a detector at position r with a light source at r' is equal to the output flux measured at r' with the same source at position r [234].

The Jacobian for absorption changes considering the reciprocity theorem is [209]

$$\mathbf{J}_{\mu_a}(d_i, s_j, r) = \left[\sum_{k|N_k\in\tau(r)} \phi_k^{(i)}(r)\psi_k(r)\right] \times \left[\sum_{k|N_k\in\tau(r)} \phi_{adj,k}^{(j)}(r)\psi_k(r)\right] \tag{3.58}$$

and for diffusion changes

$$\mathbf{J}_{\kappa}(d_i, s_j, r) = \sum_{k|\psi_k,\psi_m\in\tau(r)} \phi_k^{(i)}(r)\phi_{adj,k}^{(i)}(r)\nabla\psi_k(r)\cdot\nabla\psi_m(r) \tag{3.59}$$

where ϕ and ϕ_{adj} correspond to the solution of the direct and adjoint diffusion equations, respectively; d_i is the i-th detector, s_j the j-th source and ψ denote the basis functions or polynomial approximation used for the densities ϕ and ϕ_{adj}. In section 3.3.5 is presented the definition of variables and matrices for the discretization.

The Jacobian structure can be expressed as [157]

$$\mathbf{J} = \begin{bmatrix} \frac{\delta \ln I_1}{\delta \mathbf{u}_1} & \frac{\delta \ln I_1}{\delta \mathbf{u}_2} & \cdots & \frac{\delta \ln I_1}{\delta \mathbf{u}_{N_n}} \\ \frac{\delta \ln I_2}{\delta \mathbf{u}_1} & \frac{\delta \ln I_2}{\delta \mathbf{u}_2} & \cdots & \frac{\delta \ln I_2}{\delta \mathbf{u}_{N_n}} \\ \vdots & \vdots & \ddots & \vdots \\ \frac{\delta \ln I_{Nm}}{\delta \mathbf{u}_1} & \frac{\delta \ln I_{Nm}}{\delta \mathbf{u}_2} & \cdots & \frac{\delta \ln I_{Nm}}{\delta \mathbf{u}_{N_n}} \end{bmatrix}, \tag{3.60}$$

where $\delta \ln I_i/\delta \mathbf{u}_j$ are sub-matrices that define a change in the amplitude of the i-th measurement from changes in any of the optical properties.

For example, depending on the optical properties defined by the FEM mesh, the Jacobian could take several forms, such as the one presented by Chu and Dehghani [235] constructed by absorption coefficient, scattering coefficient and anisotropy factor that produced a Jacobian with three separate kernels:

$$\mathbf{J} = [J_{\mu_a}; J_{\mu_s'}; J_g] \tag{3.61}$$

where J_{μ_a}, $J_{\mu_s'}$ and J_g are the sensitivity functions to changes in absorption, scattering and anisotropy, respectively, with the following form

$$J_{\mu_a} = \left[\frac{\delta log I}{\delta \mu_a}; \frac{\delta \theta}{\delta \mu_a}\right] \tag{3.62}$$

$$J_{\mu_s'} = \left[\frac{\delta log I}{\delta \mu_s'}; \frac{\delta \theta}{\delta \mu_s'}\right] \tag{3.63}$$

$$J_g = \left[\frac{\delta log I}{\delta g}; \frac{\delta \theta}{\delta g}\right] \tag{3.64}$$

where $\delta\theta/\delta\mathbf{u}$ denote changes in the phase due to changes in the optical properties $\mathbf{u} = [\mu_a, \mu_s', g]$.

Due to the dynamic range of the measurements the use of the logarithm of the signals have shown to improve the quality of the reconstruction and the reduction of boundary artifacts [236]. Each row in Eq. (3.60) is known as the Photon Measurement Density Function (PMDF) and each column correspond to the perturbation in the data due to an heterogeneity at a certain node.

As an example, consider a circular geometry with radius of 43mm, 16 equally spaced sources and detectors located as seen in Fig. 3.5. The optical properties were set considering an homogeneous medium with $\mu_a = 0.01$ mm^{-1}, $\mu_s = 10$ mm^{-1}, g = 0.9 and refractive index $n_{idx} = 1.33$.

The sources were placed at 1 mm inside the medium, corresponding to one reduced scattering distance. A modulation frequency of 100 MHz was selected for this experiment and the medium was discretized into a FEM mesh consisting

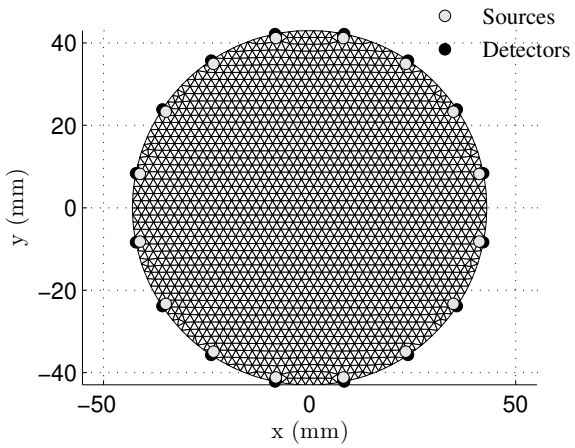

Figure 3.5: Circular geometry with 43mm of radius, 16 sources and detectors were equally located around it.

of 1785 nodes and 3418 triangular elements [235].

In Fig. 3.6a is presented the sensitivity of the amplitude from source 2 to detector 11 due to changes in the absorption coefficient. Figure 3.6b presents the sensitivity to the same source-detector pair due to diffusion changes. In both cases, it is observed that the higher values are close to the sources and detectors, decreasing towards the centre of the medium. Negative values in Fig. 3.6a indicates that by increasing the absorption results in the reduction of the measured intensity. For the scattering coefficient are also observed negative values, but with a lower magnitude compared with the effects of the absorption parameter [235].

3.6 Regularization methods and *a priori* information implementation

Assuming that anatomical and/or physiological information is available from other modalities, such as MRI or X-ray, it is possible to define a region of interest (ROI) to reduce the ill posed condition of the Jacobian matrix and to solve the

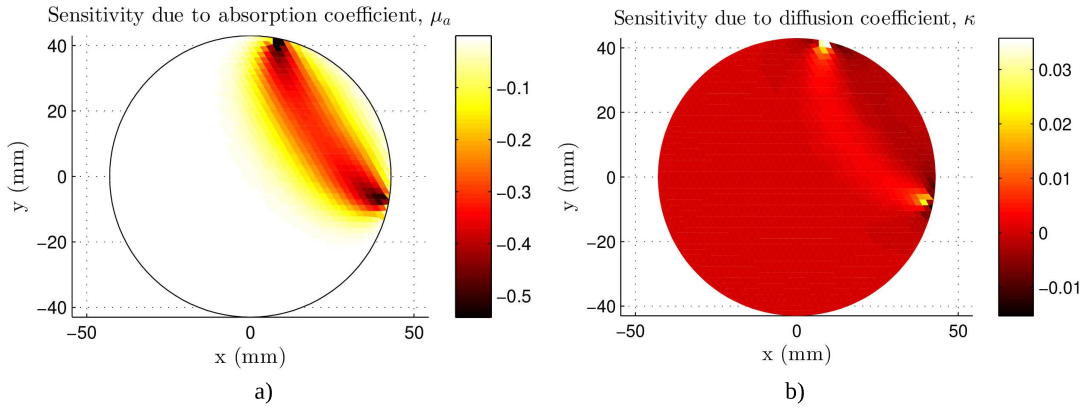

Figure 3.6: Sensitivity of a homogeneous medium due to a) absorption and b) diffusion changes.

inverse problem more efficiently. Uncertainties in the *prior* information due to low image resolution or tumour tissue can introduce errors an variations in the solution by imposing incorrect model assumptions. There are two main *prior* regularization approaches:

- *Hard prior* approach. Considering a nonlinear operator $\Gamma = P(\mu_a, \kappa)$, where Γ is a complex vector which components are mapped to log amplitude and phase measurements. Defining the image reconstruction as

$$(\hat{\mu_a}, \hat{\kappa}) = \arg\min_{\mu_a,\kappa} = \|\Gamma - P(\mu_a, \kappa)\| \tag{3.65}$$

  a Levenberg-Marquard algorithm is used to repeatedly solve

$$(\Delta\mu_a, \Delta\kappa) = J^T(JJ^T + \lambda I)^{-1}\Delta\Gamma \tag{3.66}$$

  where J is the Jacobian and $\Delta\Gamma = \Gamma - P(\mu_a, \kappa)$ is the difference between the experimental data and model measurements [237].

  This type of regularization prioritize the optical property distributions according to the regions from the segmented image given by the *a priori* information. The difficulty of this approach is the potential introduction of errors and variations due to incorrect model considerations and uncertainties in the prior information [231].

- *Soft prior* approach [231]. This regularization method uses the ℓ_2-norm to

spatially regularize the solution. It relates the optical parameter of a node with the optical parameters of the surrounding nodes by minimizing the objective function

$$\chi = \underset{x}{\text{minimize}}||y_{exp} - y_{mod}|| + \lambda||L(u - u_0)|| \tag{3.67}$$

where λ is the Tikhonov regularization parameter which balances the effect of the prior with the model-data mismatch, u_0 is the initial guess of the optical parameters and L is a Laplacian-type regularization matrix which relaxes the smoothness constraints between different tissue layers [238, 239].

In the case of FDOT, the parameters to be reconstructed are the fluorescent yield $\eta\mu_{af}$, product of the quantum efficiency η and the fluorescent absorption coefficient μ_{af}, and the lifetime τ of the fluorophore. Assuming that the chromophores in the medium are known in both wavelengths $(\mu_{a(x,m)},\ \kappa_{x,m})$, a direct method to recover the fluorescent parameters $u = (\eta\mu_{af}, \tau)$ is given by the minimization of [240]

$$\hat{u} = \arg\min_{u} ||P(u) - \Gamma||_2^2 \tag{3.68}$$

where $P(u)$ and Γ represent the model and the experimental measurements, respectively. Due to the ill condition of of Eq. (3.68), an ℓ_2 regularization with initial guess u_0 is introduced in the form

$$u^{n+1} = u^n \arg\min_{\delta u}[||J^n\delta u - (Y - J^n\delta u^n)||_2^2 + \lambda||\delta u||] \tag{3.69}$$

where J^n is the Jacobian computed after the n-th iteration for the current value $u^n = (\eta\mu_{af}, \tau)$, δu is the change of fluorescent parameters and λ is the regularization parameter.

3.7 Image reconstruction in Fluorescence Diffuse Optical Tomography

The image reconstruction in FDOT slightly differs from the standard DOT image reconstruction. Essentially the objective function for the minimization in FDOT is given by [219]

$$\chi = \sum_{i=1}^{N_{meas}} \left(\Gamma_{x,m}^{Meas} - \Gamma_{x,m}^{Calc}\right) + \lambda \sum_{n=1}^{N_{nodes}} I\left(u_0 - u\right)^2 \tag{3.70}$$

where $\Gamma_{x,m}^{Meas}$ are the experimental measurements, $\Gamma_{x,m}^{Calc}$ are the measurements calculated using a forward model such as the one given by Eq. (3.41), N_{meas} is the number of available measurements, N_{nodes} is the number of optical properties to be reconstructed, corresponding to the total of number of nodes in the inverse mesh, λ is the regularization term, I is the identity matrix, u_0 is the initial guess of optical properties and u represents the optical properties to be estimated. Subindexes x and m indicate the excitation and emission wavelength, respectively.

Assuming that the endogenous optical parameters $u_{x,m} = (\mu_{a(x,m)}, \mu_{s(x,m)}^{'})$ are known, the fluorescence yield distribution $u_{fl} = \eta\mu_{af}$ is estimated using the update function [219, 241]

$$\Delta u_{fl} = [J^T J + \lambda I] J^T (\Gamma_{fl}^{Meas} - \Gamma_{fl}^{Calc}) \tag{3.71}$$

where λ is a penalty term multiplied by the maximum value on the diagonal of the Hessian matrix $J^T J$ which is updated at each iteration. The Jacobian matrix J is calculated using the Adjoint method proposed by Arridge and Schweiger [209].

If the endogenous optical parameters are not known *a priori*, it is necessary to perform the image reconstruction of these before the estimation of μ_{af}. For the excitation case, Eq. (3.70) and Eq. (3.71) are used with the term $u_x = (\mu_a, \mu_s^{'})_x$ and a light source at the excitation wavelength.

The same procedure is used at the emission wavelength considering the term $u_m = (\mu_a, \mu_s^{'})_m$ in Eq. (3.70) and Eq. (3.71) and a light source at the emission wavelength.It is important to note that for FDOT image reconstruction techniques require the information of the endogenous optical properties of the medium at both wavelengths due to their presence in the diffusion equation.

Furthermore, in order to minimize the effects of unknown optical parameters, source light intensities variations, detector gains and coupling effects it is required a calibration procedure and some normalization such as the Born-Ratio normalization (normalized emission intensities by excitation intensities) [221, 160, 86] or the Normalized Difference method [88] which associates relative measurement changes due to changes in the optical parameters as

$$\begin{aligned} J_r \Delta u &= \Delta\Gamma \\ &= \frac{(\Gamma_1)_i - (\Gamma_2)_i}{(\Gamma_2)_i}(\Gamma_r)_i \end{aligned} \tag{3.72}$$

where the quantity $(\Gamma_r)_i$ is the predicted data measurements from a known mathematical model for test solution.

Software packages such as NIRFAST [22] and TOAST++ [23] already have implemented several of the required algorithms to perform image reconstructions from simulation models to real experimental data, and are great tools to start working straight away with DOT, FDOT and NIR spectroscopy. In the case of TOAST++, several of their functions written on C which speed-up the reconstruction, but NIRFAST offer several functions directly on Matlab, which make easier the implementation of proposed approaches.

3.8 Conclusions

This chapter has introduced the mathematical background and the computational methods used for image reconstruction and quantification of the optical properties in biological tissue. There is a wide choice of light propagation models that can be used to model light, from the accurate but computationally expensive radiative transfer equation to simpler diffusion approximation models. Similarly, to this day exist a variety of solutions to the inverse problem, some more complex that allow greater accuracy but are typically time-consuming.

The diffusion approximation (DA)to the RTE is the light transport model most commonly used in Diffuse Optical Tomography and Fluorescence Diffuse Optical Tomography due to its simplicity and that can describe tissue light interactions from relatively large tissue volumes. The typical approach used to solve the DA is by the Finite Element Method which allows modelling light propagation through complex geometries, that are commonly found in biological tissues.

The description given in the present chapter for the different methods available for estimating light propagation through tissue was to provide a general overview of their applicability and limitations. In this sense, the selection of a forward model to be used in a reconstruction scheme is the first step and needs to be clearly stated before a reconstruction technique is defined due to the information that is going to be passed to it.

The use of iterative solvers is currently the main approach used for the image reconstruction because they are suitable to be implemented in computational programs. Current advances on the hardware of computers such as high-speed processors and GPUs have increased the capabilities of DOI techniques such as

spatial resolution, accuracy of the target medium and reduced the time required for the image reconstruction.

It is known in the field of Diffuse Optical Imaging that the main limitation for it clinical applicability of imaging techniques is the time that the reconstruction take, as was mentioned, the solution is at hand due to the progresses made in processors and GPUs, but the use of high-spec computers also means that a great investment is needed. In other words, although the goal of DOI is to be used as cost effective imaging alternative to more expensive modalities, in order to bring a DOI technique into operation it is required an expensive computer to perform the reconstructions.

Then, there is clear need for computationally efficient models that can handle the complexity of the image reconstruction with a reliable accuracy and to perform it in a fraction of the time that normally is required without the necessity of an expensive computer or even the need of GPUs to be installed in a normal desktop.

Chapter 4

Reduced-order models of light transport in tissue

4.1 Introduction

Modelling complex systems using data-based models offer several advantages over traditional and formal methods that require equations of physical events that sometimes are too complex to generate reliable estimates. The process of obtaining simplified models generated by input-output data is known as system identification which is a discipline in automatic control engineering [242].

The Reduced-Order Models approach, introduced in this chapter, comes from the system identification theory and focuses on the correct structure detection and parameter estimation using a polynomial representation to obtain an accurate and simplified model of the system identified. Extending the nonlinear system identification theory to DOI, Vidal-Rosas *et. al.* 2014 [243] proposed an approach called Reduced-Order Models (ROM)to create light transport models using data and then be used in an image reconstruction technique. The imporant characteristic of ROM is that they are less computationally demanding with an accuracy that can match with other reconstruction approach.

The present chapter explains the formulation of the ROM approach to image reconstruct the absorption parameters of a highly scattering medium. To evaluate the advantages and limitations of ROM, the effect of mesh density and the number of source-detector channels on the performance of the ROM approach in the reconstruction of absorption changes. A similar study was conducted by [212] were the authors showed that by increasing the number of source-detectors channels, the sensitivity of the domain increases; and therefore, the quality of the reconstruction also improves.

This idea has been exploited by High-Density DOT [151, 36] that has showed comparable resolution to functional Magnetic-Resonance Imaging (fMRI) at the cortex level [244]. On the other hand, increasing the number of channels requires more computations, slowing down the reconstruction time.

Is important to mention that mesh density has an important effect on the accuracy of the reconstruction. Normally, a coarse mesh will produce inaccurate Jacobian matrices which will result in poor reconstructions [212]. On the other hand, high-resolution meshes can model large variations of the Jacobian close to the sources and boundaries correctly; however, the consumption of resources such as memory and computational power is also large.

The use of graphical processing units (GPUs) offers a solution to perform this kind of reconstructions. The reason is due to GPUs are well suited for processing large data sets, besides GPUs can be added to scale the processing power and further speed up the image reconstructions of endogenous optical properties [245, 246, 247]. Furthermore, the use of GPUs has been also extended to the FDOT applications to overcome the limitations related to depth tissue light re-emission analysis [248]. However, GPUs are expensive and require further technical expertise for their applicability.

Despite that strategies to optimize the inverse processes are available, such as the Jacobian reduction scheme [249] or the use of GPUs real-time reconstruction is still not achievable taking several minutes to perform the reconstruction of a single image [23, 250].

Therefore, it is desirable to evaluate the performance and limits of the ROM approach as an alternative to achieve real-time reconstructions. A previous study demonstrated the feasibility of the real-time tomographic reconstruction of haemodynamic changes in the rat brain [243]; however, the effect of the mesh resolution and source-detector channels has not been analysed. In this section, these parameters are evaluated in the reconstruction of dynamic changes of the absorption coefficient.

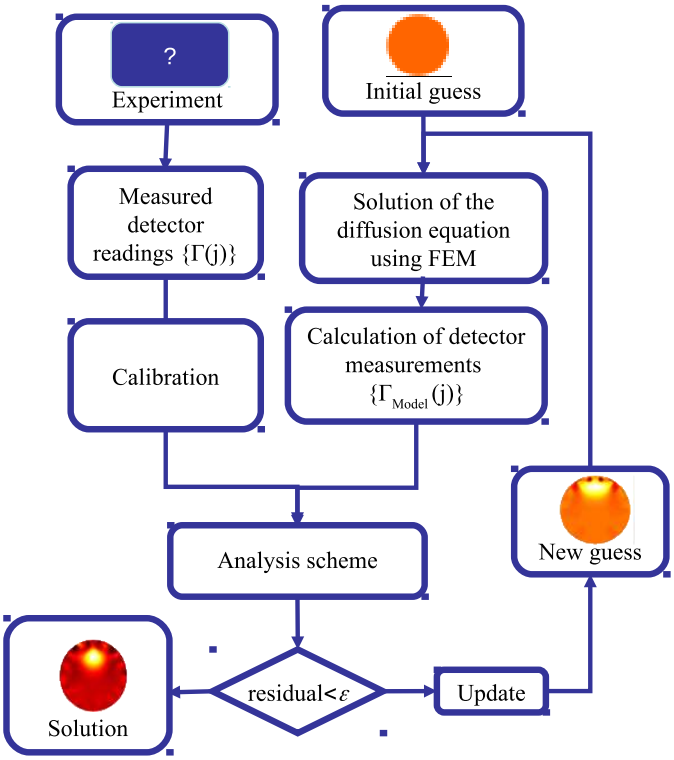

Figure 4.1: Iterative image reconstruction scheme that solves the forward problem using a mesh based on the Finite Element Method (FEM) and later the measurements are calculated.

In Fig. 4.1 is presented an example of a traditional DOT reconstruction scheme based-on FEM mesh. A FEM mesh is used to compute light propagation in the medium and then to calculate fluence measurements. However, the use of the Finite Element Method tends to increase the complexity of the inverse solver, specially for three-dimensional geometries where a large number of nodes are used to discretize the medium, thus solving the forward problem becomes a bottleneck for the image reconstruction [60].

To address the real-time limitation of diffuse optical tomography reconstructions without compromising the quality of the image, a novel forward solver denominated Reduced Order Model (ROM) approach has been proposed by Vidal-Rosas, *et. al.* [65, 243, 65]. This approach estimates models directly from data generated by a high-fidelity simulation, where the input-output relationship between measurements and optical properties of the medium for different source-detector configurations are approximated using polynomial expressions.

The ROM obtained are later used as the forward solver in an iterative image reconstruction scheme as is depicted in Fig. (4.2). The proposed approach includes a procedure for selecting, for each source-detector configuration, the minimal subset nodes that influence significantly the amount of light measured by the detectors.

The estimated models follow the *parsimonious* principle [251], which advocates the choosing of a model with the minimum number or parameters that best describes the system. Thus, resulting in a significant reduction in computation time whilst maintaining similar level of accuracy. Due to the simplicity of the models and the low computational power required to solve them, a 3-D image reconstruction can be reduced by three orders of magnitude using a low-spec computer [243].

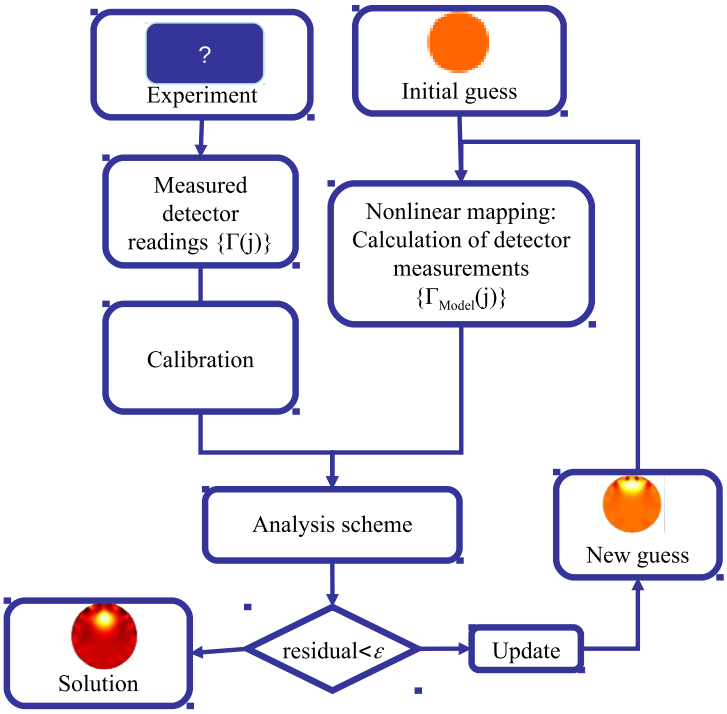

Figure 4.2: Iterative image reconstruction scheme based on Reduced Order Models (ROM). Light propagation is directly mapped from the optical properties to the measurement space.

4.2 Procedure to estimate polynomial Reduced Order Models

As it was defined in Section 3.2, lets consider a domain Ω with boundary $\partial\Omega$ with $q_i \in \partial\Omega$ and $d_j \in \partial\Omega$ that denote the locations of S sources and D detectors on the boundary of the domain of interest. By considering only one source being active in turn, this result in a total of $S \times D$ measurements.

The forward problem is then defined as: given a source q and a set of optical parameters $u(r) \in U$, and a mathematical model of light transport tissue, predict the measurements $[y_1(j), ..., y_D(j)]_{j=1,...,S} \in \partial\Omega$. The corresponding input-output relationship between parameters u and measurements y can be written as

$$y_i(j) = P_j u(r), \qquad j = 1, ..., S \tag{4.1}$$

where $P_j : U \rightarrow Y$ is the forward operator from the space of optical parameters $u(r)$ to the space of measurements $y_i(j)$ with $i = 1, ..., S$ and $j = 1, ..., D$.

The forward operator P_j is the composition of a non-linear operator, from the space of optical properties through the photon fluence and the space of measurements expressed as $P = U \rightarrow \Phi \rightarrow Y$, where Φ is the space of light propagation solutions given by Eq. (3.15) and the space Y given by Eq. (3.17) which relates the photon density ϕ to the outward flux.

The proposed reduced-order forward model involves estimating Eq. (4.1) directly from input-output data. The estimated forward model is then used in an iterative reconstruction scheme as is shown in Fig. (4.2). By mapping directly the measurements from the optical properties considering the *parsimonious* principle, offer the advantage of reducing the image reconstruction process [252].

In the present work, a polynomial representation is used for the creation of light propagation models based on the Reduced Order Models (ROM) approach. These type of models are commonly used in function approximations due to polynomial functions and their derivatives are smooth, besides they are computationally easy to use, manipulate and store.

The reduced order model of Eq. (4.1) in its component form is given by

$$\hat{y}_i(j) = f_{i,j}(u_1, ..., u_K) + e_{i,j} \tag{4.2}$$

where $\hat{y}_i(j)$ is the predicted measurement from the i-th detector and source j, $f_{i,j}$ is a polynomial approximation for the source-detector pair with $i = 1, ..., D$ and $j = 1, ...S$. The term $u_k = u_k(r)$ is the optical parameter value for the k-th node at position r and $e_{i,j}$ is the approximation error.

A key step in the estimation of a polynomial model is the selection of a minimal

set of polynomial terms. Therefore, expanding Eq. (4.2) in a multivariable polynomial form yields

$$\hat{y}_i(j) = \sum_{k=0}^{M} \theta_k(i,j) p_k(u) + e_{i,j} \tag{4.3}$$

where $\theta_k(i,j)$ are the coefficients with $i = 1, ..., N_D$ detectors and $j = 1, ..., N_S$ sources, p_k are multivariable monomial with degree of freedom equal or less than the l input function $\boldsymbol{u} = [u_1, ..., u_K]$ where K is the number of nodes in the FEM mesh and $e_{i,j}$ is the approximation error.

The M terms of the polynomial representation in Eq. (4.3) grows exponentially with the number of inputs u and the polynomial order. In practice, not all the terms are required to obtain an appropriate representation of the optical parameters and the detector measurements.

The Photon Measurement Density Function (PMDF) [209] is used to guide the Orthogonal Forward Regression (OFR) algorithm in order to further reduce the number of terms for each source-detector model. The PMDF characterize the sensitivity of the measurements to variations of the optical properties inside the medium.

Specifically, only those nodes that contribute above a given threshold (0.5 to 5%) to the PMDF are considered as the inputs for the candidate polynomial terms in the OFR algorithm. It has been demonstrated [253, 243] that the terms selected using this method correspond to the nodes within the region with the highest sensitivity.

The selection of the minimal polynomial set of terms from a full set of candidate terms in Eq. (4.3) corresponds to the structure detection. This process determines the terms that should be included in the model and is performed by the Orthogonal Forward Regression (OFR) algorithm [254]. Once a correct

model with linear parameters is determined, the parameters are estimated using a least square technique. The problem of structure identification and parameter estimation considering polynomial terms, such as the representation of Eq. (4.3), has been studied extensively and efficient algorithms can be found in the works of Billings *et. al.* [254] and Chen *et. al.* [255].

In order to apply the OFR algorithm, it is required a set of input-output data samples. The input set consists of $N \times K$ uniformly distributed random values, where N correspond to the number of samples and K the nodes of the FEM mesh. The output data corresponds to the computed measurements obtained from the input random data set. The total number of samples is divided in two sets $N = N_{estimation} + N_{validation}$, where the set $N_{estimation}$ is used for model structure detection and parameter estimation, and the remaining set $N_{validation}$ is used to validate the model

The root-mean-square error (RMSE) is used to compare the output of the estimated model and the data specified for validation, $N_{validation}$. Considering the intensities between the estimated model ,Γ_{Model}, and the measurements defined for validation, $\Gamma_{validation}$, the RMSE is given by

$$RMSE(i,j) = \sqrt{\frac{\sum_{t=1}^{K}(\Gamma_{validation}(j,t) - \Gamma_{Model}(j,t))^2}{K}} \tag{4.4}$$

where y_{val} are the measurements not used during the estimation process and $\hat{y}$ are the measurements from the polynomial ROM. The present work focuses in the development of absorption models. Functional activation and physiological changes occur in the haemodynamics, a change in the absorption is obtained, while scattering events are assumed to be constant [256].

So far, ROM has been used to reconstruct the spatial distribution of the absorption coefficient for real-time brain haemodynamic variations [243]. In this

work, ROM is extended to the reconstruction of the fluorophore distribution of diseased tissue considering variations of the fluorophore concentration. Furthermore, ROM forward model is used to characterize deep tissue using the novel Spatial Frequency Modulated Imaging technique proposed by Cuccia *et. al.* [49]. Both implementations consider three-dimensional geometries, which as stated before, increase the complexity of real-time implementation of optical imaging applications.

4.2.1 Estimation of Reduced Order Models numerical simulation

To perform the estimation of the Reduced-Order models, it is necessary to follow the following steps proposed by Vidal-Rosas [243, 65, 64]:

1. Generate a reconstruction mesh with an adequate balance between the number of nodes and measurement accuracy with a minimum of approximately 2,000 nodes [212].

2. Generate 1,000 random absorption values at each node location with a uniform distribution. The random values are the input data set.

3. Solve the diffusion equation considering the inverse mesh and the random values. Records the corresponding measurements as the output data set.

4. Compute the Photon Measurement Density Function (PMDF) for each source-detector pair as depicted in Section 3.5.3.

5. Select a minimal sub-set of candidate terms formulated in step 2 neglecting the terms that contributions is less than 1% to 5% for each PMDF calculated [249].

6. Apply the OFR algorithm to select nodes from Step 5 as follow:

(a) Form all the potential terms $p_i(t),\ i = 1, ..., M$. The polynomial terms are multivariate monomials of degree less than or equal to two.

(b) **For** i=1 to M

$$w_1^{(i)} = p_i(t) \tag{4.5}$$

$$g_1^{(i)} = \frac{\sum_{t=1}^{N} w_i^{(i)} z(t)}{\sum_{t=1}^{N} (w_1^{(i)}(t)^2)} \tag{4.6}$$

$$[ERR]_1^{(i)} = 100 \times \frac{(g_1^{(i)})^2 \sum_{t=1}^{N} (w_1^{(i)}(t))^2}{\sum_{t=1}^{N} z^2(t)} \tag{4.7}$$

end

(c) Find the maximum $[ERR]_1^{(i)}$, then set $w_1(t) = w_1^{(j)}(t)$, select $P_j(t)$ with $g1 = g_1^{(j)}$, $[ERR]_i = [ERR]_1^{(j)}$ and delete $P_j(t)$ from the candidate terms.

(d) For the n-th term, $n = 2, ..., M$ **for** $i = 1 to M - n + 1$

$$\alpha_{m,n}^{(i)} = \frac{\sum_{t=1}^{N} w_m(t) p_n(t)}{\sum_{t=1}^{N} w_m^2(t)}, \quad m = 1, ..., n-1,\ \alpha_{n,n} = 1 \tag{4.8}$$

$$w_n^{(i)} = p_n(t) - \sum_{m=1}^{n-1} \alpha_{m,n}^{(i)} w_m(t) \tag{4.9}$$

$$g_n^{(i)} = \frac{\sum_{t=1}^{N} w_n^{(i)}(t) z(t)}{\sum_{t=1}^{N} (w_m(t)})^2 \tag{4.10}$$

$$[ERR]_n^{(i)} = 100 \times \frac{(g_n^{(i)})^2 \sum_{t=1}^{N} (w_n^{(i)}(t))^2}{\sum_{t=1}^{N} z^2(t)} \tag{4.11}$$

end

(e) Find the maximum $[ERR]_n^{(i)}$, then set $w_n(t) = w_n^{(k)}(t) = p_k(t) - \sum_{m=1}^{n-1} \alpha_{m,n}^{(i)} w_m(t)$ with $\alpha_{m,n} = \alpha_{m,n}^{(k)}, m = 1, ..., n-1,\ g_n = g_n^{(k)},\ [ERRR]_n = [ERR]_n^{(k)}$ and delete $p_k(t)$ from the set of candidate terms.

(f) Repeat steps (d) and (e) and stop at the M_s-th step when

$$[ERR]_{Ms} < C_d, \quad M_s < M, \tag{4.12}$$

or when all the available terms are chosen. The range of the cut-off term is $0.05 < C_d 0.3$, where smaller values increase the quality of the models [65].

(g) Compute the linear coefficients θ_i as follows

$$\theta = gM_s$$
$$\theta_i = g_i - \sum_{k=i+1}^{M} \alpha_{i,k}\theta_k, \quad i = M_s - 1, ..., 1 \tag{4.13}$$

The ERR indicates the contribution that each term offers to the reduction of the mean square error. Also, it allows to know the significance of the term before constructing the whole model.

It is required a minimum of 200 sample points to generate the reduced-order models, less than that, the estimated models can not perform the image reconstruction. Also, it takes around 2 hours for a 2-D domain to obtain the models, and about 16 hours for a 3-D domain. It could be a limitation, but once the ROM are obtained, they can be used to image reconstruct the target medium.

4.2.2 Formulation of Reduced-Order Models using a numerical simulation example

This section illustrates the methodology for deriving a reducer-order model through a simulation example. The performance of the approach is compared with a state-of the-art conventional approach based of a full diffusion approximation model.

The aim is to reconstruct absorption changes over a circular medium. The mesh used for the image reconstruction and to generate the forward ROM has a radius $r = 43$mm and is discretized into 341 nodes and 618 elements, shown in Fig (4.3)a.

Around the medium 16 sources and 16 detectors were placed equidistantly providing 240 measurements. The absorption and scattering coefficients were $\mu_a = 0.01\text{mm}^{-1}$ and $\mu_s' = 1\text{mm}^{-1}$.

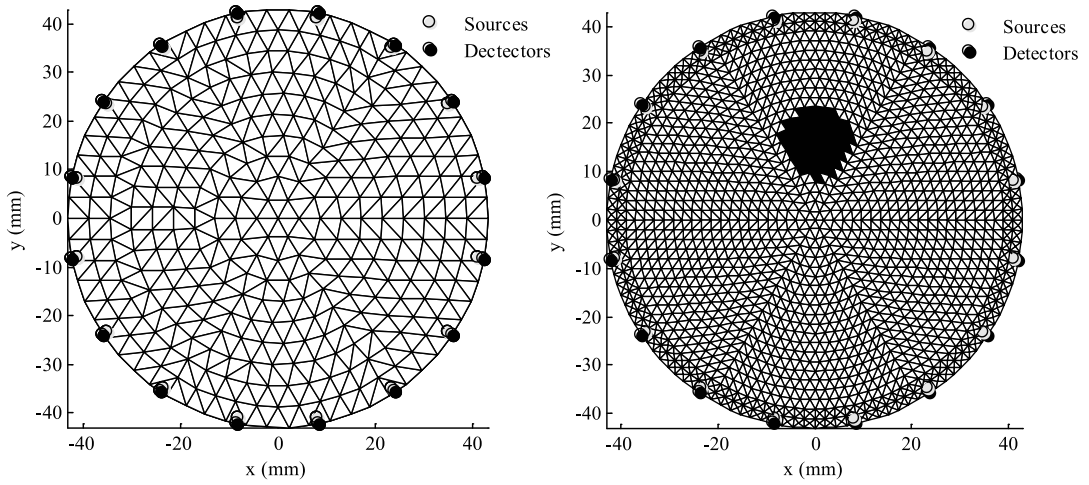

Figure 4.3: a) Coarse mesh for the inverse problem and b) structured symmetric mesh used to generate measurements with an anomaly centred at position (x, y)=(0,15).

For this inverse mesh, 1000 uniform distributed random absorption values for each node were generated. The mean value of the distribution was set to the absorption background (0.01mm^{-1}).

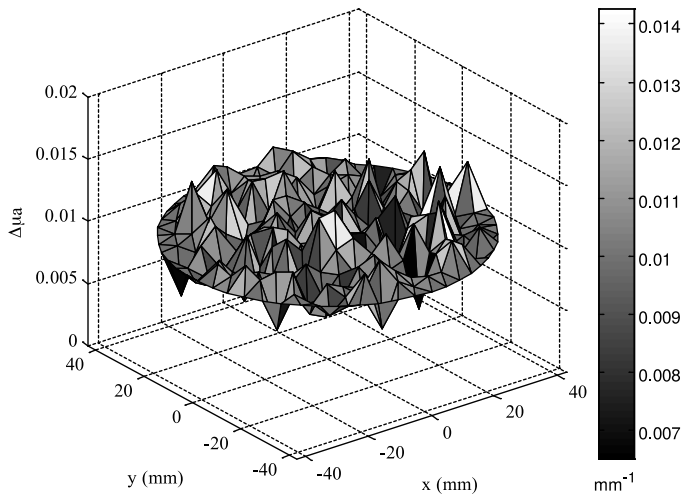

Figure 4.4: Sample of uniform distributed random absorption coefficients.

The absorption variation was selected based on the maximum absorption change expected around the background. Then , to obtain a $\Delta\mu_a < 50\%$ the variation of the absorption was set to 0.015. One sample of the random data is

presented in Fig. 4.4 where can be observed the absorption values in the nodes of the mesh.

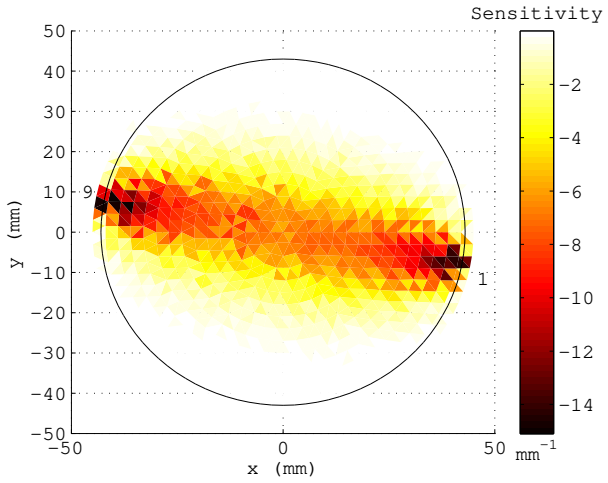

Figure 4.5: Photon measurement density function from source 1 to detector 9 used to guide the estimation process to generate the Reduced-Order Models approach.

The number of first and second order polynomial candidate terms for the inverse mesh with 341 nodes is 55,925, however this large search space is reduced by selecting the nodes with the highest contribution to the PMDF. For example, the PMDF for source 1 and detector 9 is shown in Fig. 4.5. For a 5% threshold, the number of nodes is 119 and the number of second order potential polynomial terms results in 13,923 where the best candidates are selected for the generation of the estimated models.

Next, the Orthogonal Forward Regression (OFR) algorithm was used to select the terms that contribute the most to the explained variance. The final model for source 1 and detector 9 has only 51 terms with the coefficients shown in Table 4.1 where u_i refers to the absorption coefficient $\mu_a(r_k)$ of node k at position r and θ_l are the coefficients calculated using the OFR algorithm. The model presented in Table 4.1 is the smallest one obtained after the estimation, other models are in the order of the hundreds.

Table 4.1: Parameters of the proposed forward model.

θ_i	Term	θ_i	Term
3.49e^{-4}		-3.59e^{-3}	$u_{212}u_{234}$
-2.16e^{-2}	$u_{13}u_{34}$	-3.91e^{-3}	$u_{216}u_{237}$
-8.58e^{-3}	$u_{13}u_{33}$	-2.65e^{-3}	$u_{291}u_{305}$
-8.10e^{-3}	$u_{33}u_{54}$	-2.45e^{-3}	$u_{235}u_{255}$
-1.12e^{-2}	$u_{34}u_{55}$	-2.94e^{-3}	$u_{234}u_{246}$
-7.25e^{-3}	$u_{34}u_{56}$	-2.37e^{-3}	$u_{217}u_{232}$
-7.82e^{-3}	$u_{54}u_{64}$	-2.20e^{-3}	$u_{211}u_{212}$
-7.86e^{-3}	$u_{55}u_{77}$	-2.46e^{-3}	$u_{233}u_{254}$
-7.45e^{-3}	$u_{54}u_{76}$	-1.91e^{-3}	$u_{238}u_{257}$
-7.91e^{-3}	$u_{55}u_{76}$	-2.00e^{-3}	$u_{253}u_{272}$
-8.57e^{-3}	$u_{76}u_{98}$	-2.45e^{-3}	$u_{256}u_{275}$
-8.54e^{-3}	$u_{64}u_{85}$	-2.36e^{-3}	$u_{273}u_{274}$
-8.45e^{-3}	$u_{77}u_{99}$	-1.91e^{-3}	$u_{290}u_{303}$
-8.18e^{-3}	$u_{13}u_{115}$	-1.46e^{-3}	$u_{282}u_{297}$
-8.19e^{-3}	$u_{122}u_{146}$	-1.26e^{-3}	$u_{265}u_{283}$
-6.87e^{-3}	$u_{106}u_{129}$	-1.00e^{-3}	$u_{298}u_{311}$
-6.16e^{-3}	$u_{147}u_{171}$	-1.19e^{-3}	$u_{315}u_{326}$
-4.69e^{-3}	$u_{170}u_{175}$	-9.89e^{-4}	$u_{321}u_{325}$
-4.37e^{-3}	$u_{192}u_{214}$	-9.49e^{-4}	$u_{310}u_{321}$
-4.46e^{-3}	$u_{175}u_{196}$	-9.27e^{-4}	$u_{322}u_{330}$
-4.25e^{-3}	$u_{193}u_{215}$	-9.57e^{-4}	$u_{321}u_{323}$
-4.48e^{-3}	$u_{140}u_{166}$	-9.16e^{-4}	$u_{322}u_{331}$
-4.50e^{-3}	$u_{165}u_{188}$	-9.45e^{-4}	$u_{331}u_{332}$
-4.21e^{-3}	$u_{189}u_{212}$	-8.49e^{-4}	$u_{336}u_{337}$

Table 4.1: (continuation)

θ_i	Term	θ_i	Term
-3.94e^{-3}	$u_{211}u_{233}$	-8.47e^{-4}	$u_{323}u_{332}$
-3.78e^{-3}	$u_{215}u_{236}$		

To validate the reconstruction capabilities of the proposed approach, a target medium with an anomaly is used, it has a radius $r = 43mm$ as shown in Fig. 4.3b with absorption coefficient $\mu_a = 0.01\text{mm}^{-1}$ and reduced scattering $\mu_s^{'} = 1\text{mm}^{-1}$. The medium is discretized into 1,741 nodes and 3,360 elements. A refined region near the boundary was created to increase the accuracy of the measurements. There are 16 sources and 16 detectors equally spaced around the boundary. The anomaly is an absorber was incorporated at position $(x, y) = (0, 15)$ with radius $r = 7.5\text{mm}$ and $\Delta\mu_a = 0.015\text{mm}^{-1}$.

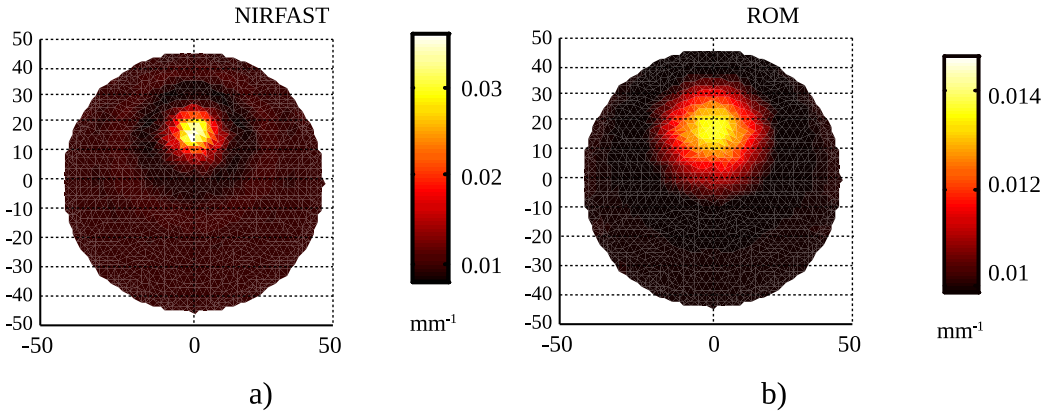

Figure 4.6: Reconstruction of the absorber inside the medium using a) NIRFAST and b) ROM approach.

Performance comparison between ROM and NIRFAST

To compare the quality of the reconstruction with ROM approach, the recovered absorption changes using NIRFAST and ROM approaches are shown in Fig. 4.6a and Fig. 4.6b, respectively.

Both approaches reconstruct the location of the absorber however, as it is displayed in Fig. 4.7, NIRFAST shows oscillations around the anomaly and overestimates its absorption value with a percentage error of $E_{NIRFAST} = 134\%$.

In contrast, ROM does not present oscillations but underestimates the absorber value with a percentage error or $E_{ROM} = 9.33\%$. It is important to note that the time required for the reconstruction is decreased considerably, for NIRFAST were necessary 27.3 seconds to reconstruct the inhomogeneity and for ROM were only required 15.7 seconds.

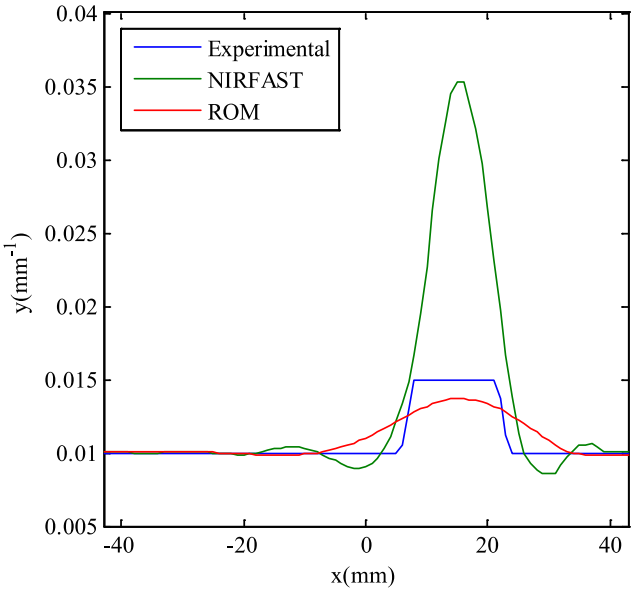

Figure 4.7: Vertical profile of the image reconstruction using NIRFAST and ROM approaches.

In the case of a three-dimensional real-time rat head simulation, Vidal-Rosas [65] demonstrated that a polynomial ROM reconstructed an anomaly in the brain in 0.47 seconds while a full diffusion approximation solver took over 1hr considering. In [243] was reported the same numerical simulation but considering radial basis functions instead of a polynomial terms. The image reconstruction in this case was 2s for the ROM-based reconstruction scheme.

In order to quantitatively assess both algorithms, the reconstructed image was evaluated by the Image Correlation Coefficient (ICC) defined by [65]

$$ICC(A,B) = \frac{1}{(N-1)} \frac{\sum_i (x_A^i - \bar{x}_A^i)(x_B^i - \bar{x}_B^i)}{\sqrt{\sum_i (x_A^i - \bar{x}_A^i)} \sqrt{\sum_i (x_B^i - \bar{x}_B^i)}} \tag{4.14}$$

where x_A^i, x_B^i denote the intensities of the i-th pixel in images A and B, $\bar{x}_A^i$, $\bar{x}_B^i$ are the mean intensities of the images evaluated. The original image is defined by A and the reconstructed image as B. The highest value is ICC=1 which indicates a perfect spatial match between both images. The corresponding image correlation coefficient obtained was $ICC_{NIRFAS} = 0.88$ and $ICC_{ROM} = 0.67$ for NIRFAST and ROM-based reconstruction approaches, respectively.

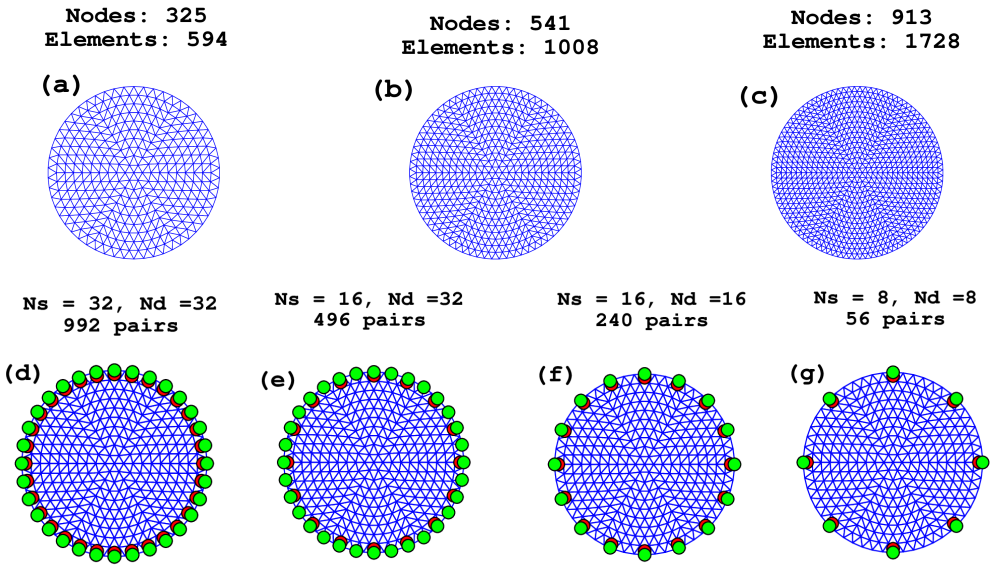

Figure 4.8: Meshes with different resolution used in the simulation: (a) 325 nodes, (b) 541 nodes, and (c) 913 nodes. Several source-detector combinations were also simulated: (d) 992 pairs, (e) 496 pairs, (f) 240 pairs, and (g) 56 pairs.

4.3 Effects of mesh density and model precision in the performance of Reduced-Order Models

The medium consisted of a circle with radius d = 25 mm and optical properties of $\mu_a = 0.01$ mm^{-1} and $\mu_s' = 1$ mm^{-1}. Three different meshes with 325, 541 and 913 nodes were simulated; these are displayed in Fig. 4.8a-c. Similarly,

several source-detector combinations were tested for each mesh resolution, which provided 992, 496, 240 and 56 source-detector channels (Fig. 4.8d-g). Simulated measurements were obtained from a high-density mesh with 2209 nodes and 4278 elements. A circular perturbation with a radius of r = 4 mm was placed at (x, y) = (10, 0), while the absorption coefficient varied according to a quasi-periodic signal defined by the following equation:

$$s_{quasi}(t) = \frac{1}{2}\left(\cos\left(\frac{\pi}{8}t\right) + \sin\left(\frac{\sqrt{\pi}}{4}t\right)\right). \tag{4.15}$$

Two hundred time points were generated and for each one, 1% Gaussian noise was added to the simulated data in order to avoid inverse crime.

For each mesh density and for each source-detector combination, second-order polynomial reduced-order models with precisions ranging from 85% to 96% were calculated. The percentage indicates the variance in the estimation data that can be explained by the model. Model calculation required input and output data. The former consisted of 1000 samples of uniformly distributed absorption values at each node location; while the latter consisted of the outward flux due to those absorption changes. The first 500 samples were used for model estimation and the rest of the samples were used for model validation.

The absorption changes were reconstructed for each time point using the standard FEM and ROM-based approaches. The inverse problem for the FEM case was solved using NIRFAST which employs an iterative Levenberg–Marquardt procedure [22]. In the same manner the inverse problem using the ROM-approach was solved using NIRFAST reconstruction algorithms, but the Jacobian and the forward solutions of the diffusion equation were substituted for polynomial models. Additionally, in order to assists in stabilizing the inversion process and to produce robust solutions to noise, a mean filter was applied after each iteration

of the inverse solver.

To evaluate the reconstructions from the different models, the following qualitative and quantitative measures were evaluated:

- Image Correlation Coefficient (ICC) stated previously, where Eq. (4.14) is applied to each time point of the quasi-periodic signal (Eq. (4.15)) and also to the time series as a whole, in this case the image A is a 2D matrix with size $N \times T$ where N is the total number of nodes and T is the total number of time points containing the original changes of the absorption coefficient. Similarly, he image B corresponds to the recovered absorption changes obtained from either FEM or ROM-based approaches.

- Absolute error given by

$$error(A, B) = \sqrt{\sum_i (x_A^i - x_B^i)^2} \tag{4.16}$$

  where x_A^i and x_B^i denote the intensities of the i-th pixel in the images A an B, respectively. The absolute error was calculated for each time point and also for the time series as a whole.

- Full-width-half-maximum (FWHM) along the x-axis and the y-axis

- Area under the curve (AUC)

- Reconstruction time

- Ratio of the reconstruction time. This ratio evaluates the speed improvement by using the ROM-based approach and it is defined as

$$R = \frac{\text{Reconstruction time NIRFAST}}{\text{Reconstruction time ROM approach}} \tag{4.17}$$

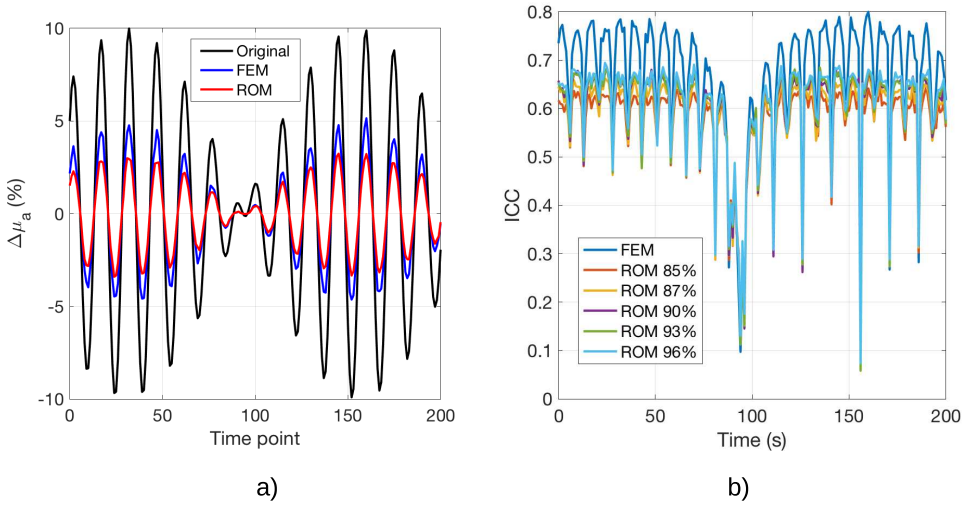

Figure 4.9: (a) Reconstruction of quasi-periodic signal, (b) ICC for each time point.

Results and discussion

The original and recovered absorption change at the centre of the inclusion $(x, y) = (10, 0)$ mm is plotted in Fig. 4.9a, these results correspond for the mesh with 325 nodes (594 elements) and 992 source-detector pairs. Both NIRFAST and ROM-based approaches underestimated $\Delta\mu_a$; however, the recovered contrast depends linearly on the original change; indicating that a calibration step can minimised the difference [257].

The ICC also varies proportionally to the original contrast, achieving higher quality reconstructions for large changes; on the other hand, the quality is compromised for $\Delta\mu_a < 1\%$. The reason is because the measured intensity due small absorption changes is buried in noise and impossible to be recovered.

A typical reconstruction of the absorption change using NIRFAST and ROM-based approaches is displayed in Fig. 4.10a and b, respectively. The original location of the perturbation is represented with the black dotted circle. A cross-section of the recovered contrast is shown in Fig 4.10c, where the underestimation of the absorption change is clearly visible.

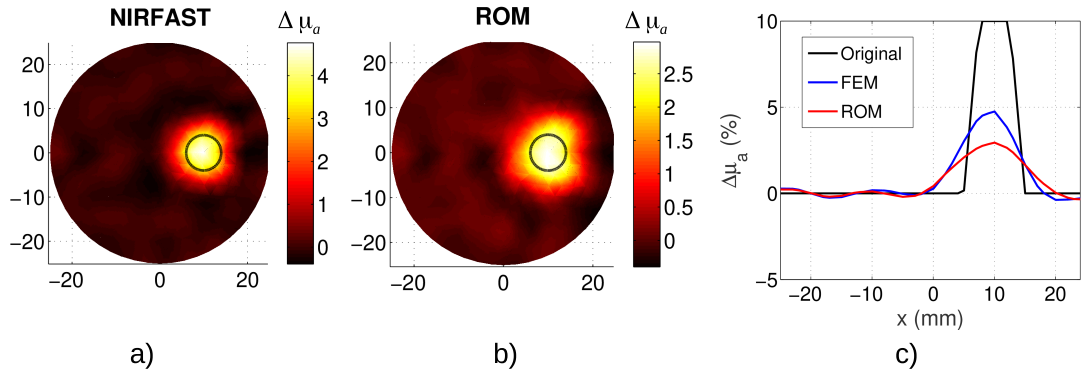

Figure 4.10: Example of the reconstruction of an absorption using (a) NIRFAST and (b) ROM approaches. (c) Vertical profile comparison from both reconstructions.

Figure 4.11 shows the ICC for all the mesh resolutions and source-detector combinations. The coarse mesh consisting of 325 nodes and 594 elements achieved the highest quality in the reconstruction. The quality of the reconstruction decreased with the number of measurements, this is explained by the reduction of the sensitivity to changes in the medium due to a decreased of the density in the volumes sampled by the Jacobian functions [212].

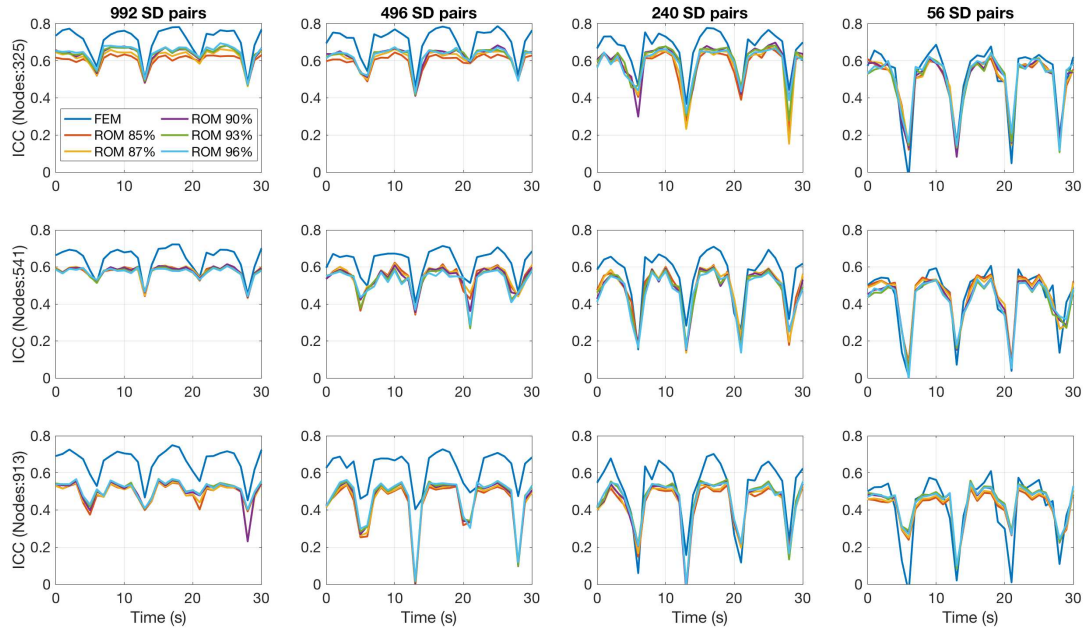

Figure 4.11: Comparison of the effect of the number of source-detector pairs and mesh density on the ICC.

In a similar way, the quality of the reconstruction decreased as the number of nodes (elements) increased. A column-wise comparison of Fig. 4.11 indicates that the effect is larger for the ROM approach than for the FEM-based approach. The reason is that an increase in the number of nodes implies an increase in the number of dimensions (each node location represents one dimension) and since all the reduced-order models were estimated using the same data size, it is possible that higher-dimensional spaces (larger meshes) were under-sampled.

Figure 4.11 also shows that the difference in the performance between the two methods decreases as the number of source-detector decreases. In the extreme case, the fourth column in Fig. 4.11 shows the ICC between the two approaches is undistinguishable. The results shown in Fig 4.12 for the reduced-order model correspond to a second-order polynomial model with a precision of 96%; however, the performance of the other models (85% to 95%) is very similar and is not shown here for the sake of space.

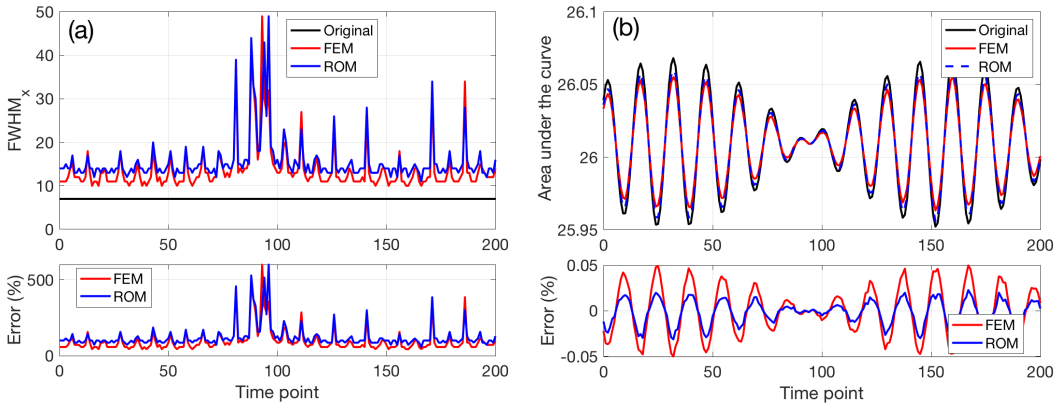

Figure 4.12: (a) FWHM in the direction of the x-axis, the values of FWHM in the direction of the y-axis are very similar (Not shown). (b) Area under the curve (AUC).

The effect of the mesh resolution and source-detector pairs on the ICC for the whole time series is shown in Fig. 4.13a. Increasing the number of measurements has a larger effect on the FEM approach; however, there is very little improvement

after 496 source-detector pairs. For the ROM-approach, similar conclusions can be reached but the effect is smaller.

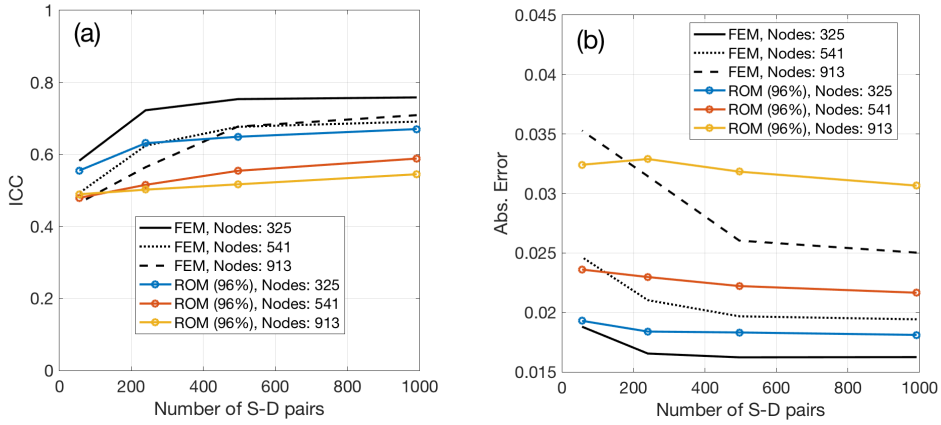

Figure 4.13: (a) Overall ICC considering the time series as a whole. Similarly, the absolute error is displayed in panel (b)

On the other hand, Fig. 4.13b indicates that the quantitative accuracy depends strongly on the mesh resolution; with the best results obtained by the coarse mesh (325 nodes, 594 elements). The effect of increasing the number of measurements is less significant in the ROM-approach than the FEM-based approach. One reason could be that since the perturbation is relatively large and close to the boundary, only a few source-detector pairs (56 S-D pairs) are enough to sample the target imaging space; possibly, the reconstruction of smaller perturbations and more complex shapes can demonstrate the benefits of high-density sampling; however, this topic is outside the scope of this study.

Finally, Fig. 4.14a shows the time required to recover the absorption changes that varied according to a quasi-periodic signal. The inverse problem was solved on a mesh with 325 nodes (594 elements) and 992 source-detector pairs. Fig. 4.14b shows that the proposed approach accelerates the reconstruction by a factor of 1.7; and on average the reconstruction speed is of 2 Hz, which can be considered as real-time.

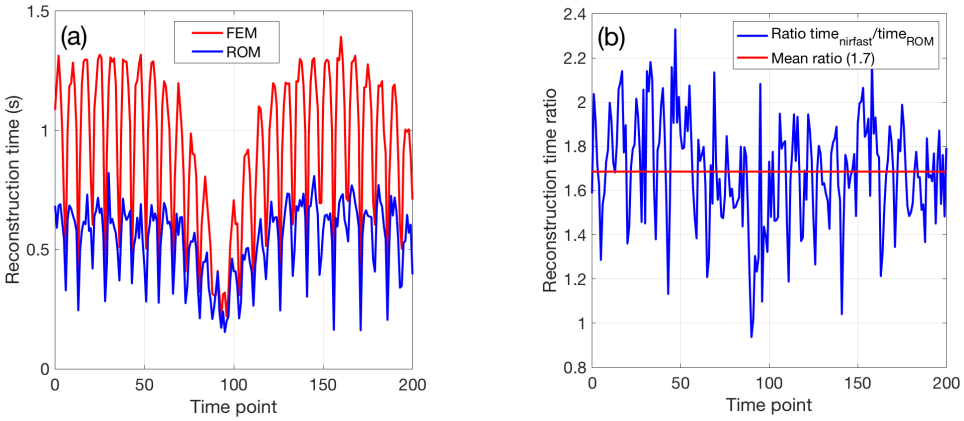

Figure 4.14: (a) Time required to calculate the absorption changes due to a quasi-periodic signal for each time point. (b) Improvement in the speed of the reconstruction for each time point.

4.4 Conclusions

This chapter introduced an approach to derive reduced-order models directly from data obtained by simulating a high-fidelity finite-element approximation of the diffusion equation. The reduced-order model provides a direct relation between the photon fluence and the measured light in the image reconstruction process.

A major advantage of the approach is that the evaluation of the reduced order model does not require to recalculate the solution of the diffusion equation over the finite-element mesh, which results in a significant reduction of the computation time, especially for complex 3D geometries.

The simulation results presented from a two dimensional geometry confirm the advantages of ROM approach as an alternative to the direct use of the D.E. in an iterative image reconstruction scheme. The major contribution of this approach is the reduction in the computational burden and the resulting reconstruction time.

In this section is also compared the effect of the mesh resolution and

the number of measurements on the performance of the ROM-based and the FEM-based approaches in the reconstruction of absorption changes. Results demonstrated that the quantitative and qualitative accuracy is not compromised by approximate models, and furthermore, despite that the meshes used have very small number of nodes and elements, still the ROM-based method outperformed the traditional FEM approach.

Although the time required for the model estimation is a limitation, once the ROM models are obtained previous research demonstrated that the reconstruction speed in three-dimensins is dramatically accelerated with the use of reduced-order models, and this method outperformed the standard FEM approach by three orders of magnitude [243].

The previous work that inspired this research was focused mainly on the application of the ROM approach reconstruct endogenous absorption parameters using a continuous-wave. It considered two types of data-based system identification: polynomial models and Radial-basis functions. It was demonstrated that the latter method didn't offer any advantages over polynomial models and added an extra effort due to the process required to determine the centres of the functions used. Thus, it was found that the use of polynomial models was accurate enough to reconstruct the targeted absorption parameters.

Among the open research left to do on the previous work was the implications for using a different source of illumination, increase the number of source-detector pairs and generate models to target a different optical property to be reconstructed. The present work for the first time cover the mentioned work to further extend the applicability of data-based modelling to complex systems such as the light propagation in tissue and the optical image reconstruction process.

.

Chapter 5

Fluorescence Diffuse Optical Tomography with Reduced Order Models

5.1 Introduction

Fluorescence Diffuse Optical Tomography (FDOT) is a relatively new imaging modality used to study molecular processes from cell culture, tissue samples and *in vivo* subjects such as small animals or to quantify the concentration of a fluorophore inside tumoral tissue.

The advantages of FDOT imaging modality are its high specificity, low cost instrumentation, less invasiveness and non-ionizing procedure, compared with other modalities such as Positron Emission Tomography and X-ray Computed Tomography. However, the main limitations of FDOT are the low spatial resolution achieved on large geometries and the time required to solve the image reconstruction process normally attained to all Diffuse Optical Imaging (DOI) techniques.

In this chapter is presented a methodology to speed up the image reconstruction of FDOT to target the fluorescent properties of exogenous fluorescent

markers using a light transport model based on the reduced-order models (ROM) approach which was used to recover the absorption properties of brain tissue in the work presented by Vidal-Rosas *et. al* 2014 [243].

The method proposed in this work directly maps the emitted fluorescent light from fluorophores within the tissue to the measured light by detectors on the boundary to recover the fluorescent optical properties. The reconstructed parameters result immune to the surrounding absorption properties of the tissue due to the emission is detected on a different wavelength, thus ROM only assess the optical properties that generated a given re-emitted fluoerescent signal.

This is a novel way to model the emission of fluorescent light and to image reconstruct and quantify the characteristics of a fluorescent marker. Typical reconstruction approaches require prior information of the distribution of the endogenous optical properties to further resolve the fluorescent emitted light. As is going to be presented in this chapter, the only information that is required is an initial guess of the background fluorescent and the maximum expected value that can be reached by the fluorescent marker.

Along this chapter is explained the formulation ROM approach to target the fluorescent marker optical properties. Besides are explored the limitations related to the number of samples, noise level and accuracy of the models formulated. To facilitate the explanation, ROM is first formulated in a two-dimensional slice from a mouse thorax model. Later, the ROM approach is extended to a full three-dimensional thorax of a mouse. In both cases, the target to reconstruct is tumoral tissue inside the lungs of the mice models.

Is important to note that this is the first time that input-output data is used to model fluorescent optical properties from the re-emitted light at the emission

wavelength. In contrast to the ROM from Vidal-Rosas *et. al* 2014 [243] which reconstructed the endogenous optical properties from a single wavelength. The work here presented considered that the excitation light and the endogenous optical properties are at a different wavelength that the fluorescent optical properties being reconstructed.

5.2 Image reconstruction with fluorescent Reduced-Order Models

In this section is shown the procedure to generate fluorescence forward reduced order models for the image reconstruction of anomalies tagged with a fluorescent marker. The ROM proposed approach is implemented in the fluorescent toolbox on NIRFAST package. The light propagation model in NIRFAST is modified and only is used its fluorescent inverse solver.

Light propagation and image reconstruction in FDOT are detailed in Section 3.4 and Section 3.7, respectively. In this section are only presented the results of the image reconstructions.

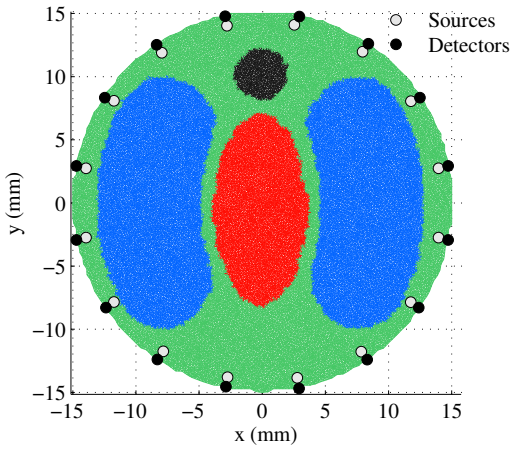

Figure 5.1: Numerical model of a mouse thorax segmented in four regions: muscle (green), lungs (blue), heart (red) and bone (black) and discretized into 19,575 nodes and 8,777 triangular elements.

5.2.1 Two-dimensional mouse thorax numerical model

In this section is presented the implementation in a two-dimension domain. The process of generating the fluorescent forward ROM is similar to the SFD imaging approach presented in Chapter 4 and Chapter 6.

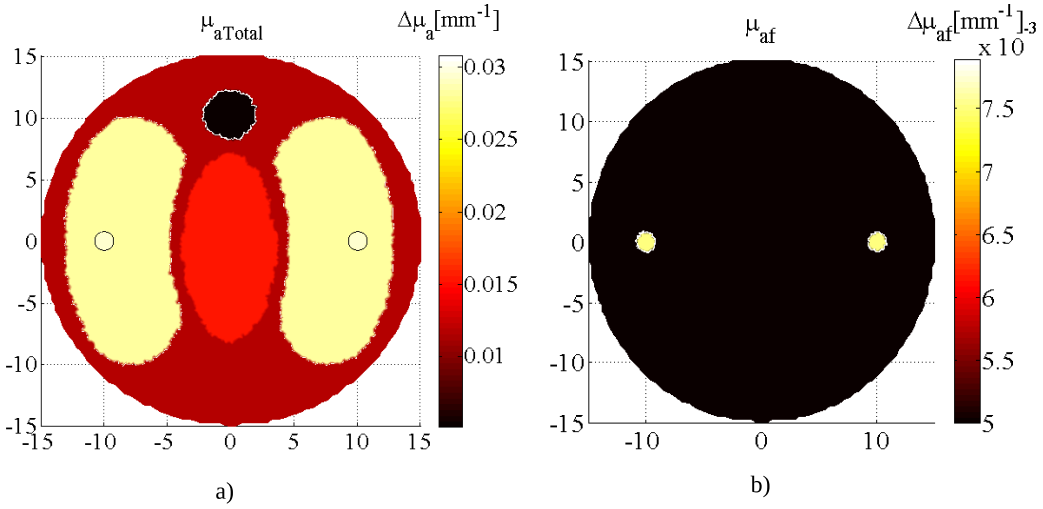

Figure 5.2: Target mouse thorax model used for the image reconstruction. a) Absorption distribution for muscle, lung, heart, bone and tumoural tissue, and b) fluorescence distribution with fluorescent concentration within the tumours.

Figure 5.1 is presented the thorax of a mouse model segmented in four tissue regions: muscle, bone, lungs and heart. It was discretized into 19,575 nodes and 38,777 triangular elements. In Fig. 5.2a is presented the optical property distribution of the target model with two inclusion in each of the lungs representing tumoural tissue. Figure 5.2 presents the fluorescence distribution where the two inclusions located within the lungs of the mouse model.

Table 5.1: Optical properties for the mouse thorax model.

Tissue	$\mu_{a(x,m)}$ [mm^{-1}]	$\mu'_{s(x,m)}$ [mm^{-1}]
Muscle	0.0068	1.081
Lung	0.0233	1.974
Heart	0.0104	1.008
Bone	0.0001	0.060

The optical property distribution is shown in Fig. 5.3a and it is detailed in Table 5.1, these optical values are the average for each tissue structure within the range of [450n, 750nm] and were proposed by Cong&Wang, 2005 [258]. These optical parameters just in this case are the same at both wavelengths. This assumption is used due to fluorescent perturbations are predominant over absorption changes and is consistent with most of the fluorescent markers used in biological tissue [259].

The optical properties of the fluorescent agent for the background are the absorption $\mu_{af} = 0.005\text{mm}^{-1}$ and the quantum efficiency $\eta = 0.16$, considering an uptake distribution of Indocyanine Green (ICG) dye [260]. There are 16 sources and 16 detectors equally distributed around the medium, where the sources are modelled one reduced scattering distance inside the medium.

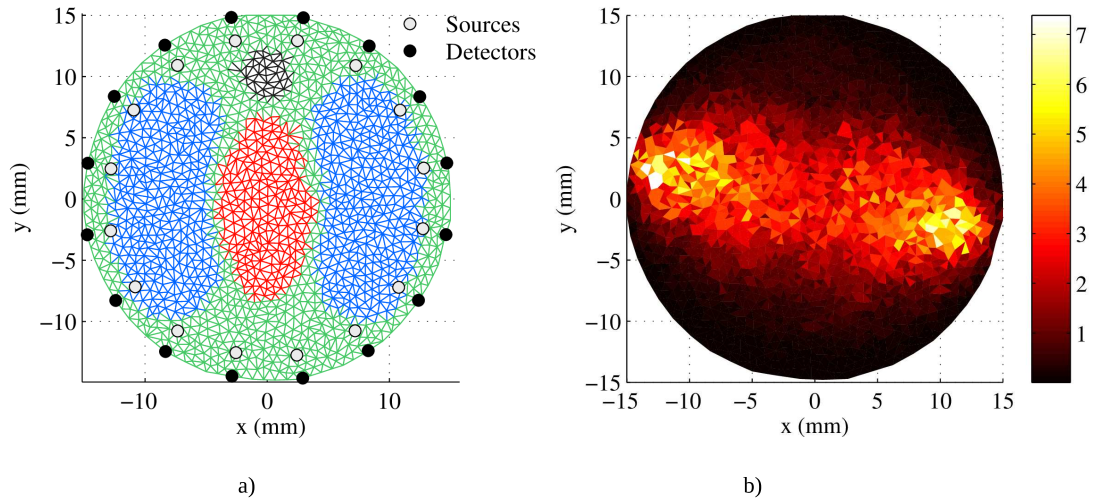

Figure 5.3: Data required for the image reconstruction and ROM generation: a) inverse mesh with *a priori* structural information and b) the Photon Measured Density Functio (PMDF) used to guide the system identification process.

5.2.2 Fluorescence forward ROM formulation for a mouse thorax model

The inverse mesh used for the image reconstruction and for the generation of the fluorescent ROM is shown in Fig. 5.3a. It consists of 1,501 nodes and 2,903 triangular elements.

A second order polynomial model was estimated for each source-detector (SD) pair. To guide the search space of the OFR was analysed the Photon Measurement Density Function (PMDF). All the nodes with less that 5% of contribution to the PMDF were not considered for an specific SD pair, in Fig. 5.3b is presented an example of a PMDF used to generate the ROM from source 1 to detector 9.

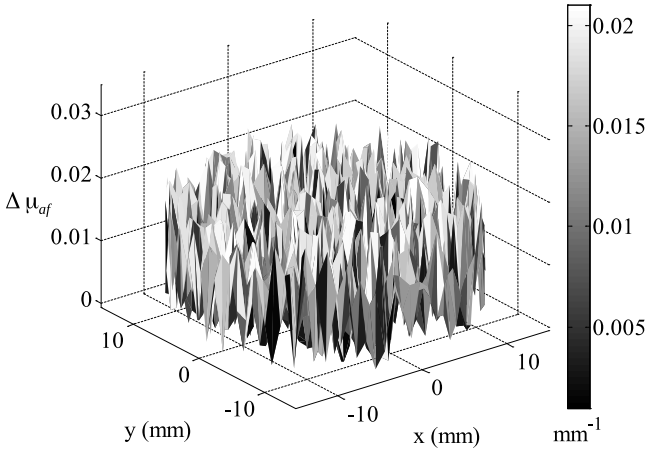

Figure 5.4: Sample of the random absorption values used for ROM estimation.

To generate the input and output data for the identification process was used NIRFAST. A set of 1,000 uniform distributed random values were used as the input for each node in the inverse mesh and the corresponding measurements were recorded as the output data. Figure 5.4 shows one sample of the random input data used.

Model structure detection and parameter estimation were performed consid-

ering the first 500 input/output records. The remaining data was used for model validation. After the system identification process, a total of 240 polynomial models were obtained, one for each source-detector combination. The polynomial structure of these equations are similar to the SFD imaging approach, thus, a sample is omitted in this case.

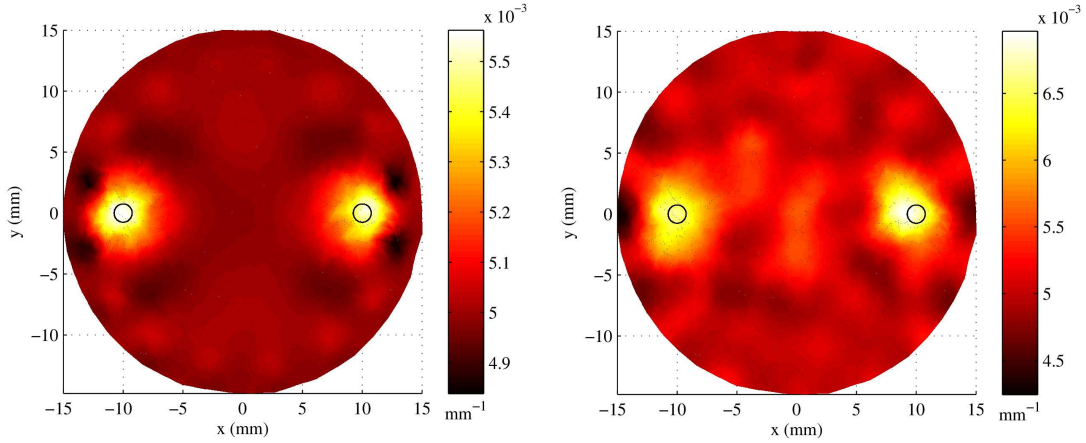

Figure 5.5: Image reconstruction of the fluorescent concentration inside the lungs. a) Using NIRFAST as reference and b) results from the proposed ROM approach.

5.2.3 Image reconstruction evaluation for the 2D mouse thorax model

To validate the proposed approach in Fig. 5.5 are presented the image reconstructions from NIRFAST and ROM. The black circle indicates the real position and the size of the fluorescent concentration. For this reconstruction, to the experimental measurements were added with a 1% of noise. The regularization term in both algorithms was set to 0.5, which offered the best reconstruction capabilities.

It is observed in Fig. 5.5a that NIRFAST presents a more uniform circular shape close to the black circles representing the real location of the anomalies. In contrast, the image reconstruction with ROM presents a non-uniform uniform

reconstruction around the expected anomalies.

For a closer inspection of the image reconstruction, in Fig. 5.6 is presented the vertical profile of the target and the reconstructions with their respective ICCs values. It is observed that ROM is closer to real value but it produces an artifac close to the centre of the medium. In contrast, NIRFAST produces a uniform reconstruction, but its accuracy is lower compared with ROM.

It is important to mention that NIRFAST required 50 seconds and 37 iterations to obtain a single image, while ROM only took 5.7 seconds and 7 iterations to produce good trade-off between the accuracy of the final value and the time required for the reconstruction. Although ROM estimation took over two hours, the important contribution of the proposed approach is during the image reconstruction process.

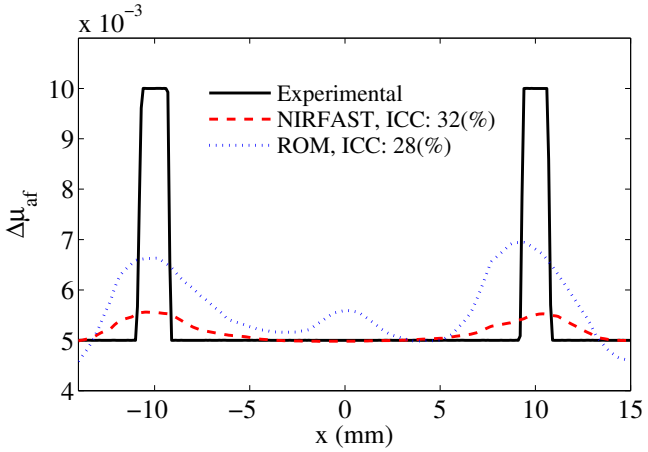

Figure 5.6: Vertical profile comparison of the reconstructions.

5.2.4 Noise effects on the reconstructions

To test the limits of the proposed approach, different values of noise were considered, in Fig. 5.7 are shown the most significant effects found for the reconstruction. It is important to mention that for both algorithms the

regularization parameter was set to λ =0.5. Other values were tested, but this value probed to offer the best results.

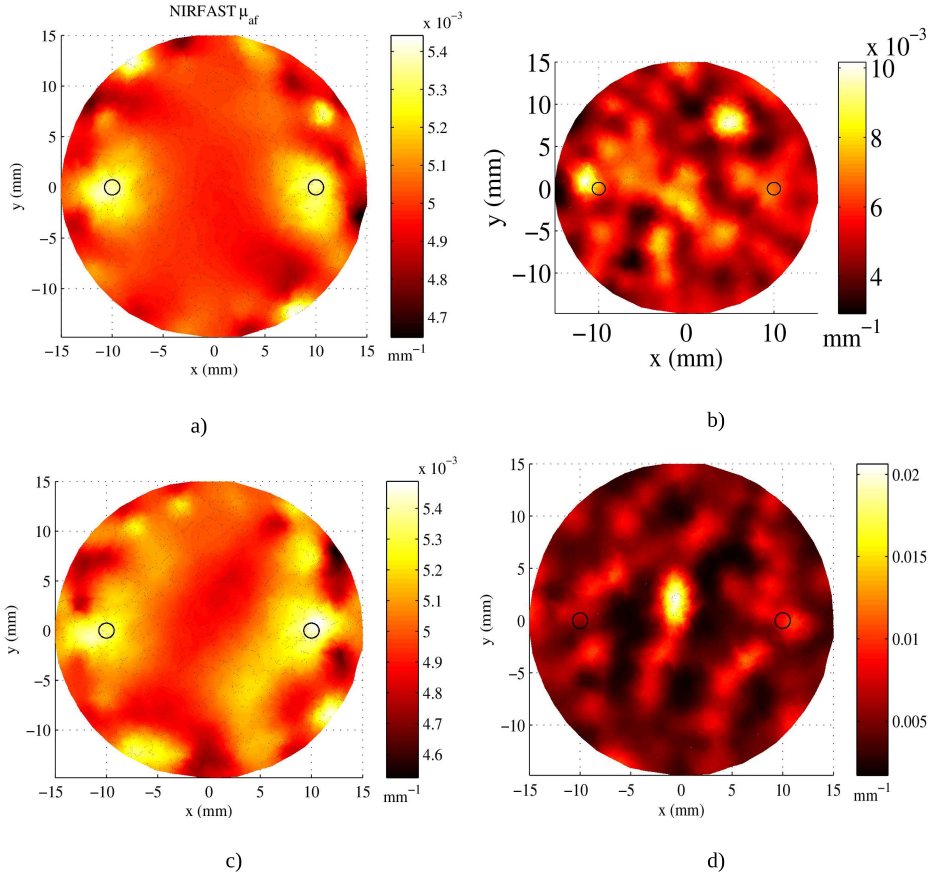

Figure 5.7: Results of the reconstructions for 6% of noise: a) NIRFAST still reconstructs the anomalies but b) ROM only resolves one of the anomalies correctly. At 10% of noise c) NIRFAST slightly recover the location of the fluorescence and d) ROM is not able to reconstruct the anomalies.

As is shown in Fig. 5.7, noise produces a degradation effect over the reconstrucions with a high impact on ROM approach. This can be due to during the estimation process, noise effects were not considered, and although ROM resolved faster, after 6% of noise (Fig. 5.7a and 5.7b) ROM reconstruction failed to recover the location of one of the anomalies, while NIRFAST recovered both of them. In the case of 10% of noise both of the approaches failed to recover the anomalies, but NIRFAST offered a glimpse of where they are located. The reason why tends to fail could be due to noise effects are not considered during

the model estimation, but due to random parameters are used in the formulation they can operate when noise is equal or lower to 5%.

5.3 Three-dimensional image reconstruction in a mouse model

Now is explored the capabilities of the proposed ROM approach to speed up the image reconstruction in a three dimensional medium. The procedure to generate the fluorescence ROM is illustrated using the heterogeneous thorax model presented in Fig. 5.8a. This model is a cylinder with 30 mm in diameter and 30 mm in height and is segmented in four regions: muscle, bone, lunngs and heart tissues.

The optical parameters at both the excitation and emission wavelengths are listed in Table 5.2 and the background fluorescence absorption was set as $\mu_{af} = 0.005\text{mm}^{-1}$ and quantum efficiency $\eta = 0.16$ considering the ICG optical properties [258].

An array of 25 sources and 25 detectors in a honeycomb pattern [64, 108] is located over the right lung region resulting in 600 source-detector pair combinations where no measurements were considered from a source located at the same place of a detector. The excitation light is modelled as isotropic point sources located one reduced scattering distance $1/\mu_s^{'}$ beneath the surface. The medium was discretized into 16,972 tetrahedral elements and 3,261 nodes.

Table 5.2: Optical properties for the 3D mouse thorax model.

Tissue	$\mu_{a(x)}$	$\mu_{s(x)}^{'}$	$\mu_{a(m)}$	$\mu_{s(m)}^{'}$
Muscle	0.0052	1.08	0.0068	1.03
Lung	0.0133	1.97	0.0203	1.95
Heart	0.0083	1.01	0.0104	0.99
Bone	0.0024	1.75	0.0035	1.61

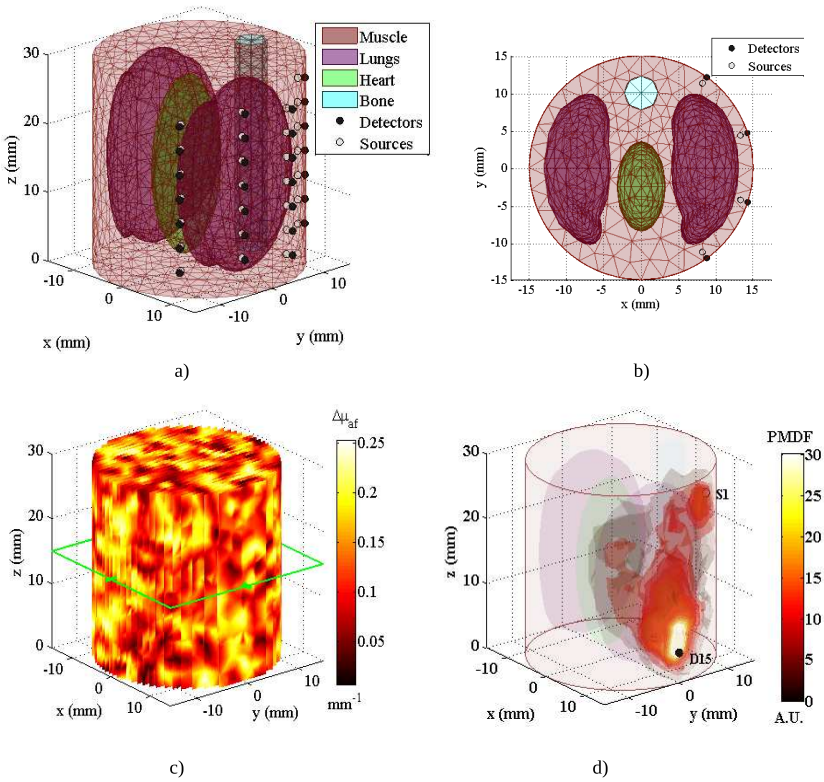

Figure 5.8: a) Coarse mesh used for the image reconstruction and fluorescence forward ROM formulation it is observed the location of the sources and detectors on onse side of the thorax model. b) upper view of the medium showing the location of the sources modelled at one reduced scattering distance inside the medium, c) three-dimensional view of the random absorption values used as inputs to the ROM formulation and d) PMDF used to guide the OFR algorithm.

To generate the forward ROM, a sequence of 1000 normally distributed random fluorescent absorption values were used to compute fluorescence measurements using the FEM approximation of the fluorescence diffusion equation. A set of 500 records were used as data estimation and the remaining set for model validation.

The minimum value of the random sequence corresponds to the background fluorescent absorption value and the maximum value was set as μ_{af}^{max} considering the optical response of ICG at 780nm and 830nm [261] One sample of the normally distributed random data throughout the medium is presented in Fig. 5.8b and Fig. 5.8c. A second order polynomial model was estimated for each source-

detector pair using the OFR and the PMDF o guide the structure detection, those nodes within a 5% threshold were selected as the input nodes to the model. Fig. 5.8d hows the PMDF from source 1 to detector 15 indicating the region of nodes to be considered in the model.

The proposed model considered 3,261 inputs and second order polynomial functions, resulting in 534,640 candidate monomial terms. However, the resulting model for each source-detector pair is smaller by the use of the OFR algorithm. For example, the model estimated for source 1 and detector 15 consists only of 113 terms.

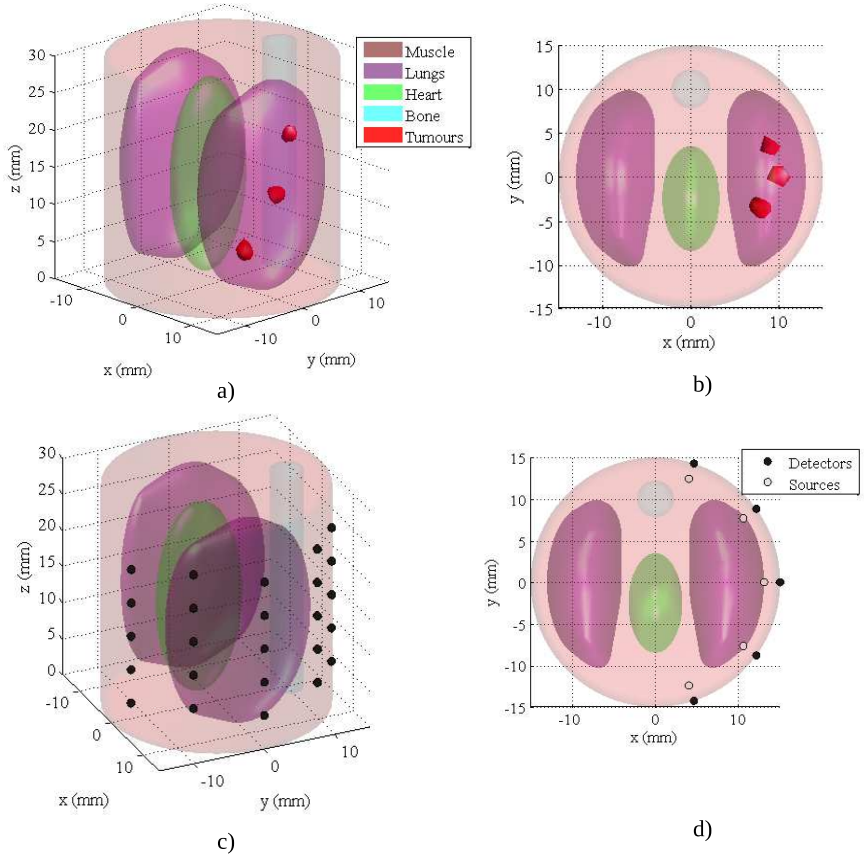

Figure 5.9: a) Target medium consisting of four main tissue regions and three anomalies, b) Upper view of the medium showing the distribution of the anomalies. c) set of source-detector (SD) pairs located on one side of the medium and d) upper view of the SD pairs where the sources are located one reduced scattering coefficient inside the medium.

5.3.1 Three-dimensional mouse thorax model with three tumours

To test the above forward model was used a cylindrical mouse thorax numerical model with three inclusions in the right lung as can be seen in Fig 5.9. It was discretized in 99,750 tetrahedral elements and 11,490 nodes. Sources and detectors were located at the same position of the inverse mesh, see Fig. 5.9c and Fig. 5.9d, and the optical properties were set with respect to Table 5.2. To the measurements a 1% of uniform distributed noise was added to test the ROM capabilities.

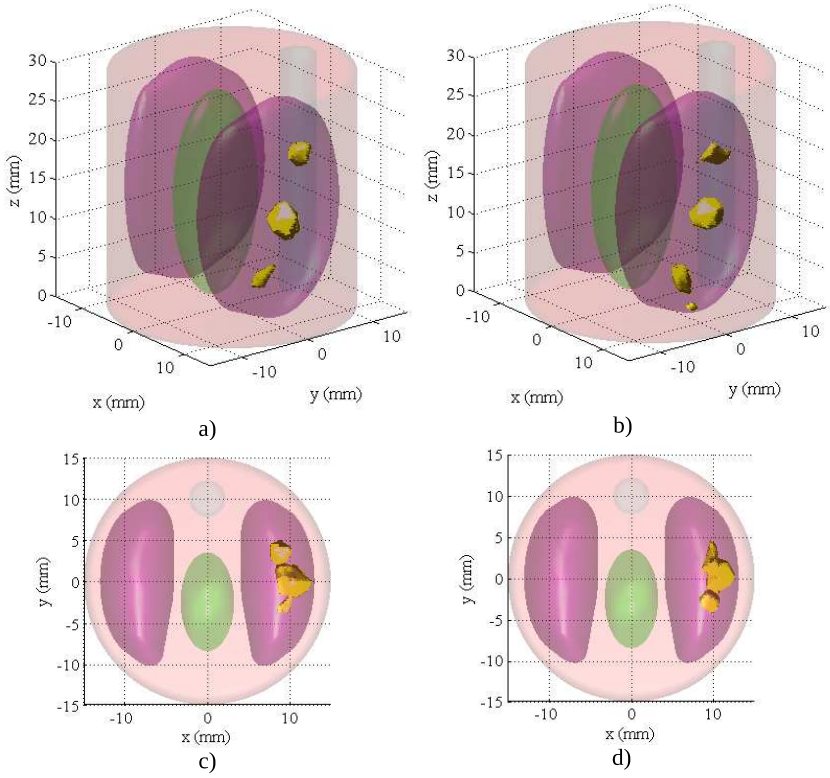

Figure 5.10: Image reconstructions from a) NIRFAST three dimensional view, b) NIRFAST top view, c) ROM three dimensional view and d) ROM top view.

5.3.2 Image reconstruction of three static tumours in the lung of the mouse model

As in the previous section, NIRFAST was used to implement the fluorescent forward ROM and also as the reference to compare the image reconstruction. It is observed in Fig. 5.5 that both algorithms located the three anomalies. The regularization parameter was set to $\lambda = 0.1$ in both algorithms to have the same conditions and a way to compare their performance. In this case, NIRFAST required 75 seconds to perform the reconstruction meanwhile ROM performed the reconsruction in only 8 seconds, although model estimation took around 16 hours.

To uncover the limits of ROM, the noise of the measured signal was increased until ROM started to fail in the reconstruction of the anomalies. When the noise reached the 4% NIRFAST recovered the location of the anomalies but overestimated the size of the inclusions, see Fig. 5.11. ROM was able to recover the region where the anomalies are present and offered an idea of the volumes where the fluorescent marker presents a higher concentration.

In Fig. 5.11 the noise is further increased to a 6%, NIRFAST was able to locate the region where the fluorescent marker is located, but no clear separation of the tumours is provided. On the contrary, ROM was unable to recover the information of the fluorescent marker that tagged the tumours.

As can be observed, the noise effects on the 3D reconstruction are more drastic, compared with the 2D image reconstruction, one possible reason for this behaviour is due to the complexity and the size of the target medium. Another reason is that only one side of the mouse thorax is scanned, then no information is obtained from the other side of the medium that could improve the reconstruction.

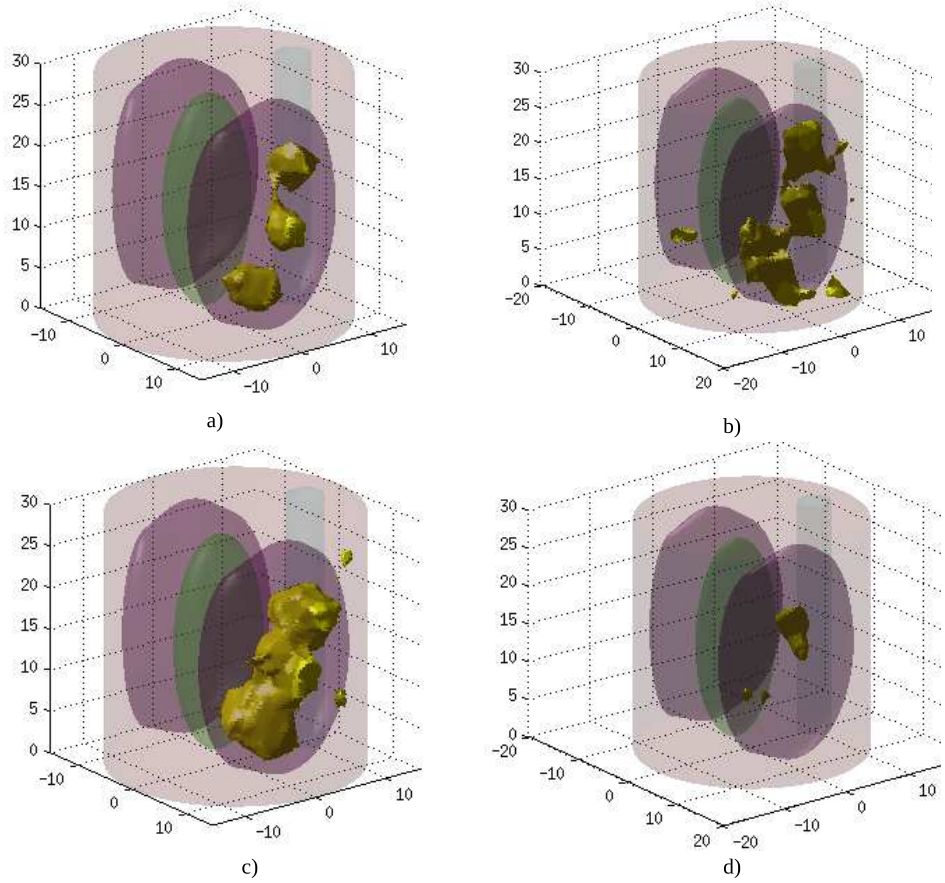

Figure 5.11: Noise effects on 3D reconstructions. At 4% of noise, a) NIRFAST locates the tumours but overestimated the size of the anomalies, b) ROM offered a glimpse of where the fluorescent agent is more concentrated. At 6% NIRFAST detected the region and d) ROM is not able to reconstruct the anomalies.

5.3.3 Image reconstruction of a time-varying fluorescent concentration in the lung's tumours of the mouse

To test the real-time capabilities of ROM, it is used a quasi-periodic signal for the fluorescent absorption in the anomalies. The optical parameters are the same from the mediums above explored, the regularization is $\lambda = 0.1$ and is considered 1% of noise in the measurements. The result of 100 samples points of a quasiperiodic signal is presented in Fig. 5.12. The quasiperiodic variation is injected in the three anomalies to analyse the speed and the accuracy of each medium.

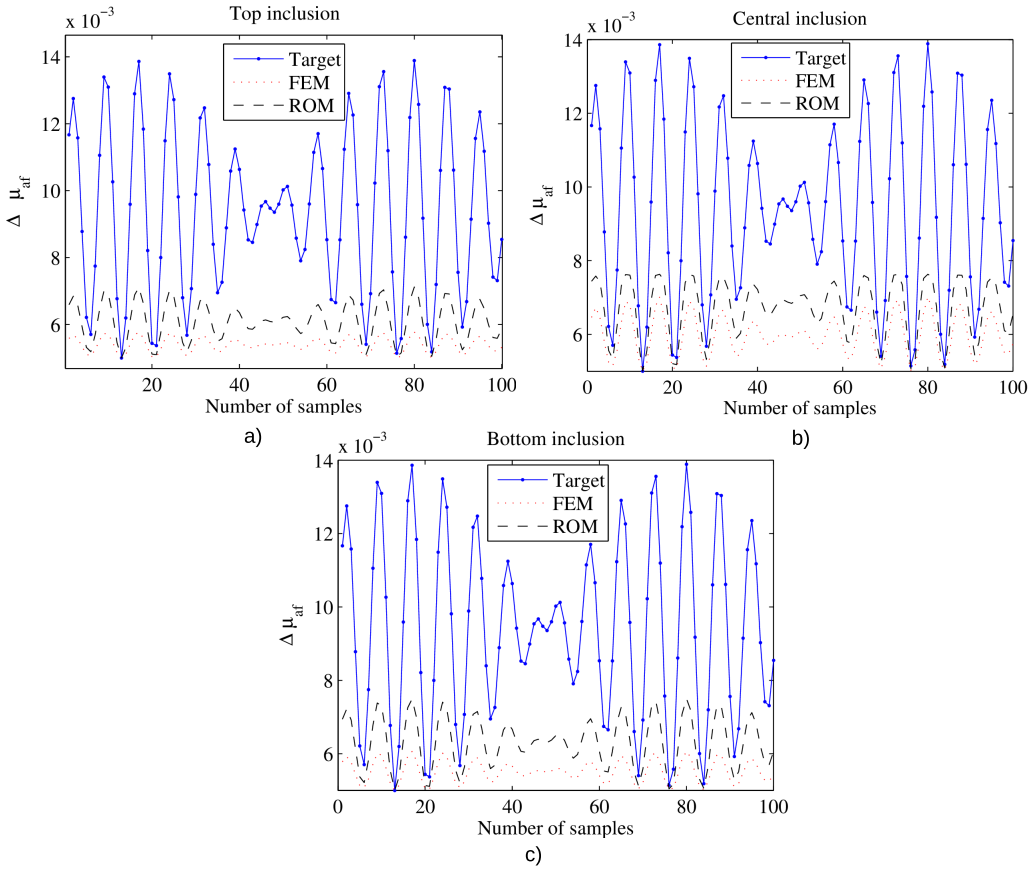

Figure 5.12: Dynamic image reconstruction of the fluorophore concentration from. a) Top tumour, b) middle tumour and c) bottom tumour.

In the three graphics presented in Fig. 5.12 the value tracked was the higher one obtained within each reconstructed anomaly. It can be observed that NIRFAST and ROM follow the behaviour of the fluorescent concentration, but underestimate the expected value of the quasi-periodic signal injected in each anomaly. Note that ROM obtained a higher value and also took 10 minutes to reconstruct the full time series. In contrast, NIRFAST presented a lower fluorescent absorption reconstruction and took over two hours to finalize the reconstruction of the 100 samples.

5.4 Conclusions

To the knowledge of the author, the work presented along this chapter correspond to the first time that input-output data are used to create simplified models to describe fluorescent re-emitted light to perform the image reconstruction from exogenous optical properties at two different wavelengths of operation being the excitation wavelength the one that excited the fluorescent marker to emit light at a different wavelength where the ROM approach described the fluorophore properties.

Previous work related to the ROM theory focused on the reconstruction of the absorption parameters at a single wavelength of operation. Its main application is related to functional reconstruction of brain activity. In contrast, this work extended the ROM approach to target exogenous optical properties at a different wavelength than the light source used to illuminate the medium.

Our results demonstrate that tomographic reconstructions for tracking fluorescent perfusion can be performed in a fraction of the time using ROM approach compared with the FEM solution presented by NIRFAST. In the study cases above presented, all the anomalies were precisely located, although the fluorescent estimated values were not accurately obtained the proposed ROM approach showed a good trade-off between the quality of the image, the accuracy of the estimated value and the time required for the reconstruction.

In the two-dimensional case, the image reconstruction based-on ROM was reduced close to a tenth of the time required by NIRFAST, although the creation of the models took around two hours, it is possible to run continuous tests over the subject with no necessity of calibration due to the robust structure of the models used consider uncertainties during their formulation.

The main contribution of ROM to the FDOT modality is related to the reconstruction fluorescent target of relatively large 3D domains with heterogeneous optical property distribution close to a real-time reconstruction using a personal computer with no extra hardware or an expensive processor. This is demonstrated by the image reconstruction presented in this chapter consisting on the thorax of a mouse model with a diameter of 30cm and a height as well of 30cm and three tumors inside the lung.

By using an array of 25 sources and 25 detectors, which could be considered a large set of source-detector pairs, the image reconstruction of polynomial ROM took only 8 seconds, while NIRFAST considering a full FEM mesh took 75 seconds for a single image. Thus, the use of solvers that consider full meshes are not able to perform real-time reconstructions using a personal computer. Although ROM estimation takes time, once the models are obtained, they can be directly implemented and be used between trials with the test subject due to the robust capabilities of the estimated model. In other words, it is possible to monitor a medical treatment or to detect physiological changes for a specific subject once the ROM have been obtained for that subject.

With the above results, it has been demonstrated the capability of ROM to perform close-to-real time image reconstruction without the necessity of specialized computers or expensive GPUs. It is only required CPU processing to perform the image reconstruction in a normal desktop. The main advantage is the direct estimation of the fluorescence absorption from boundary measurements at the emission wavelength, thus requiring only the sources to operate on the excitation wavelength of the fluorescent marker, and then only measuring the emitted light from the fluorescence generated to later estimate the location of the fluorescent target.

It is assumed that using a dense inverse mesh with a faster CPU and higher RAM capacity the accuracy could be improved and the reconstruction time could be reduced. But this solution also increase the costs of the system implementation and commercialization. With the approach proposed in this work, there is no necessity to invest on expensive computers or additional hardware.

One limitation that ROM presents is the time required for the estimation of the model, taking several hours in a normal computer and using code wrote in Matlab. One possible solution to overcome the limitation is the use of C/C++ coding which is an specialized language for iterative executions, being an iterative process the way how the polynomial models are estimated. Another solution could be the implementation of the estimation in FGPAs specifically programmed to estimate the models and also to perform the image reconstruction process.

.

Chapter 6

Diffuse optical tomography using spatial frequency domain imaging

6.1 Introduction

Near-infrared spectroscopy (NIRS) and diffuse optical tomography (DOT) are two of the main diffuse optical imaging (DOI) approaches used to characterize biological chromophores such as oxy-hemoglobin HbO_2, deoxy-haemoglobin (HbR), water content and lipids from the quantification of absorption and scattering coefficient variations [262, 163].

NIRS uses a wide content from spectral and temporal domains with a limited number of source-detector (SD) measurements. In principle, NIRS can't provide sensitive information from depth tissue, because of the SD configuration used that limits depth information [138, 121, 21]. This is normally addressed by increasing SD distance separation which leads to a reduction in the spatial resolution [263].

In contrast, DOT approaches utilize a limited number of wavelengths (4-6) and a constrained temporal information with large SD arrays to obtain high resolution images. However, DOT instrumentation is expensive and complex compared with

NIRS equipment [263, 264].

Spatial frequency domain (SFD) imaging is a novel approach that can be used to perform tomographic reconstructions without the need of a large array of detectors with wide dynamic range. This approach measures the optical properties of a high scattering medium by projecting structured light on the medium and by measuring its spatial phase shift [265, 266, 49].

This approach exploits the fact that many biological tissues are made up of layers (i.e. skin, skull and brain cortex) and that tissue optical properties do not vary with the depth within each layer [267, 268]. The method resolves the layers individually and is able to characterize the optical properties in an entire field-of-view at once [269, 270].

Spatial Frequency Domain imaging has been mainly used in topographic image reconstructions of human and animal skin [270, 271, 265, 272], rodents cortex [273, 50], to study tissue oxygenation [274, 265], postoperative tissue recovery [275], skin burns [51], and *in vivo* and surgically resected breast tissue [276, 277, 262]. By creating a map of a planar image reconstructions, depth tissue information from inner layers is projected at the surface of the medium, thus simplifying optical property recovery, but limiting the tomographic capabilities.

One solution to improve depth optical property recovery is through a calibration process that matches the reflectance between the target medium and a multilayer simulation model [272]. The disadvantage of this method is that it requires several calibrations which are further increased with the number of layers considered and thus, increasing the complexity of the approach.

Three-dimensional applications of this approach include the profile character-

ization of phantoms, *in vivo* tissue [278, 269] and the image reconstructions from inclusions embedded in homogeneous mediums [279, 280, 281, 279]

The limitations of SFDI are related to the spatial characterization of depth tissue and that it is unable to perform continuous image reconstructions from varying signals. These are due to the lack of mathematical models used to describe modulated light behaviour in depth tissue and the time required for data acquisition and the demodulation process.

To address current challenges and limitations of this imaging technique, researches have investigated:

- the use of mirrors, lenses and lasers around the target medium, but these greatly increase the complexity and the cost of the system [54],
- alternative patterns of illumination from the more commonly used sinusoidal pattern [282, 283, 281],
- the effects of patterned light illumination for quantifying inclusions tagged with fluorescent markers [284, 285, 286] and
- the application of a tomographic approach that exploits the theoretical framework of diffuse optical tomography. [279].

This chapter introduces a new reconstruction method to obtain tomographic images from biological tissue with a wide field-of-view using a spatially modulated light source and a CCD camera. The proposed method makes use of the ROM approach presented in Chapter 4 to describe light propagation within the tissue layers. Then, this model is used within an iterative reconstruction algorithm to update the initial guess of optical properties until a tomographic image of the optical properties is obtained.

A second contribution to the SFDI field is the use of the virtual sensor theory for the CCD camera operation. This technique is norally used in CCD cameras to simplify its operation and improve data processing. The virtual sensor methodology assumes that a finite number of pixels on the CCD camera are used as a single measurement point instead of using each pixel to measure reflected light. With this approach is it possible to simplify the operation of a CCD camera and to control the data that is measured.

As is going to be presented in this chapter, virtual sensor theory could be considered an important contribution for both the SFDI imaging and to the ROM approach. To the knowledge of the author and by the time this work was written the use of the virtual sensor on CCD cameras was not used before in combination with Spatial Frequency Domain Imaging or to formulate Reduced Order Models in any other Diffuse Optical Imaging modality.

6.2 Instrumentation

It has been demonstrated that diffuse reflectance intensity decay depends upon the optical properties of a medium [201]. The intensity decay is also referred as the spatial Point Spread Function (s-PSF) and its measurement can be used to estimate the optical properties of a target medium [287].

An alternative method to characterize the spatial dependant intensity decay is by the spatial Modulation Transfer Function (s-MTF) [276], which is the Fourier equivalent of the s-PSF in the frequency domain [262, 288]. The method measures the AC-amplitude attenuation of a spatially modulated illumination projected to a turbid medium [265].

SFD imaging instrumentation was first introduced by Dögniz in 1998 [289],

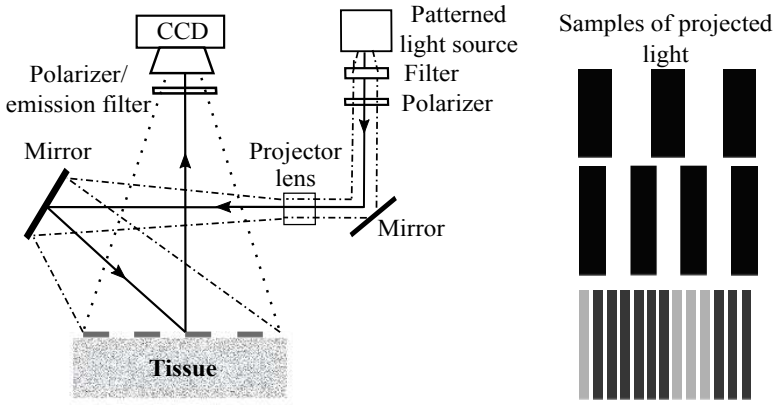

Figure 6.1: Schematic of a spatial frequency domain imaging system proposed by the group of Cuccia [49].

and to this day there have not been many changes from his proposed equipment. The schematic of a SMLI instrument, presented in Fig. 6.1, consists of [270, 278]:

- a source of illumination from a xenon/tungsten-halogen lamp that is spatially modulated,
- a set of bandpass filters ranging from 400-1050 nm,
- mirrors used to illuminate the sample at an angle of $\alpha = 7^{\circ}$ to avoid specular reflection,
- polarisers placed at the source and the detector device to further reduce specular reflection,
- a tunable filter $(\lambda = 650 - 1100nm, \Delta\Lambda = 10nm)$,
- a CCD camera of 12 or 16 bits used to collect the reflected light
- and a computer used to control data acquisition and to perform image processing.

6.3 Light propagation model considering a spatial modulated light source

To solve the forward problem considering a spatial modulated source the CW diffusion equation is used in the form [272]

$$-\Delta \cdot \kappa(r)\Delta\Phi(r) + \mu_a(r) = S \tag{6.1}$$

where the terms μ_a, κ and the corresponding boundary condition were defined in Section 3.3.2. The source term S differs from the one presented in Eq. (3.15) and is defined as a sinusoidal fringe pattern given by

$$S = S_0[1/2 + Msin(2\pi f_i x + \alpha)] \tag{6.2}$$

where S_0 is the light intensity, M the modulation depth, f_x the spatial frequency, x is a point on the surface of the medium and α is the spatial phase angle. The light source is assumed to be located at one reduced scattering distance from the boundary.

The measured photon fluence at the surface is given by [201]

$$R(\xi) = -\Delta\phi(\xi, z)|_{z=0}. \tag{6.3}$$

Each illumination pattern in Eq. (6.2) is three times phase shifted at $\alpha = 0, 2/3\pi, 4/3\pi$ rad. The resulting intesities, $R_{j,alpha}$ are then demodulated using

$$\begin{aligned} R_{ac}(x,y) = \frac{2^{1/2}}{3}[&(R_{i,0}(x,y) - r_{i,2/3\pi})^2 + (R_{i,2/3\pi}(x,y) - r_{i,4/3\pi})^2 \\ &+ (R_{i,4/3\pi}(x,y) - r_{i,0})^2]^{1/2} \end{aligned} \tag{6.4}$$

where index i accounts for the i-th pixel measurement at the (x, y) position. This demodulation allows to treat the reflectance at each pixel independently [49, 274].

6.4 Image reconstruction

To recover the optical property distribution it is used the iterative image reconstruction with regularization and structural *prior* information to improve the accuracy of the reconstruction as depicted in Section 4.2.1.

The objective function is given by

$$\chi = \min_{\mu} \left\{ \sum_{i=1}^{N_{meas}} (\ln R_i^{meas} - \ln R_i^{calc})^2 + \lambda \sum_{i=1}^{N_{nodes}} (\mu - \mu_0)^2 \right\} \tag{6.5}$$

where N_{meas} is the number of measurements, $Nnodes$ the number of unknowns, $\ln R_i^{meas}$ and $\ln R_i^{calc}$ are the logarithmic of the experimental and model calculated reflectance measurements, respectively [236], μ_0 is an initial guess of the optical properties and λ is the regularization term. In this work, it is defined $\mu = \mu_a$ due to physiological the absorption coefficient is affected by physiological changes [21].

Minimizing Eq. (6.5) by setting the first derivatives with respect to μ to zero and using a Levenberg-Marquardt (LM) regularization with $\delta\mu = \mu - \mu_0$ yields to the update function

$$(J^T J + \lambda I)(\delta\mu) = J^T(\ln R_i^{meas} - \ln R_i^{calc}) \tag{6.6}$$

where J is the Jacobian matrix, the regularization term λ reduced at each iteration by a factor of $10^{0.25}$ and scaled by the maximum of diag$(J^T J)$ [290, 22].

6.5 Reduced order models with spatial modulated light source

The necessity to record three angular shifts for each spatial frequency used at each optical wavelength, yields to the SFD imaging approach to take up to

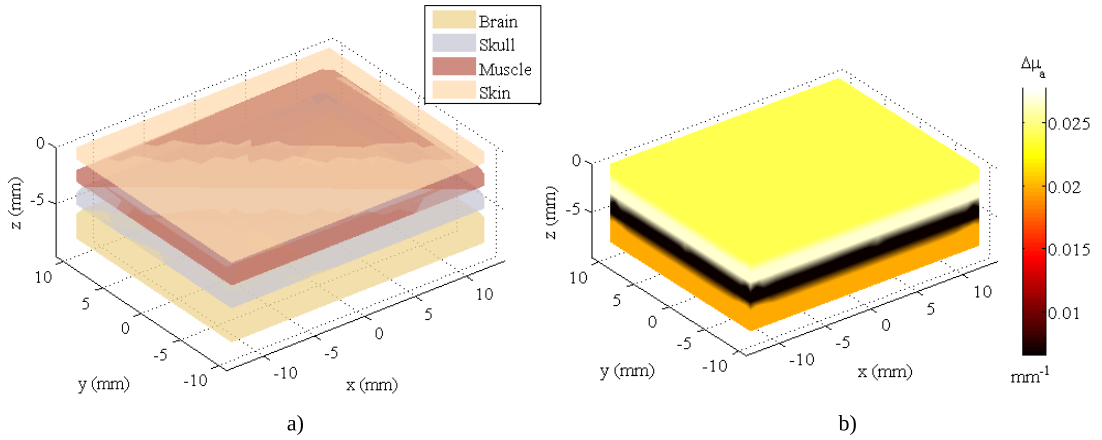

Figure 6.2: Human head section model: a) tissue regions considered in the numerical simulation and b) distribution of the absorption coefficient along the medium.

six times longer than diffuse optical topography image reconstructions [291]. Therefore, it is demonstrated in this work that the time required for tomographic reconstructions is exponentially increased due to the number of nodes used in the inverse mesh.

6.5.1 Human head simulation model

To speed up the image reconstruction process it is proposed the use of the reduced order models (ROM) approach. To test the tomographic capabilities of SFD imaging with ROM approach, a numerical model of a human head section segmented in four tissue regions is used, see Fig. (6.2)a. The medium was discretized in a fine mesh consisting of 17,107 tetrahedral elements and 3,491 nodes.

Table 6.1: Optical properties for the head model.

Tissue	μ_a [mm^{-1}]	$\mu_s^{'}$ [mm^{-1}]
Skin	0.02	0.50
Muscle	0.022	1.0
Skull	0.005	1.63
Brain	0.015	1.63

The optical properties of the model are presented in Table 6.1 and correspond to real tissue parameters found in the near-infrared spectrum [243]. Figure 6.2b

shows the distribution of the absorption coefficient for each tissue in the model.

Light reflectance measurements were generated by simulating the instrumental set-up shown in Fig. 6.1 considering a 16-bit couple-charge device (CCD) camera. Light propagation was calculated for six spatial frequencies ranging from 0 to 3 mm^{-1} projected at three phase angles: 0, $2/3\pi$ and $4/3\pi$ [292, 293].

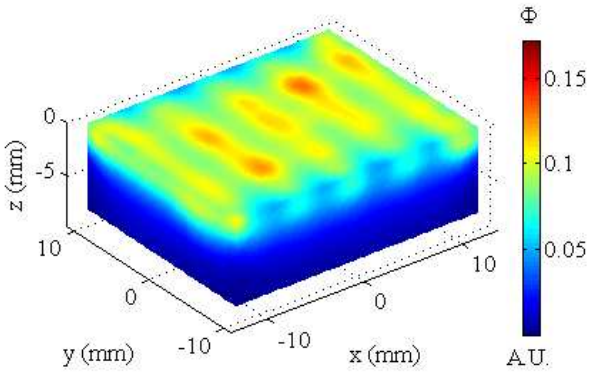

Figure 6.3: Light propagation with spatial frequency $f_x = 0.18$ and $\alpha = 2/3\pi$.

The software NIRFAST was used to simulate the light propagation through the human head section. The boundary condition was modified to account for the spatial modulated light source projected over the surface of the domain, where Fig. 6.3 shows one sample of the light propagation through the medium.

6.5.2 Reduced Order Models formulation

Typically, in reflectance diffuse optical tomography, deep tissue optical properties are recovered using each pixel of a CCD camera, or a group of pixels, as a single detector [228, 236, 294, 259, 295]. Once a set of measurements is obtained, the image reconstruction scheme utilizes a two step iterative scheme in order to recover the optical properties as shown in Fig. (3.3).

This iterative method has the drawback that calculates the light propagation

and the light measurements in two stages. Besides, it uses all the available nodes in the inverse mesh which increase the complexity of the inversion process and the time required for the image reconstruction [64].

It has been demonstrated that use of ROM approach reduces the time required in DOT reconstructions based-on fiber-optic instrumentation [65]. In this work is extended the ROM approach to non-contact reflectance DOT. For this purpose, one model is generated for a group of pixels that serve as a single detector in order to map the optical properties from deep tissue.

NIRFAST software was used to generate the input and output data required for the estimation of the polynomial approximation of the SFD forward model given by Eq. (6.1), Eq. (6.2) and Eq. (6.2). The inverse mesh used consisted of 5,968 elements and 1,377 nodes and had the same spatial distribution as the fine mesh used to generate the experimental measurements.

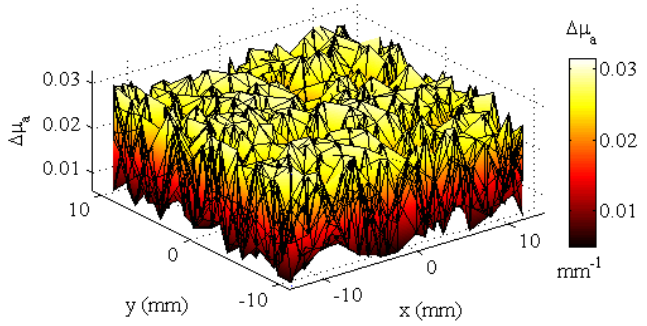

Figure 6.4: Random absorption values used as inputs used to generate the polynomial models.

The input data were 1,000 uniform distributed random absorption values at each node in the inverse mesh for each one of the spatial frequencies and each angular shift, see Fig. 6.4 for one sample of the input data.

For the output data, the reflectance measurements were obtained by 16 virtual

detectors. This technique combines the pixels on a CCD camera via averaging to produce a single measurement [156, 296], see Fig. 6.5. Other approaches to create CCD detectors include pixel binning and virtual detector in conjunction with varying integration times. Details of these approaches can be found in [297, 131].

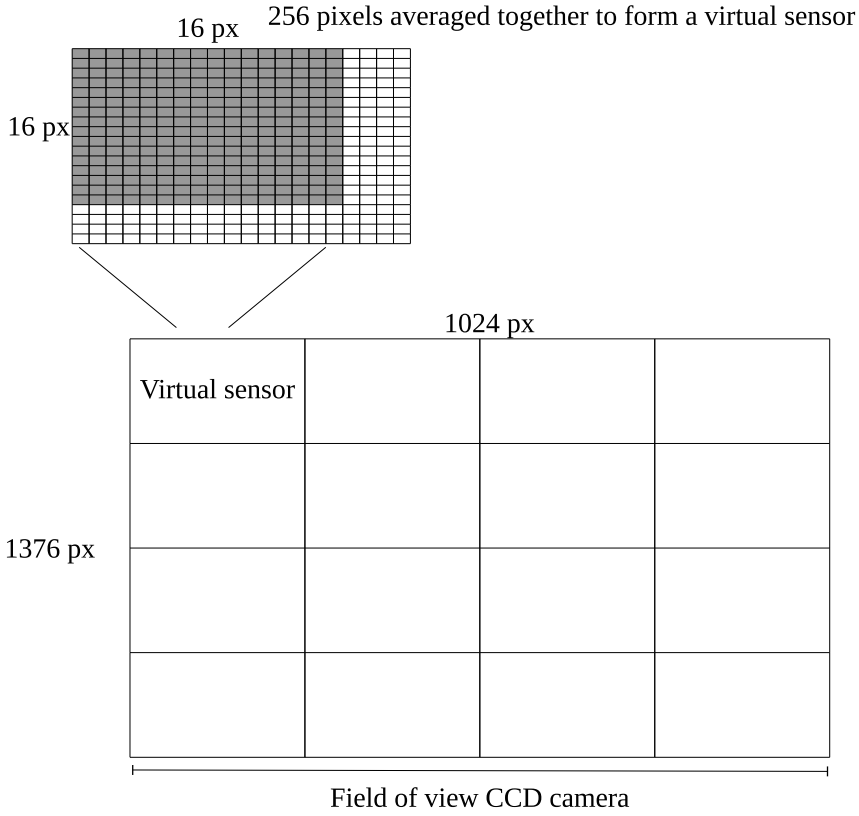

Figure 6.5: Example of the virtual sensor approach used for measuring the reflectance from the numerical model.

For each virtual detector, a polynomial reduced order model was generated in the form

$$R_{i,f_x,\alpha} = f(S_{f_x,\alpha}, \mu_a(k)) \tag{6.7}$$

where f represent the forward reduced order models, indices $i = 1, ..., 16$ and $k = 1, ..., 1,377$ are the sources and the nodes in the mesh, respectively. Then, by considering 16 outputs, six spatial frequencies, three angular shifts, 1,377 nodes

from the inverse mesh and second order monomial terms, the total number of candidate terms is 274,034,880.

Model structure detection and parameter estimation were performed using the OFR algorithm that computed the Error Reduction Ratio (ERR) for each candidate term with a *cut-off* value of $C_d = 0.05$ [64]. In Table 6.2

Table 6.2: Parameters for one output of the forward reduced order models with spatial frequency modulated illumination.

θ_i	Term	θ_i	Term	θ_i	Term
0.00942		-0.0233	$u_{0317}u_{0364}$	0.02	$u_{0664}u_{1213}$
-0.117	$u_{0440}u_{0512}$	-0.0411	$u_{0447}u_{0729}$	-0.0118	$u_{0284}u_{0428}$
-0.047	$u_{0431}u_{0441}$	-0.0528	$u_{0431}u_{0491}$	-0.0192	$u_{0363}u_{0448}$
-0.0497	$u_{0396}u_{0515}$	-0.0224	$u_{0275}u_{0523}$	-0.0305	$u_{0331}u_{1063}$
-0.124	$u_{0291}u_{0660}$	-0.0116	$u_{0403}u_{0967}$	-0.0367	$u_{0415}u_{0516}$
-0.134	$u_{0395}u_{0592}$	-0.0386	$u_{0285}u_{0430}$	-0.0201	$u_{0638}u_{1073}$
-0.144	$u_{0401}u_{0432}$	-0.0429	$u_{0410}u_{0780}$	0.0262	$u_{0756}u_{0952}$
-0.125	$u_{0289}u_{0429}$	-0.0398	$u_{0277}u_{0781}$	-0.0677	$u_{0431}u_{0515}$
-0.107	$u_{0274}u_{0391}$	-0.0361	$u_{0312}u_{0313}$	-0.0851	$u_{0396}u_{0396}$
-0.0501	$u_{0399}u_{0591}$	-0.0448	$u_{0513}u_{0762}$	-0.0929	$u_{0399}u_{0515}$
-0.0653	$u_{0325}u_{0390}$	-0.0273	$u_{0330}u_{0760}$	-0.0453	$u_{0286}u_{0591}$
-0.0936	$u_{0516}u_{0582}$	-0.031	$u_{0366}u_{0662}$	-0.0316	$u_{0532}u_{0666}$
-0.0537	$u_{0287}u_{0583}$	0.0199	$u_{0904}u_{0968}$	-0.0188	$u_{0911}u_{0965}$
-0.0886	$u_{0407}u_{0517}$	-0.0362	$u_{0597}u_{0721}$	-0.0564	$u_{0287}u_{0512}$
-0.104	$u_{0397}u_{0661}$	-0.061	$u_{0292}u_{0441}$	-0.0419	$u_{0518}u_{0583}$
-0.0661	$u_{0393}u_{0404}$	-0.0551	$u_{0444}u_{0512}$	-0.0269	$u_{0395}u_{1049}$
-0.0797	$u_{0284}u_{0728}$	-0.0406	$u_{0521}u_{1072}$	-0.0269	$u_{0592}u_{1267}$
-0.0537	$u_{0169}u_{0492}$	-0.0608	$u_{0440}u_{0590}$	-0.0195	$u_{0442}u_{0834}$
-0.0417	$u_{0322}u_{0662}$	-0.0402	$u_{0323}u_{0408}$	-0.0334	$u_{0591}u_{0838}$

Table 6.2: (continuation)

θ_i	Term	θ_i	Term	θ_i	Term
-0.0602	$u_{0282}u_{0665}$	-0.0261	$u_{0314}u_{1030}$	-0.0215	$u_{0308}u_{0674}$
-0.0635	$u_{0324}u_{0400}$	-0.0299	$u_{0404}u_{0593}$	0.0205	$u_{0936}u_{1373}$
-0.0671	$u_{0279}u_{0581}$	-0.0361	$u_{0276}u_{0591}$	-0.00814	$u_{0867}u_{0881}$
-0.0715	$u_{0438}u_{0522}$	-0.0696	$u_{0431}u_{0512}$	0.0189	$u_{0415}u_{0604}$
-0.0663	$u_{0310}u_{0402}$	-0.106	$u_{0440}u_{0441}$	-0.0288	$u_{0865}u_{1038}$
-0.0531	$u_{0443}u_{0664}$	-0.0411	$u_{0321}u_{0672}$	-0.0118	$u_{0791}u_{1217}$
-0.0452	$u_{0437}u_{0595}$	-0.0306	$u_{0670}u_{0727}$	-0.0198	$u_{0403}u_{0789}$
-0.0597	$u_{0398}u_{0634}$	-0.0218	$u_{0509}u_{0518}$	-0.062	$u_{0325}u_{0959}$
-0.0282	$u_{0452}u_{0518}$	0.0478	$u_{0288}u_{1153}$	-0.0575	$u_{0390}u_{0640}$
-0.0381	$u_{0446}u_{0519}$	-0.0356	$u_{0494}u_{0530}$	0.0364	$u_{0640}u_{0959}$
-0.0587	$u_{0327}u_{0779}$	-0.0374	$u_{0589}u_{1339}$	0.0337	$u_{0963}u_{1006}$
-0.06	$u_{0514}u_{0531}$	-0.0198	$u_{0520}u_{0671}$	0.017	$u_{0919}u_{1370}$
-0.0322	$u_{0835}u_{1225}$	-0.0324	$u_{0278}u_{1079}$	-0.0153	$u_{0487}u_{0732}$
-0.0692	$u_{0288}u_{0660}$	-0.0243	$u_{0584}u_{0663}$	-0.0198	$u_{0367}u_{1150}$
-0.0205	$u_{0286}u_{0783}$	0.0228	$u_{0402}u_{0739}$	-0.0218	$u_{0429}u_{1153}$

where θ_i are the estimated coefficients and $u_k = \mu_a(k)$ are the selected nodes from the inverse mesh to form the monomial terms for the polynomial approximation. The model above presented is the shortest one obtained, other models consider far more terms that for practical purposes are not shown in this work.

6.5.3 Image reconstruction for static optical parameters

Considering *a priori* structural information (anatomical boundaries between tissues), two image reconstruction study cases are explored: i) initial guess close to the expected values using the optical parameters in Table 6.3 and ii) homogeneous absorption coefficient and known scattering coefficient.

Reconstruction with initial guess close to expected values

In this case, the optical parameters in the inverse mesh are close to the values of the target medium, see Table 6.3.

Table 6.3: Initial guess of optical properties for reconstruction algorithm.

Tissue	μ_a [mm^{-1}]	$\mu_s^{'}$ [mm^{-1}]
Skin	0.018	0.50
Muscle	0.02	1.0
Skull	0.004	1.63
Brain	0.01	1.63

The three-dimensional (3D) image reconstruction using NIRFAST and ROM is shown in Fig. 6.6. As can be seen, both approaches reconstructed the inner distribution of the head section.

Figure 6.7 presents a vertical cut from the target medium in Fig. 6.2b and the reconstructions in Fig. 6.6. The increased direction of the$x$-axis indicates the deepness of the tissue and the y-axis the absorption coefficient.

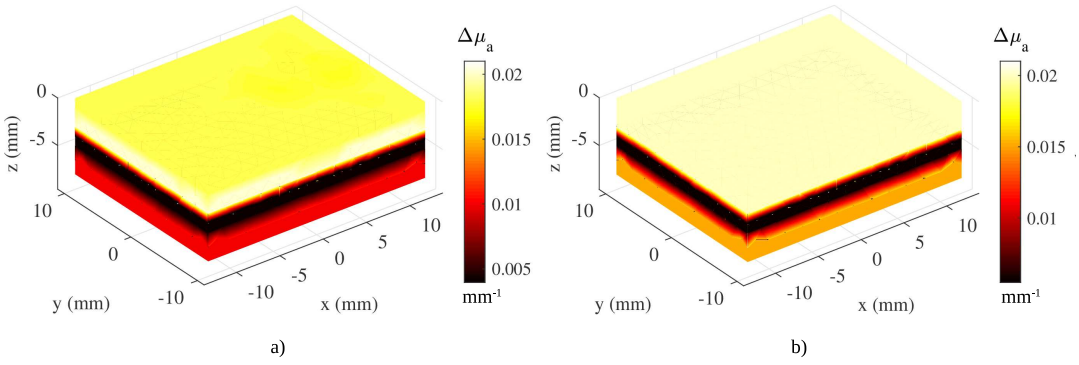

Figure 6.6: Three dimensional image reconstruction of the absorption value with initial guess close to the expected values. a) Using NIRFAST and b) with the ROM approach.

It is observed that NIRFAST performed a better tissue separation between skin and muscle tissues, but it underestimates the absorption distribution along the medium. In contrast, ROM vertical profile shows a better estimation of the final absorption value of brain tissue and a closer estimation of the bone

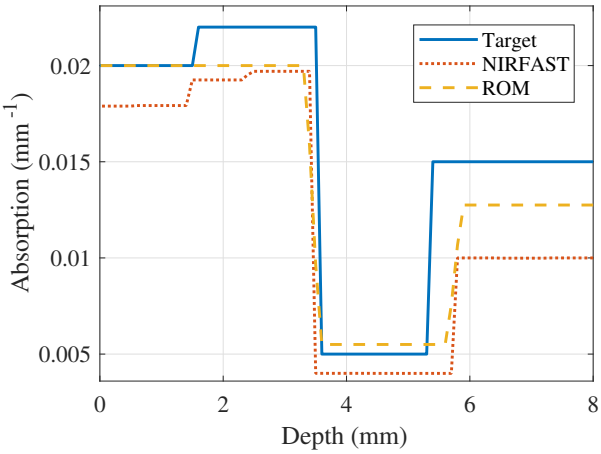

Figure 6.7: Vertical profile comparison between the target medium and the reconstructions from NIRFAST and ROM approaches with heterogeneous initial guess.

absorption value. The only value that it failed to recover the one related to the muscle.

Quantitatively, it is used the Image Correlation Coefficient (ICC) criteria given by Eq 4.14 to compare both approaches. NIRFAST presented an ICC value of $ICC_{NIRFAST} = 0.89$ while ROM obtained an $ICC_{ROM} = 0.91$. The maximum values for the ICC criteria is $ICC = 1$ indicating a perfect match between the evaluated and the target images.

Furthermore, ROM image reconstruction took 15 seconds, outperforming the time required by NIRFAST which took over 50 seconds. The specifications of the computer used in the reconstructions are as follow: intel i7-4700MQ, 8Gb in RAM, hard-drive of 500Gb, graphic card NVIDIA k610m, operative system Ubuntu 14.04 and Matlab 2017a.

Reconstruction with homogeneous absorption distribution

This study case explores if the proposed ROM approach and NIRFAST are able to recover the absorption distribution with a homogeneous initial guess. The

selected value was $\mu_a^0 = 0.013\text{mm}^{-1}$, which is the average of the absorption coefficients shown in Table 6.3, the scattering distribution remained as in the previous example.

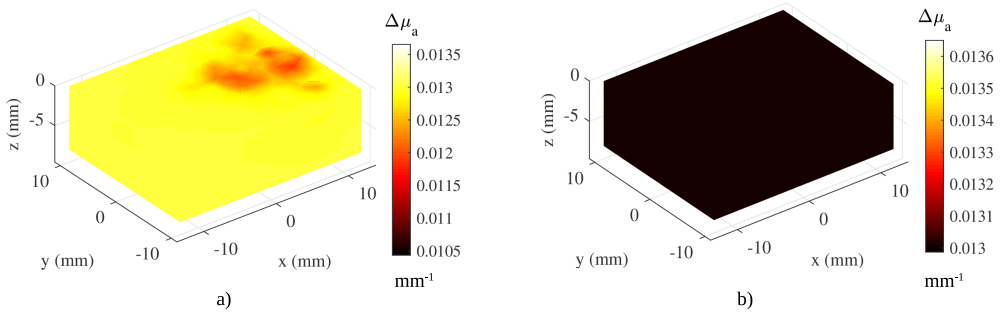

Figure 6.8: Three dimensional image reconstruction of the absorption value with an homogeneous initial for the absorption value. a) Using NIRFAST and b) with the ROM approach.

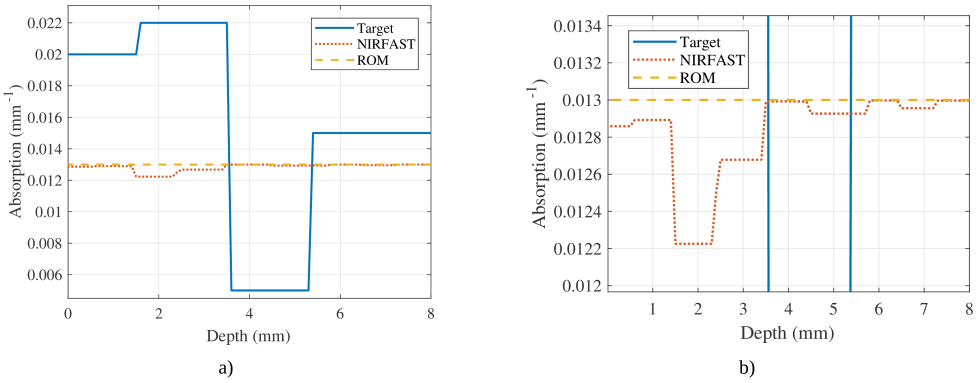

Figure 6.9: Vertical profile comparison between the target medium and the reconstructions from NIRFAST and ROM approaches with homogeneous absorption initial guess.

As can be seen in Fig. 6.8a and Fig. 6.8b, both approaches are unable to reconstruct the absorption distribution correctly. In both cases, a different value from the initial guess proposed was obtained.

The vertical profile comparison displayed in Fig. 6.9a offers an insight of the absorption distribution estimated. In both cases, the estimation is similar to the homogeneous distribution initial guess.

A closer look to the vertical profiles, see Fig. 6.9a, shows that NIRFAST attempts to estimate a different distribution from the initial guess proposed but is unable to resolve the values from the target medium. In contrast, ROM remains constant close to the initial guess. The ICCs obtained were $ICC_{NIRFAST} = -0.566$ and $ICC = -0.275$. The time required were 59 seconds for NIRFAST and 25 seconds for the ROM approach.

6.6 Conclusions

This chapter presented the first results from the Reduced Order Models (ROM) approach within a non-contact framework and a frequency modulated light source, In contrast to the previous work for the monitoring of brain activity presented by Vidal-Rosas *et. al* [243, 252] and the contribution made in this dissertation related to the image reconstruction in Fluorescent Diffuse Optical Tomography that made use of optical fibres to construct the models and to measure the transmitted light within the tissue.

An important contribution to the Spatial Frequency Domain Imaging and also for the Reduced Order Models to be extended to contact-less technologies is the application of the virtual sensor theory used on CCD cameras. The principle of reducing the number of detection positions, in this case pixels of a camera, greatly improve data acquisition and allowed the proper formulation of the Reduced Order Models approach.

Theoretically, an ideal Diffuse Optical Imaging technique would be a system that considers thousands of source-detector measurements and a wide bandwidth of wavelengths, but the engineering implications, such as the complexity of the equipment and time of the reconstructions, limits the practical implementation of such approach. If we consider that CCD cameras have thousands of pixels,

then the only limitation is how to be able to reduce the burden of processing each individual pixel.

By the application of the virtual sensor, this limitation is overcome because it is possible to group pixels to work as a single measurement position, thus exploiting the detection capabilities of a CCD camera with a reduced number of final sensing positions that can be relatively easy to control. This was demonstrated on this chapter by combining the Reduced Order Models with sixteen sensing positions on the CCD camera.

Related to the SFDI reconstructions, it was observed that ROM outperformed NIRFAST in the accuracy of the reconstruction and the reduced time required to obtain the optical parameters. It is important to mention that the accuracy of the image reconstruction strongly depends on the correct selection of the initial optical parameters. More accurate values tend to further improve the quality of the final image and reduce the reconstruction in both NIRFAST and ROM reconstruction algorithms.

Another factor that affects the reconstructions is the quality of the inverse mesh used for the image reconstruction. Fine meshes improve the quality but tend to exponentially increase the time required for the image reconstruction when considering a image reconstruction scheme that requires the whole mesh.

As has been mentioned on the previous chapters, the ROM approach has the advantage that it does not work directly with the full FEM mesh during the inverse process. It maps the measurements from the reduced order models, generated by the system identification process to obtain an estimation of the absorption parameters that interacted with the light within the medium and then creates a 3D map of that distribution.

Chapter 7

Conclusions

The work presented in this thesis addresses two specific problems that are hindering the application of diffuse optical imaging in clinical settings, specifically for Fluorescent Diffuse Optical Tomography and Spatial Frequency Domaing Imaging: processing of high-density data and real-time image reconstruction of the optical properties from biological tissue.

In summary, the imaging problem is cast into a non-linear mapping using a data base model, which accelerates the inversion process by avoiding solving the diffusion equation directly. Instead, the proposed method employs a highly optimised reduced-order model (ROM) of the diffusion equation to describe light propagation.

The model used in this work is based on polynomial functions; which are a convenient choice since they are easy to store and manipulate; but they are by no means the only choice because other functions such as neural networks, splines or wavelets can also be implemented. Although a previous work of Vidal Rosas [252] used Radial-basis functions to formulate ROM and showed that it was required further analysis in order to select the correct parameters for the functions and the results were similar to those obtained by polynomial models. Therefore, it was concluded that polynomial models were a better option for ROM formulation

and implementation.

Diffuse optical imaging has received a significant attention in recent years because of the benefits it can bring in comparison with traditional imaging modalities such as MRI, CT or PET. Those benefits include portability, non-invasiveness, compactness, speed, continuous monitoring and safety [21, 298].

The technology is moving swiftly and recent progress includes ultra high-density probes [151, 299], real-time imaging [256] and mobile/wearable devices [300, 301]. The introduction of high-density (HD) data has shown to be decisive for the success of DOT in brain imaging; which has demonstrated to approach the performance of fMRI in accuracy and resolution at the cortex level [302]. Wearability can also bring important benefits, as allowing unrestricted imaging of brain function in naturalistic environments.

However, the benefits are no problem-free, for example, wearability intensifies movements artefacts (i.e. abrupt head rotations), systemic interference (increased heart rate while walking in comparison to standing still) and also cofounding effects (attention to multiple tasks simultaneously) [303, 304, 300].

On the other hand, high-density data requires sophisticated solution algorithms and computational power in the form of GPUs for example [305]. In addition, real-time imaging is not a trivial problem, since it requires a trade-off between reconstruction speed and accuracy [256, 243].

This thesis introduces a new methodology for the reconstruction of optical parameters in Diffuse Optical Imaging, in particular to Fluorescence Diffuse Optical Tomography (FDOT) and Spatial Frequency Domain Imaging (SFDI). The proposed approach accelerates the reconstruction process by a factor of

approximately four in 2D FDOT and an improvement of a fifth of the time required in 3D FDOT, while for SFDI the speed improved by a factor of two.

An important contribution made to Spatial Frequency Domain Imaging was the use of the virtual sensor on CCD cameras. Previous to this work, there is no work related of limiting the number of available detection points or pixels to detect a spatially modulated light source. The implications of this contribution is related to the possibility to have more control over the data collected over the analysed area.

Furthermore, the use of the virtual sensor was the key point that allowed the formulation of ROM using CCD cameras, which also is a work not reported before. Is important to note that with the use of the virtual sensor and ROM it is possible to perform contact-less experiments using CCD cameras instead of only using optical fibres.

Moreover, the reconstruction speed has been improved without compromising the quality of the images obtained. The results presented in this work demonstrated the feasibility of the approach while running on a modest and cheap PC. Using compiled C/C++ subroutines can further reduce these values, potentially reaching real-time imaging.

In addition, considering the low computational cost of the proposed method means that FDOT and SFD imaging can be solved in a personal computer with no addition of a GPU or an expensive CPU. This opens new possibilities to further miniaturise the devices, to increase portability and to achieve real-time imaging using .

Furthermore, other diffuse imaging modalities can also benefit from the

introduction of the methods presented in this thesis. For example, speckle contrast optical tomography (SCOT) is a new modality that employs point sources and a detector array (CCD) to quantify the spatial or temporal speckle contrast [306, 307]. This technology produces ultra-large data density (>50000 source-detector pairs) that prohibits the use of nonlinear solvers such as NIRFAST. By using reduced-order models, the restrictions in memory and speed can be minimized. Thus, ROM in combination with the proposed virtual sensor approach could benefit the characterization high density optical imaging approaches

Finally, the method that we advocate can also be used in conjunction with the full model, i.e. reduced-order models can be used in an initial run; then the solution produced can be used as an initial guess, which can be further refined by the standard approach, that uses the full diffusion equation model.

Future work could be the implementation of the ROM into portable devices, such as tablets or smart phones with enough computational power to run 3D graphics. Also, explore other DOI modalities such as SCOT or exploit the computational capabilities of ROM by training models using the Radiative Transfer Equation as the input-output data source instead of the Diffusion Equation further expanding the proposed approach to Fluorescence Molecular Tomography or Optical Coherence Tomography which are out of the scope of the diffusion approximation.

Bibliography

[1] Paul Suetens. *Fundamentals of medical imaging*. Cambridge University Press, illustrate edition, 2009.

[2] A. Dhawan. *Medical image analysis*. Wiley-IEEE Press, 2011.

[3] C Zhu and Q Liu. Review of Monte Carlo modeling of light transport in tissues. *Journal of Biomedical Optics*, 18(5), 2013.

[4] D A Boas, J P Culver, J J Stott, and A K Dunn. Three dimensional Monte Carlo code for photon migration through complex heterogeneous media including the adult human head. *Optics Express*, 10(3):159–170, 2002.

[5] A D Klose and A H Hielscher. Optical tomography with the equation of radiative transfer. *International Journal of Numerical Methods for Heat and Fluid Flow*, 18(3-4):443–464, 2008.

[6] F Martelli, D Contini, A Taddeucci, and G Zaccanti. Photon migration through a turbid slab described by a model based on diffusion approximation. II. Comparison with Monte Carlo results. *Applied Optics*, 36(19):4600–4612, 1997.

[7] D Contini, F Martelli, and G Zaccanti. Photon migration through a turbid slab described by a model based on diffusion approximation. I. Theory. *Applied Optics*, 36(19):4587–4599, 1997.

[8] T Tarvainen, M Vauhkonen, V Kolehmainen, S R Arridge, and J P Kaipio. Coupled radiative transfer equation and diffusion approximation model for photon migration in turbid medium with low-scattering and non-scattering regions. *Physics in Medicine and Biology*, 50(20):4913–4930, 2005.

[9] K Ren, G S Abdoulaev, G Bal, and A H Hielscher. Algorithm for solving the equation of radiative transfer in the frequency domain. *Optics Letters*, 29(6):578–580, 2004.

[10] Andreas H Hielscher. Optical tomographic imaging of small animals. *Current opinion in biothecnology*, 16(1):79–88, 2005.

[11] A P Gibson, J C Hebden, and S R Arridge. Recent advances in diffuse optical imaging. *Physics in Medicine and Biology*, 50(4):R1–R43, 2005.

[12] S R Arridge. Optical tomography in medical imaging. *Inverse Problems*, 15(2):R41–R49, 1999.

[13] Regine Choe. *Diffuse optical tomography and spectroscopy of breast cancer and fetal brain*. PhD thesis, Pennsylvania, 2005.

[14] Vikas Chaudhary. *Advances in Brain Imaging*. 2012.

[15] A E Cerussi, A J Berger, F Bevilacqua, N Shah, D Jakubowski, J Butler, R F Holcombe, and B J Tromberg. Sources of absorption and scattering contrast for near-infrared optical mammography, 2001.

[16] A Maki, Y Yamashita, Y Ito, and H Koizumi. Spatial and Temporal Analysis of Human Motor Activity Using Noninvasive NIR Topography, 1995.

[17] B W Pogue and M S Patterson. Frequency-domain optical absorption spectroscopy of finite tissue volumes using diffusion theory. *Physics in Medicine and Biology*, 39(7):1157–1180, 1994.

[18] S Wray, M Cope, D T Delpy, J S Wyatt, and E O R Reynolds. Characterization of the near infrared absorption spectra of cytochrome aa3 and haemoglobin for the non-invasive monitoring of cerebral oxygenation. *BBA - Bioenergetics*, 933(1):184–192, 1988.

[19] Eva M Sevick-Muraca and Christina L Burch. Origin of phosphorescence signals reemitted from tissues. *Optics Letters*, 19(23):1928–1930, 1994.

[20] J Chang, H L Graber, and R L Barbour. Imaging of fluorescence in highly scattering media. *IEEE Transactions on Biomedical Engineering*, 44(9):810–822, 1997.

[21] A Gibson and H Dehghani. Diffuse optical imaging. *Philosophical Transactions of the Royal Society A: Mathematical, Physical and Engineering Sciences*, 367(1900):3055–3072, 2009.

[22] H Dehghani, M E Eames, P K Yalavarthy, S C Davis, S Srinivasan, C M Carpenter, B W Pogue, and K D Paulsen. Near infrared optical tomography using NIRFAST: Algorithm for numerical model and image reconstruction. *Communications in Numerical Methods in Engineering*, 25(6):711–732, 2008.

[23] M Schweiger and S Arridge. The Toast++ software suite for forward and inverse modeling in optical tomography. *Journal of Biomedical Optics*, 19(4), 2014.

[24] V Ntziachristos, A G Yodh, M Schnall, and B Chance. Concurrent MRI and diffuse optical tomography of breast after indocyanine green enhancement. In *Proceedings of the National Academy of Sciences of the United States of America*, volume 97, pages 2767–2772, Department of Bioengineering, University of Pennsylvania, Philadelphia, PA 19104-6089, United States, 2000.

[25] Samir Kumar Biswas, Rajan Kanhirodan, Ram Mohan Vasu, and Debasish Roy. Practical fully three-dimensional reconstruction algorithms for diffuse optical tomography. *Journal of the Optical Society of America A*, 29(6):1017–1026, 2012.

[26] S L Jacques and B W Pogue. Tutorial on diffuse light transport. *Journal of Biomedical Optics*, 13(4), 2008.

[27] L Wang, S L Jacques, and L Zheng. MCML-Monte Carlo modeling of light transport in multi-layered tissues. *Computer Methods and Programs in Biomedicine*, 47(2):131–146, 1995.

[28] A D Klose. The forward and inverse problem in tissue optics based on the radiative transfer equation: A brief review. *Journal of Quantitative Spectroscopy and Radiative Transfer*, 111(11):1852–1853, 2010.

[29] S R Arridge and J C Schotland. Optical tomography: Forward and inverse problems. *Inverse Problems*, 25(12), 2009.

[30] D A Boas, K Chen, D Grebert, and M A Franceschini. Improving the diffuse optical imaging spatial resolution of the cerebral hemodynamic response to brain activation in humans. *Optics Letters*, 29(13):1506–1508, 2004.

[31] B W Pogue, S C Davis, X Song, B A Brooksby, H Dehghani, and K D Paulsen. Image analysis methods for diffuse optical tomography. *Journal of Biomedical Optics*, 11(3), 2006.

[32] Y Bérubé-Lauzière, M Crotti, S Boucher, S Ettehadi, J Pichette, and I Rech. Prospects on Time-Domain Diffuse Optical Tomography Based on Time-Correlated Single Photon Counting for Small Animal Imaging, 2016.

[33] S K Biswas, R Kanhirodan, and R M Vasu. Three-dimensional diffuse optical tomography: System implementation and validation of reconstruction algorithms. In *IEEE Nuclear Science Symposium Conference Record*, pages 2811–2813, Department of Physics, Indian Institute of Science, Bangalore, 560012, India, 2010.

[34] R Weissleder and V Ntziachristos. Shedding light onto live molecular targets. *Nature Medicine*, 9(1):123–128, 2003.

[35] E M C Hillman. Optical brain imaging in vivo: Techniques and applications from animal to man. *Journal of Biomedical Optics*, 12(5), 2007.

[36] Xue Wu, Adam T Eggebrecht, Silvina L Ferradal, Joseph P Culver, and Hamid Dehghani. Quantitative evaluation of atlas-based high-density diffuse optical tomography for imaging of the human visual cortex. *Biomedical Optics Express*, 5(11):3882–3900, nov 2014.

[37] T F Massoud and S S Gambhir. Molecular imaging in living subjects: Seeing fundamental biological processes in a new light. *Genes and Development*, 17(5):545–580, 2003.

[38] M T Albelda, E García-España, and J C Frías. Imaging atoms in medicine. *BioMetals*, 22(3):393–399, 2009.

[39] X Liu, B Zhang, J Luo, and J Bai. 4-D reconstruction for dynamic fluorescence diffuse optical tomography. *IEEE Transactions on Medical Imaging*, 31(11):2120–2132, 2012.

[40] V Ntziachristos. Fluorescence molecular imaging, 2006.

[41] C Darne, Y Lu, and E M Sevick-Muraca. Small animal fluorescence and bioluminescence tomography: A review of approaches, algorithms and technology update. *Physics in Medicine and Biology*, 59(1):R1–R64, 2014.

[42] A Y Bluestone, M Stewart, J Lasker, G S Abdoulaev, and A H Hielscher. Three-dimensional optical tomographic brain imaging in small animals, part 1: Hypercapnia. *Journal of Biomedical Optics*, 9(5):1046–1062, 2004.

[43] A B Milstein, S Oh, K J Webb, C A Bouman, Q Zhang, D A Boas, and R P Millane. Fluorescence optical diffusion tomography. *Applied Optics*, 42(16):3081–3094, 2003.

[44] C Habermehl, C Schmitz, and J Steinbrink. Contrast-enhanced diffuse optical tomography of brain perfusion in humans using ICG. In *Progress in Biomedical Optics and Imaging - Proceedings of SPIE*, volume 8207, 2012.

[45] C Habermehl, C H Schmitz, and J Steinbrink. Contrast enhanced high-resolution diffuse optical tomography of the human brain using ICG. *Optics Express*, 19(19):18636–18644, 2011.

[46] V Ntziachristos and B Chance. Probing physiology and molecular function using optical imaging: Applications to breast cancer. *Breast Cancer Research*, 3(1):41–46, 2001.

[47] A Corlu, R Choe, T Durduran, M A Rosen, M Schweiger, S R Arridge, M D Schnall, and A G Yodh. Three-dimensional in vivo fluorescence diffuse optical tomography of breast cancer in humans. *Optics Express*, 15(11):6696–6716, 2007.

[48] S J Erickson, S L Martinez, J DeCerce, A Romero, L Caldera, and A Godavarty. Three-dimensional fluorescence tomography of human breast tissues in vivo using a hand-held optical imager. *Physics in medicine and biology*, 58(5):1563–1579, 2013.

[49] D J Cuccia, F Bevilacqua, A J Durkin, and B J Tromberg. Modulated imaging: Quantitative analysis and tomography of turbid media in the spatial-frequency domain. *Optics Letters*, 30(11):1354–1356, 2005.

[50] David J Cuccia, Frederic Bevilacqua, Anthony J Durkin, and Bruce J Tromberg. Quantitative Recovery of Tissue Optical Properties in the Spatial Frequency Domain Using Modulated Imaging. In *Frontiers in Optics*, pages 2500–2500, 2005.

[51] John Quan Nguyen, Christian Crouzet, Tuan Mai, Kathleen Riola, Daniel Uchitel, Lih-Huei Liaw, Nicole Bernal, Adrien Ponticorvo, Bernard Choi, and Anthony J Durkin. Spatial frequency domain imaging of burn wounds in a preclinical model of graded burn severity. *Journal of Biomedical Optics*, 18(6):66010, 2013.

[52] Amaan Mazhar, Ata Sharif, David Cuccia, J Stuart Nelson, Kristen Kelly, and Anthony Durkin. *Spatial Frequency Domain Imaging of Port Wine Stain Biochemical Composition in Response to Laser Therapy: A Pilot Study*, volume 44. oct 2012.

[53] M D Reisman, Z E Markow, A Q Bauer, and J P Culver. Structured illumination diffuse optical tomography for noninvasive functional neuroimaging in mice, 2017.

[54] J A Guggenheim, H R A Basevi, J Frampton, I B Styles, and H Dehghani. Multi-modal molecular diffuse optical tomography system for small animal imaging. *Measurement Science and Technology*, 24(10), 2013.

[55] A Joshi, W Bangerth, A B Thompson, and E M Sevick-Muraca. Adaptive finite element methods for fluorescence enhanced frequency domain optical tomography: Forward imaging problem. In *2004 2nd IEEE International Symposium on Biomedical Imaging: Macro to Nano*, volume 2, pages 1103–1106, 2004.

[56] A Joshi, W Bangerth, and E M Sevick-Muraca. Adaptive finite element based tomography for fluorescence optical imaging in tissue. *Optics Express*, 12(22):5402–5417, 2004.

[57] M Guven, B Yazici, K Kwon, E Giladi, and X Intes. Effect of discretization error and adaptive mesh generation in diffuse optical absorption imaging: I. *Inverse Problems*, 23(3):1115–1133, 2007.

[58] Jong Chul Ye, C A Bouman, R P Millane, and K J Webb. Nonlinear multigrid optimization for Bayesian diffusion tomography. *Proc ICIP*, 2(5):653—-657vol.2, 1999.

[59] M Guven, B Yazici, X Intes, and B Chance. An adaptive multigrid algorithm for region of interest diffuse optical tomography. In *IEEE International Conference on Image Processing*, volume 2, pages 823–826, Drexel University, Electrical and Computer Engineering, Philadelphia, PA, United States, 2003.

[60] Y Zhai and S A Cummer. Fast tomographic reconstruction strategy for diffuse optical tomography. *Optics Express*, 17(7):5285–5297, 2009.

[61] J.-C. Baritaux, S C Sekhar, and M Unser. A spline-based forward model for optical diffuse tomography. In *2008 5th IEEE International Symposium on Biomedical Imaging: From Nano to Macro, Proceedings, ISBI*, pages 384–387, Biomedical Imaging Group, EPFL, CH-1015 Lausanne, Switzerland, 2008.

[62] A Frassati, A Da Silva, J.-M. Dinten, and D Georges. Model reduction by multiresolution method applied to Fluorescence Diffuse Optical Tomography. In *Annual International Conference of the IEEE Engineering in Medicine and Biology - Proceedings*, pages 767–770, IEEE, 2007.

[63] N Ducros, A Da Silva, J.-M. Dinten, C S Seelamantula, M Unser, and F Peyrin. A time-domain wavelet-based approach for fluorescence diffuse optical tomography. *Medical Physics*, 37(6):2890–2900, 2010.

[64] E E Vidal-Rosas, S A Billings, Y Zheng, J E W Mayhew, D Johnston, A Kennerly, and D Coca. Real-time Diffuse Optical Tomography using reduced-order light propagation models. In *Proceedings of the 8th IASTED International Conference on Biomedical Engineering, Biomed 2011*, pages 378–385, Department of Automatic Control and Systems Engineering, University of Sheffield, Mappin Street, Sheffield, S1 3JD, United Kingdom, 2011.

[65] E E Vidal-Rosas. *Advanced tomographic reconstruction methods for diffuse optical imaging of cerebral haemodynamic response*. PhD thesis, University of Sheffield, 2011.

[66] M. Cutler. Transillumination as an aid in the diagnosis of breast lesions. *Surg. Gynecol. Obstet*, 48:721–728, 1929.

[67] D A Boas, D H Brooks, E L Miller, C A DiMarzio, M Kilmer, R J Gaudette, and Q Zhang. Imaging the body with diffuse optical tomography. *IEEE Signal Processing Magazine*, 18(6):57–75, 2001.

[68] C Gros, Y Quenneville, and Y Hummel. Breast diaphanology . *Journal de radiologie, d"electrologie, et de medecine nucleaire*, 53(4):297–306, 1972.

[69] Frans F. Jobsis. Noninvasive, infrared monitoring of cerebral and myocardial oxygen sufficiency and circulatory parameters. *Science*, 198(4323):1264–1267, 1977.

[70] Y Yamashita, A Maki, and H Koizumi. Measurement system for noninvasive dynamic optical topography, 1999.

[71] D Grosenick, H Wabnitz, H H Rinneberg, K T Moesta, and P M Schlag. Development of a time-domain optical mammograph and first in vivo applications. *Applied Optics*, 38(13):2927–2943, 1999.

[72] J C Hebden, S R Arridge, and D T Delpy. Optical imaging in medicine: I. Experimental techniques. *Physics in Medicine and Biology*, 42(5):825–840, 1997.

[73] S B Colak, M B Van Der Mark, G W 'T Hooft, J H Hoogenraad, E S Van Der Linden, and F A Kuijpers. Clinical optical tomography and NIR spectroscopy for breast cancer detection. *IEEE Journal on Selected Topics in Quantum Electronics*, 5(4):1143–1158, 1999.

[74] V Ntziachristos, J Ripoll, L V Wang, and R Weissleder. Looking and listening to light: The evolution of whole-body photonic imaging. *Nature Biotechnology*, 23(3):313–320, 2005.

[75] H Egger, M Freiberger, and M Schlottbom. On forward and inverse models in fluorescence diffuse optical tomography. *Inverse Problems and Imaging*, 4(3):411–427, 2010.

[76] D A Boas, C E Elwell, M Ferrari, and G Taga. Twenty years of functional near-infrared spectroscopy: Introduction for the special issue. *NeuroImage*, 85:1–5, 2014.

[77] R Roy and E M Sevick-Muraca. Truncated Newton's optimization scheme for absorption and fluorescence optical tomography: Part I theory and formulation. *Optics Express*, 4(10):353–371, 1999.

[78] R Roy and E M Sevick-Muraca. Truncated Newton's optimization scheme for absorption and fluorescence optical tomography: Part II reconstruction from synthetic measurements. *Optics Express*, 4(10):372–382, 1999.

[79] F Scholkmann, S Kleiser, A J Metz, R Zimmermann, J Mata Pavia, U Wolf, and M Wolf. A review on continuous wave functional near-infrared spectroscopy and imaging instrumentation and methodology, 2014.

[80] Xiaofeng Zhang. Instrumentation in Diffuse Optical Imaging. *Photonics*, 1(1):9–32, mar 2014.

[81] C H Schmitz, M Löcker, J M Lasker, A H Hielscher, and R L Barbour. Instrumentation for fast functional optical tomography. *Review of Scientific Instruments*, 73(2 I):429, 2002.

[82] A. Hielscher, G. Abdoulaev, A. Klose, J. Lasker, M. Stewart, and A. Bluestone. Near-Infrared diffuse optical tomography. *Disease Markers Functional Imaging of Early Markers of Disease*, 18:313–337, 2002.

[83] E E Graves, J Ripoll, R Weissleder, and V Ntziachristos. A submillimeter resolution fluorescence molecular imaging system for small animal imaging. *Medical Physics*, 30(5):901–911, 2003.

[84] D K Joseph, T J Huppert, M A Franceschini, and D A Boas. Diffuse optical tomography system to image brain activation with improved spatial resolution and validation with functional magnetic resonance imaging. *Applied Optics*, 45(31):8142–8151, 2006.

[85] K L Perdue, Q Fang, and S G Diamond. Quantitative assessment of diffuse optical tomography sensitivity to the cerebral cortex using a whole-head probe. *Physics in Medicine and Biology*, 57(10):2857–2872, 2012.

[86] V Ntziachristos and R Weissleder. Experimental three-dimensional fluorescence reconstruction of diffuse media by use of a normalized Born approximation. *Optics Letters*, 26(12):893–895, 2001.

[87] S R Arridge and W R B Lionheart. Nonuniqueness in diffusion-based optical tomography. *Optics Letters*, 23(11):882–884, 1998.

[88] Y Pei, H L Graber, and R L Barbour. Normalized-constraint algorithm for minimizing inter-parameter crosstalk in DC optical tomography. *Optics Express*, 9(2):97–109, 2001.

[89] Y Pei, H L Graber, and R L Barbour. Influence of systematic errors in reference states on image quality and on stability of derived information for dc optical imaging. *Applied Optics*, 40(31):5755–5769, 2001.

[90] A Farina, S Tagliabue, L D Sieno, E Martinenghi, T Durduran, S Arridge, F Martelli, A Torricelli, A Pifferi, and A D Mora. Time-domain functional diffuse optical tomography system based on fiber-free silicon photomultipliers, 2017.

[91] A Puszka, L Di Sieno, A D Mora, A Pifferi, D Contini, A Planat-Chrétien, A Koenig, G Boso, A Tosi, L Hervé, and J.-M. Dinten. Spatial resolution in depth for time-resolved diffuse optical tomography using short sourcedetector separations, 2015.

[92] I Nissilä, J C Hebden, D Jennions, J Hieno, M Schweiger, K Kotilahti, T Noponen, A Gibson, S Järvenpää, L Lipiäinen, and T Katila. Comparison between a time-domain and frequency-domain system for optimal tomography, 2006.

[93] Vivek Venugopal, Jin Chen, and Xavier Intes. Development of an optical imaging platform for functional imaging of small animals using wide- field excitation. *Biomedical Optics Express*, 1(1):143–156, 2010.

[94] F Leblond, S C Davis, P A Valdés, and B W Pogue. Pre-clinical whole-body fluorescence imaging: Review of instruments, methods and applications. *Journal of Photochemistry and Photobiology B: Biology*, 98(1):77–94, 2010.

[95] L. Hundley, T. Coburn, E. Garwin, and L. Stryer. Nanosecond fluorimeter. *Review of Scientific Instruments*, 38:488–492, 1967.

[96] D.T. Delpy, M. Cope, P. Vanderzee, Simon Arridge, S. Wray, and J. Wyatt. Estimation of optical pathlength through tissue from direct time of flight measurement. *Physics in Medicine and Biology*, 33:1433–1442, 1988.

[97] B. Chance, Shoko Nioka, J. Kent, K. McCully, M. Fountain, R. Greenfeld, and G. Holtom. Time-resolved spectroscopy of hemoglobin and myoglobin in resting and ischemic muscle. *Analytical Biochemistry*, 174:698–707, 1988.

[98] M S Patterson, B Chance, and B C Wilson. Time resolved reflectance and transmittance for the non-invasive measurement of tissue optical properties. *Appl. Opt.*, 28(12):2331–2336, 1989.

[99] Yiwen Ma, Shaorun Gong, Feng Gao, Fang Yang, Huijuan Zhao, and Jingying Jiang. Improvement of performances in time-domain breast DOT by the aid of image segmentation. volume 6850, pages 68500P–68500P–9, 2008.

[100] V Ntziachristos, X H Ma, and B Chance. Time-correlated single photon counting imager for simultaneous magnetic resonance and near-infrared mammography. *Review of Scientific Instruments*, 69(12):4221–4233, 1998.

[101] David K. Jennions. *Time-Resolved Optical Tomography Instrumentation for Fast 3D Functional Imaging*. PhD thesis, University College London, 2008.

[102] V Ntziachristos, X H Ma, A G Yodh, and B Chance. Multichannel photon counting instrument for spatially resolved near infrared spectroscopy. *Rev. Sci. Instrum.*, 70(1):193–201, 1999.

[103] E M C Hillman, J C Hebden, M Schweiger, H Dehghani, F E W Schmidt, D T Delpy, and S R Arridge. Time resolved optical tomography of the human forearm. *Physics in Medicine and Biology*, 46(4):1117–1130, 2001.

[104] J.-P. L'Huillier. Time-domain fluorescence mammography using early-time reflected signals : Finite element approach. In *Proceedings of SPIE - The International Society for Optical Engineering*, volume 6994, 2008.

[105] Vasilis Ntziachristos, A G Yodh, Mitchel Schnall, and Britton Chance. Comparison between intrinsic and extrinsic contrast for malignancy detection using NIR mammography. In *Proceedings of SPIE - The International Society for Optical Engineering*, volume 3597, pages 565–570, 1999.

[106] R M Danen, Yong Wang, X D Li, C Dean Kurth, W S Thayer, and A G Yodh. Near-infrared imaging of brains. In *Conference on Lasers and Electro-Optics Europe - Technical Digest*, pages 86–87, 1998.

[107] A Pifferi, D Contini, A D Mora, A Farina, L Spinelli, and A Torricelli. New frontiers in time-domain diffuse optics, a review, 2016.

[108] N Ducros, A Da Silva, J.-M. Dinten, C S Seelamantula, M Unser, and F Peyrin. Time resolved fluorescence diffuse optical tomography using multi-resolution exponential B-splines. In *Proceedings - 2009 IEEE International Symposium on Biomedical Imaging: From Nano to Macro, ISBI 2009*, pages 157–160, CEA, LETI, MINATEC, 17 rue des Martyrs, F-38054 Grenoble, France, 2009.

[109] Elizabeth M. C. Hillman. *Experimental and theoretical investigations of near infrared tomographic imaging methods and clinical applications*. PhD thesis, University of London, 2002.

[110] D A Boas. Diffuse photon probes of structural and dynamical properties of turbid media: theory and biomedical applications. *Optics express*, 8(5):263–270, 1996.

[111] R. D. Spencer and G. Weber. Measurements of subnanosecond fluorescence lifetimes with a cross-correlation phase fluorometer. *Annals of the New York Academy of Sciences*, 158:361–376, 1969.

[112] B. A. Feddersen, D. W. Piston, and E. Gratton. Digital parallel acquisition in frequency-domain fluorimetry. *Review of Scientific Instruments*, 60:2929–2936, 1989.

[113] Sergio Fantini, Maria Angela Franceschini, and Enrico Gratton. Semi-infinite-geometry boundary-problem for light migration in highly scattering media - a frequency domain study in the diffusion-approximation. *Journal of the Optical Society of America B-Optical Physics*, 11:2128–2138, 1994.

[114] M. A. Oleary, David A. Boas, Britton Chance, and Arjun G Yodh. Refraction of diffuse photon density waves. *Physical Review Letters*, 69:2658–2661, 1992.

[115] S. J. Madsen, E. R. Anderson, Richard C. Haskell, and Bruce J. Tromberg. Portable, high-bandwidth frequency-domain photon migration instrument for tissue spectroscopy. *Optics Letters*, 19:1934–1936, 1994.

[116] Sergio Fantini, Maria Angela Franceschini, B. Fishkin Joshua, Beniamino Barbieri, and Enrico Gratton. Quantitative determination of the absorption spectra of chromophores in strongly scattering media: A light-emitting-diode based technique. *Applied Optics*, 33(22):5204–5214, 1994.

[117] Q Q Zhang, X J Wu, C Wang, S W Zhu, Y L Wang, B Z Gao, and X.-C. Yuan. Scattering coefficients of mice organs categorized pathologically by spectral domain optical coherence tomography. *BioMed Research International*, 2014, 2014.

[118] D Grosenick, H Rinneberg, R Cubeddu, and P Taroni. Review of optical breast imaging and spectroscopy, 2016.

[119] Sergio Fantini. Optical Mammography. In Mohammed Arif Hayat, editor, *Cancer Imaging: Lung and breast carcinomas*, chapter Chapter 16, pages 449–458. Academic Press, vol. 1 edition, 2007.

[120] S Fantini, S. A. Walker, M A. Franceschini, M. Kaschke, P.M. Schlag, and K.T. Moesta. Assessnent of the size, position and optical properties of breast tumours in vivo by non-invasive optical methods. *Appl. Opt.*, 37:1982–1989, 2005.

[121] JeeHyun Choi, Martin Wolf, Vladislav Toronov, Ursula Wolf, Chiara Polzonetti, Dennis Hueber, Larisa P Safonova, Rajarsi Gupta, Antonios Michalos, William Mantulin, and Enrico Gratton. Noninvasive determination of the optical properties of adult brain: near-infrared spectroscopy approach. *Journal of Biomedical Optics*, 9(1):221–229, 2004.

[122] K Ren, B Moa-Anderson, G Bal, X Gu, and A H Hielscher. Frequency domain tomography in small animals with the equation of radiative transfer. In *Progress in Biomedical Optics and Imaging - Proceedings of SPIE*, volume 5693, pages 111–120, Dept. of Appl. Physics and Appl. Mathematics, Columbia University, New York, NY 10027, United States, 2005.

[123] David J Cuccia, Frederic Bevilacqua, Anthony J Durkin, Sean Merritt, Bruce J Tromberg, Gultekin Gulsen, Hon Yu, Jun Wang, and Orhan Nalcioglu. In vivo quantification of optical contrast agent dynamics in rat tumors by use of diffuse optical spectroscopy with magnetic resonance imaging coregistration. *Applied optics*, 42(16):2940–50, 2003.

[124] E M Sevick-Muraca, J S Reynolds, T L Troy, G Lopez, and D Y Paithankar. Fluorescence lifetime spectroscopic imaging with measurements of photon migration, 1998.

[125] Q Zhu, T Durduran, V Ntziachristos, M Holboke, and A G Yodh. Imager that combines near-infrared diffusive light and ultrasound. *Optics Letters*, 24(15):1050–1052, 1999.

[126] A Laidevant, L Hervé, M Debourdeau, J Boutet, N Grenier, and J.-M. Dinten. Fluorescence time-resolved imaging system embedded in an ultrasound prostate probe. *Biomedical Optics Express*, 2(1):194–206, 2011.

[127] B Li, F Maafi, R Berti, P Pouliot, E Rhéaume, J C Tardif, and F Lesage. Hybrid FMT-MRI applied to in vivo atherosclerosis imaging. *Biomedical Optics Express*, 5(5):1664–1676, 2014.

[128] S C Davis, B W Pogue, R Springett, C Leussler, P Mazurkewitz, S B Tuttle, S L Gibbs-Strauss, S S Jiang, H Dehghani, and K D Paulsen. Magnetic

resonance-coupled fluorescence tomography scanner for molecular imaging of tissue. *Review of Scientific Instruments*, 79(6), 2008.

[129] S C Davis, S L Gibbs-Strauss, H Dehghani, B W Pogue, and K D Paulsen. MRI-coupled fluorescence tomography of murine glioma metabolic activity. In *Biomedical Optics, BIOMED 2008*, Thayer School of Engineering, Dartmouth College, Hanover NH 03755, United States, 2008.

[130] A Ale, V Ermolayev, E Herzog, C Cohrs, M H De Angelis, and V Ntziachristos. FMT-XCT: In vivo animal studies with hybrid fluorescence molecular tomography-X-ray computed tomography. *Nature Methods*, 9(6):615–620, 2012.

[131] J P Culver, R Choe, M J Holboke, L Zubkov, T Durduran, A Slemp, V Ntziachristos, B Chance, and A G Yodh. Three-dimensional diffuse optical tomography in the parallel plane transmission geometry: Evaluation of a hybrid frequency domain/continuous wave clinical system for breast imaging. *Medical Physics*, 30(2):235–247, 2003.

[132] Vasilis Ntziachristos, A G Yodh, and Britton Chance. Optical Tomography using multi-frequency intensity information. In *Annual International Conference of the IEEE Engineering in Medicine and Biology - Proceedings*, volume 2, page 1100, 1999.

[133] S. J. Madsen, P. Wyss, Lars O. Svaasand, Richard C. Haskell, Y. Tadir, and Bruce J. Tromberg. Determination of the optical-properties of the human uterus using frequency-domain photon migration and steady-state techniques. *Physics in Medicine and Biology*, 39:1191–1202, 1994.

[134] S R Arridge. Photon-measurement density functions. Part I: Analytical forms. *Applied Optics*, 34(31):7395–7409, 1995.

[135] N Shah, A Cerussi, C Eker, J Espinoza, J Butler, J Fishkin, R Hornung, and B Tromberg. Noninvasive functional optical spectroscopy of human breast tissue, 2001.

[136] R J Cooper and D A Boas. Functional Near-Infrared Spectroscopy, 2015.

[137] H Ayaz, B Onaral, K Izzetoglu, P A Shewokis, R Mckendrick, and R Parasuraman. Continuous monitoring of brain dynamics with functional near infrared spectroscopy as a tool for neuroergonomic research: Empirical examples and a technological development, 2013.

[138] A Pellicer and M D C Bravo. Near-infrared spectroscopy: A methodology-focused review. *Seminars in Fetal and Neonatal Medicine*, 16(1):42–49, 2011.

[139] Alexey N. Bashkatov, Elina A. Genina, and Valery V. Tuchin. Optical Properties of Skin, Subcutaneous, and Muscle Tissues: a Review. *Journal of Innovative Optical Health Sciences*, 04(01):9–38, 2011.

[140] G Taga, K Asakawa, A Maki, Y Konishi, and H Koizumi. Brain imaging in awake infants by near-infrared optical topography, 2003.

[141] Tingting Cai, Hullin Zhu, Jie Xu, Shijing Wu, Xinge Li, and Salling He. Human cortical neural correlates of visual fatigue during binocular depth perception: An fNIRS study. *PLoS ONE*, 12(2):e0172426, 2017.

[142] Yuichi Yamashita, Atsuchi Maki, and Hideaki Koizumi. Near-infrared topographic measurement system: Imaging of absorbers localized in a scattering medium. *Review of Scientific Instruments*, 67:730, 1996.

[143] M A Franceschini, V Toronov, M E Filiaci, E Gratton, and S Fantini. On-line optical imaging of the human brain with 160-ms temporal resolution, 2000.

[144] S Fantini and A Sassaroli. Near-infrared optical mammography for breast cancer detection with intrinsic contrast. *Annals of Biomedical Engineering*, 40(2):398–407, 2012.

[145] R Ziegler, B Brendel, H Rinneberg, and T Nielsen. Investigation of detection limits for diffuse optical tomography systems: II. Analysis of slab and cup geometry for breast imaging, 2009.

[146] T Durduran, R Choe, J P Culver, L Zubkov, M J Holboke, J Giammarco, B Chance, and A G Yodh. Bulk optical properties of healthy female breast tissue. *Physics in Medicine and Biology*, 47(16):2847–2861, 2002.

[147] E E Vidal-Rosas, S A Billings, T Chico, and D Coca. Reproducibility of parameters of postocclusive reactive hyperemia measured by diffuse optical tomography, 2016.

[148] Haijing Niu, Sabin Khadka, Fenghua Tian, Zi-Jing Lin, Chunming Lu, Chaozhe Zhu, and Hanli Liu. Resting-state functional connectivity assessed with two diffuse optical tomographic systems. *Journal of biomedical optics*, 16(4):046006, 2011.

[149] T Durduran, R Choe, W B Baker, and A G Yodh. Diffuse optics for tissue monitoring and tomography. *Reports on Progress in Physics*, 73(7), 2010.

[150] A M Siegel, J J A Marota, and D A Boas. Design and evaluation of a continuous-wave diffuse optical tomography system, 1999.

[151] A T Eggebrecht, S L Ferradal, A Robichaux-Viehoever, M S Hassanpour, H Dehghani, A Z Snyder, T Hershey, and J P Culver. Mapping distributed brain function and networks with diffuse optical tomography, 2014.

[152] Richard J Grable, Steven L Ponder, Nikolaos A Gkanatsios, William Dieckmann, Patrick Olivier, Robert H Wake, and Yueping Zeng. Optical computed tomography for imaging the breast: First look. In *Proceedings of SPIE - The International Society for Optical Engineering*, volume 4082, pages 40–45, 2000.

[153] B W Pogue and K D Paulsen. High-resolution near-infrared tomographic imaging simulations of the rat cranium by use of a priori magnetic resonance imaging structural information. *Optics Letters*, 23(21):1716–1718, 1998.

[154] X Zhang, C Badea, M Jacob, and G A Johnson. Development of a noncontact 3-D fluorescence tomography system for small animal in vivo imaging. In *Progress in Biomedical Optics and Imaging - Proceedings of SPIE*, volume 7191, Dept. of Radiology, Duke University Medical Center, Durham, NC, United States, 2009.

[155] B W Pogue, T O McBride, U L Osterberg, and K D Paulsen. Comparison of imaging geometries for diffuse optical tomography of tissue, 1999.

[156] Dax Kepshire, Scott C Davis, Hamid Dehghani, Keith D Paulsen, and Brian W Pogue. Fluorescence tomography characterization for sub-surface imaging with protoporphyrin IX. *Optics Express*, 16(12):8581–8593, 2008.

[157] H Dehghani, S Sri Nivasan, B W Pogue, and A Gibson. Numerical modelling and image reconstruction in diffuse optical tomography. *Philosophical Transactions of the Royal Society A: Mathematical, Physical and Engineering Sciences*, 367(1900):3073–3093, 2009.

[158] S C Davis, K S Samkoe, J A O'Hara, S L Gibbs-Strauss, K D Paulsen, and B W Pogue. Comparing implementations of magnetic-resonance-guided fluorescence molecular tomography for diagnostic classification of brain tumors. *Journal of Biomedical Optics*, 15(5), 2010.

[159] D Kepshire, N Mincu, M Hutchins, J Gruber, H Dehghani, J Hypnarowski, F Leblond, M Khayat, and B W Pogue. A microcomputed tomography guided fluorescence tomography system for small animal molecular imaging. *Review of Scientific Instruments*, 80(4), 2009.

[160] F Leblond, H Dehghani, D Kepshire, and B W Pogue. Early-photon fluorescence tomography: Spatial resolution improvements and noise stability considerations. *Journal of the Optical Society of America A: Optics and Image Science, and Vision*, 26(6):1444–1457, 2009.

[161] M C W Van Rossum and Th.M. Nieuwenhuizen. Multiple scattering of classical waves: Microscopy, mesoscopy, and diffusion. *Reviews of Modern Physics*, 71(1):313–371, 1999.

[162] S L Jacques. Optical properties of biological tissues: A review. *Physics in Medicine and Biology*, 58(11):R37–R61, 2013.

[163] Brian C. Wilson and Steven L. Jacques. Optical reflectance and transmission of tissues: Principles and Applications. *IEEEJ Quantum Electron*, 26(12):2186–2199, 1990.

[164] C Dean Kurth and W S Thayer. A multiwavelength frequency-domain near-infrared cerebral oximeter. *Physics in Medicine and Biology*, 44(3):727–740, 1999.

[165] S.A. Prahl, M. Keijzer, S.L. Jacques, and A.J. Welch. A Monte Carlo model of light propagation in tissue. *SPIE Institute series*, IS(5):102–111, 1989.

[166] B C Wilson and G Adam. A Monte Carlo model for the absorption and flux distributions of light in tissue. *Medical Physics*, 10(6):824–830, 1983.

[167] N Cao, M Ortner, and A Nehorai. Solutions for diffuse optical tomography using the Feynman-Kac formula and interacting particle method. In *Progress in Biomedical Optics and Imaging - Proceedings of SPIE*, volume 6434, 2007.

[168] R F Bonner, R Nossal, S Havlin, and G H Weiss. Model for photon migration in turbid biological media. *Journal of the Optical Society of America. A, Optics and image science*, 4(3):423–432, 1987.

[169] A H Gandjbakhche, G H Weiss, R F Bonner, and R Nossal. Photon path-length distributions for transmission through optically turbid slabs. *Physical Review E*, 48(2):810–818, 1993.

[170] Rinat Ankri, Haim Taitelbaum, and Dror Fixler. On phantom experiments of photon migration model in tissues. *The open optics journal*, 5:28–32, 2011.

[171] F A Grunbaum. Diffuse tomography: The isotropic case. *Inverse Problems*, 8(3):409–419, 1992.

[172] Phaneendra Yalavarthy. *A generalized least-squares minimization method for near infrared diffuse optical tomography.* PhD thesis, Dartmouth College, 2007.

[173] D A Boas, M A O'Leary, B Chance, and A G Yodh. Scattering of diffuse photon density waves by spherical inhomogeneities within turbid media: Analytic solution and applications. In *Proceedings of the National Academy of Sciences of the United States of America*, volume 91, pages 4887–4891, 1994.

[174] S R Arridge, M Cope, and D T Delpy. The theoretical basis for the determination of optical pathlengths in tissue: temporal and frequency analysis. *Physics in medicine and biology*, 37(7):1531–60, 1992.

[175] F Martelli, A Sassaroli, Y Yamada, and G Zaccanti. Analytical approximate solutions of the time-domain diffusion equation in layered slabs. *Journal of the Optical Society of America A: Optics and Image Science, and Vision*, 19(1):71–80, 2002.

[176] J C J Paasschens. Solution of the time-dependent Boltzmann equation, 1997.

[177] Fabrizio Martelli, Angelo Sassaroli, Antonio Pifferi, Alessandro Torricelli, Lorenzo Spinelli, and Giovanni Zaccanti. Heuristic Green's function of the time dependent radiative transfer equation for a semi-infinite medium. *Optics Express*, 15(26):18168–18175, 2007.

[178] W. F. Ames. *Numerical Methods for Partial Differential Equations.* Computer science and scientific computing, Academic Press, New York, 3rd edition, 1992.

[179] B W Pogue, M S Patterson, H Jiang, and K D Paulsen. Initial assessment of a simple system for frequency domain diffuse optical tomography, 1995.

[180] A H Hielscher, A D Klose, and K M Hanson. Gradient-based iterative image reconstruction scheme for time-resolved optical tomography. *IEEE Transactions on Medical Imaging*, 18(3):262–271, 1999.

[181] A H Hielscher, R E Alcouffe, and R L Barbour. Comparison of finite-difference transport and diffusion calculations for photon migration in homogeneous and heterogeneous tissues. *Physics in Medicine and Biology*, 43(5):1285–1302, 1998.

[182] M Schweiger, S R Arridge, and D T Delpy. Application of the finite-element method for the forward and inverse models in optical tomography. *Journal of Mathematical Imaging and Vision*, 3(3):263–283, 1993.

[183] K D Paulsen and H Jiang. Spatially varying optical property reconstruction using a finite element diffusion equation approximation. *Medical Physics*, 22(6):691–701, 1995.

[184] H Gao and H Zhao. A fast-forward solver of radiative transfer equation. *Transport Theory and Statistical Physics*, 38(3):149–192, 2009.

[185] L D Montejo, H.-K.K. Kim, and A H Hielscher. A finite-volume algorithm for modeling light transport with the time-independent simplified spherical harmonics approximation to the equation of radiative transfer. In *Progress in Biomedical Optics and Imaging - Proceedings of SPIE*, volume 7896, 2011.

[186] V Y Soloviev, C D'Andrea, P Surya Mohan, G Valentini, R Cubeddu, and S R Arridge. Fluorescence lifetime optical tomography with discontinuous Galerkin discretisation scheme. *Biomedical Optics Express*, 1(3):998–1013, 2010.

[187] W Xie, Y Deng, L Lian, K Wang, Z Luo, and H Gong. Boundary element method for diffuse optical tomography. In *Proceedings - 2013 7th International Conference on Image and Graphics, ICIG 2013*, pages 5–8, 2013.

[188] F Fedele, M J Eppstein, J P Laible, A Godavarty, and E M Sevick-Muraca. Fluorescence photon migration by the boundary element method. *Journal of Computational Physics*, 210(1):109–132, 2005.

[189] A D Zacharopoulos, S R Arridge, O Dorn, V Kolehmainen, and J Sikora. Three-dimensional reconstruction of shape and piecewise constant region

values for optical tomography using spherical harmonic parametrization and a boundary element method. *Inverse Problems*, 22(5):1509–1532, 2006.

[190] S Srinivasan and H Ghadyani. 3-D Image-guided diffuse optical tomography using boundary element method and MPI implementation. In *Proceedings of the Annual International Conference of the IEEE Engineering in Medicine and Biology Society, EMBS*, pages 8452–8454, Thayer School of Engineering, Dartmouth College, 8000 Cummings Hall, Hanover, NH-03755, United States, 2011.

[191] Akira Ishimaru. *Wave Propagation and Scattering in Random Media*. Academic press New York, 1978.

[192] A D Klose and A H Hielscher. Optical tomography using the time-independent equation of radiative transfer-Part 2: Inverse model. *Journal of Quantitative Spectroscopy and Radiative Transfer*, 72(5):715–732, 2002.

[193] T Tarvainen, M Vauhkonen, V Kolehmainen, and J P Kaipio. Hybrid radiative-transfer-diffusion model for optical tomography. *Applied Optics*, 44(6):876–886, 2005.

[194] S R Arridge and J C Hebden. Optical imaging in medicine: II. Modelling and reconstruction. *Physics in Medicine and Biology*, 42(5):841–853, 1997.

[195] E D Aydin, C R E De Oliveira, and A J H Goddard. A comparison between transport and diffusion calculations using a finite element-spherical harmonics radiation transport method. *Medical Physics*, 29(9):2013–2023, 2002.

[196] R A J Groenhuis, H A Ferwerda, and J J Ten Bosch. Scattering and absorption of turbid materials determined from reflection measurements. 1: Theory, 1983.

[197] R A J Groenhuis and J J Ten Bosch. Scattering and absorption of turbid materials determined from reflection measurements. 2: Measuring method and calibration, 1983.

[198] M Keijzer, W M Star, and P R M Storchi. Optical diffusion in layered media, 1988.

[199] M Schweiger, S R Arridge, M Hiraoka, and D T Delpy. The finite element method for the propagation of light in scattering media: Boundary and source conditions. *Medical Physics*, 22(11 I):1779–1792, 1995.

[200] V Tsenova and E Stoykova. Refractive index measurement in human tissue samples. In *Proceedings of SPIE - The International Society for Optical Engineering*, volume 5226, pages 413–417, 2003.

[201] T J Farrell, M S Patterson, and B Wilson. A diffusion theory model of spatially resolved, steady-state diffuse reflectance for the noninvasive determination of tissue optical properties in vivo. *Medical Physics*, 19(4):879–888, 1992.

[202] S R Arridge, M Schweiger, M Hiraoka, and D T Delpy. A finite element approach for modeling photon transport in tissue. *Medical Physics*, 20(2 I):299–310, 1993.

[203] Richard C Haskell, Lars O Svaasand, Tsong-Tseh Tsay, Ti-Chen Feng, Matthew S McAdams, and Bruce J Tromberg. Boundary conditions for the diffusion equation in radiative transfer. *Journal of the Optical Society of America A: Optics and Image Science, and Vision*, 11(10):2727–2741, 1994.

[204] A H Hielscher, S L Jacques, L Wang, and F K Tittel. The influence of boundary conditions on the accuracy of diffusion theory in time-resolved reflectance spectroscopy of biological tissues. *Physics in Medicine and Biology*, 40(11):1957–1975, 1995.

[205] T Lister, P A Wright, and P H Chappell. Optical properties of human skin. *Journal of Biomedical Optics*, 17(9), 2012.

[206] V G Peters, D R Wyman, M S Patterson, and G L Frank. Optical properties of normal and diseases human breast tissues in the visible and near infrared. *Physics in Medicine and Biology*, 35(9):1317–1334, 1990.

[207] C Correia, K Jackson, J.-P. Véran, D Andersen, O Lardière, and C Bradley. Static and predictive tomographic reconstruction for wide-field multi-object adaptive optics systems. *Journal of the Optical Society of America A: Optics and Image Science, and Vision*, 31(1):101–113, 2014.

[208] Andhi Marjono, Akira Yano, Shinpei Okawa, Feng Gao, and Yukio Yamada. Total light approach of time-domain fluorescence diffuse optical tomography. *Optics Express*, 16(19):15268–15285, 2008.

[209] S R Arridge and M Schweiger. Photon-measurement density functions. Part 2: Finite-element-method calculations. *Applied Optics*, 34(34):8026–8037, 1995.

[210] F.J. Pettersen and J.O. Hogetveit. From 3D tissue data to impedance using Simpleware ScanFE+IP and Comsol Multiphysics - a tutorial. *Journal of Electrical Bioimpedance*, 2:13–32, 2011.

[211] Rachee Singh and Iven Jose. Diffuse Optical Tomography : A Simulation Based Approach. In *Proceedings of the COMSOL Conference 2011*, volume 1, 2011.

[212] P K Yalavarthy, H Dehghani, B W Pogue, and K D Paulsen. Critical computational aspects of near infrared circular tomographic imaging: Analysis of measurement number, mesh resolution and reconstruction basis. *Optics Express*, 14(13):293–307, 2006.

[213] P K Yalavarthy, D R Lynch, B W Pogue, H Dehghani, and K D Paulsen. Implementation of a computationally efficient least-squares algorithm for highly under-determined three-dimensional diffuse optical tomography problems, 2008.

[214] M Jermyn, H Ghadyani, M A Mastanduno, W Turner, S C Davis, H Dehghani, and B W Pogue. Fast segmentation and high-quality three-dimensional volume mesh creation from medical images for diffuse optical tomography. *Journal of Biomedical Optics*, 18(8), 2013.

[215] Paúl Leonardo Medina Vázquez. *Técnicas matemáticas para reconstrucción de imágenes de fluorescencia con aplicaciones en biomedicina*. PhD thesis, Universidad Carlos III de Madrid, 2009.

[216] Joseph R. Lakowikz. *Principles of fluorescence spectroscopy*. Springer Science & Business Media, 2007.

[217] Y Lin, H Gao, O Nalcioglu, and G Gulsen. Fluorescence diffuse optical tomography with functional and anatomical a priori information: Feasibility study. *Physics in Medicine and Biology*, 52(18):5569–5585, 2007.

[218] H Egger, M Freiberger, and M Schlottbom. Analysis of forward and inverse models in fluorescence optical tomography. *Aachen Institute for Advanced Study in Computational Engineering Science*, 2009.

[219] S C Davis, H Dehghani, J Wang, S Jiang, B W Pogue, and K D Paulsen. Image-guided diffuse optical fluorescence tomography implemented with Laplacian-type regularization. *Optics Express*, 15(7):4066–4082, 2007.

[220] Anne Koenig, Lionel Hervé, Véronique Josserand, Michel Berger, Jérôme Boutet, Anabela Da Silva, Jean-Marc Dinten, Philippe Peltié, Jean-Luc Coll, and Philippe Rizo. In vivo mice lung tumor follow-up with fluorescence diffuse optical tomography. *Journal of Biomedical Optics*, 13(1):11008–11009, 2008.

[221] Q Zhu, H Dehghani, K M Tichauer, R W Holt, K Vishwanath, F Leblond, and B W Pogue. A three-dimensional finite element model and image reconstruction algorithm for time-domain fluorescence imaging in highly scattering media. *Physics in Medicine and Biology*, 56(23):7419–7434, 2011.

[222] R L Barbour, H L Graber, J Chang, S.-L.S. Barbour, P C Koo, and R Aronson. MRI-Guided Optical Tomography: Prospects and Computation for a New Imaging Method, 1995.

[223] Tanja Tarvainen. *Computational methods for light transport in optical tomography*. PhD thesis, University of Kuopio, 2006.

[224] R J Gaudette, D H Brooks, C A DiMarzio, M E Kilmer, E L Miller, T Gaudette, and D A Boas. A comparison study of linear reconstruction techniques for diffuse optical tomographic imaging of absorption coefficient. *Physics in Medicine and Biology*, 45(4):1051–1070, 2000.

[225] B. Calvin-Shaw. *Development of novel reconstruction methods based on L1 minimization for near infrared diffuse optical tomography*. PhD thesis, Bangalore, India, 2012.

[226] Gregory Boverman. *Model-based approaches to the solution of the inverse problem for Diffuse Optical Tomography*. PhD thesis, Northeastern University, 2007.

[227] A H Hielscher, A D Klose, A K Scheel, B Moa-Anderson, M Backhaus, U Netz, and J Beuthan. Sagittal laser optical tomography for imaging of rheumatoid finger joints. *Physics in Medicine and Biology*, 49(7):1147–1163, 2004.

[228] H Ö Kazanci, T Mercan, and M Canpolat. Design and evaluation of a reflectance diffuse optical tomography system. *Optical and Quantum Electronics*, 47(2):257–265, 2014.

[229] R Roy and E M Sevick-Muraca. A numerical study of gradient-based nonlinear optimization methods for contrast enhanced optical tomography. *Optics Express*, 9(1):49–65, 2001.

[230] Martin Schweiger. *Application of the Finite Element Method in infrared image recontruction of scattering media*. PhD thesis, University College London, 1994.

[231] P K Yalavarthy, B W Pogue, H Dehghani, C M Carpenter, S Jiang, and K D Paulsen. Structural information within regularization matrices improves near infrared diffuse optical tomography. *Optics Express*, 15(13):8043–8058, 2007.

[232] M Guven, B Yazici, X Intes, and B Chance. Diffuse optical tomography with a priori anatomical information. In *Proceedings of SPIE - The International Society for Optical Engineering*, volume 4955, pages 634–646, Electrical and Computer Eng. Dept., Drexel University, Philadelphia, PA, United States, 2003.

[233] M Guven, B Yazici, X Intes, and B Chance. Hierarchical Bayesian algorithm for diffuse optical tomography. In *Proceedings - Applied Imagery Pattern Recognition Workshop*, volume 2005, pages 140–145, Electrical, Computer, and Systems Engineering Department, Rensselaer Polytechnic Institute, Troy, NY, United States, 2005.

[234] B Kanmani and R M Vasu. Diffuse optical tomography through solving a system of quadratic equations: Theory and simulations. *Physics in Medicine and Biology*, 51(4):981–998, 2006.

[235] M Chu and H Dehghani. Image reconstruction in diffuse optical tomography based on simplified spherical harmonics approximation. *Optics Express*, 17(26):24208–24223, 2009.

[236] Zhen Yuan, Jiang Zhang, Xiaodong Wang, and Changqing Li. A systematic investigation of reflectance diffuse optical tomography using nonlinear reconstruction methods and continuous wave measurements. *Biomedical optics express*, 5(9):3011–22, 2014.

[237] H Dehghani, B W Pogue, J Shudong, B Brooksby, and K D Paulsen. Three-dimensional optical tomography: Resolution in small-object imaging. *Applied Optics*, 42(16):3117–3128, 2003.

[238] K D Paulsen and H Jiang. Enhanced frequency-domain optical image reconstruction in tissues through total-variation minimization. *Applied Optics*, 35(19):3447–3458, 1996.

[239] B Brooksby, S Jiang, H Dehghani, B W Pogue, K D Paulsen, J Weaver, C Kogel, and S P Poplack. Combining near-infrared tomography and magnetic resonance imaging to study in vivo breast tissue: Implementation of a Laplacian-type regularization to incorporate magnetic resonance structure. *Journal of Biomedical Optics*, 10(5), 2005.

[240] H Gao, Y Lin, G Gulsen, and H Zhao. Fully linear reconstruction method for fluorescence yield and lifetime through inverse complex-source formulation: Simulation studies. *Optics Letters*, 35(11):1899–1901, 2010.

[241] T Correia, N Ducros, C D'Andrea, M Schweiger, and S Arridge. Quantitative fluorescence diffuse optical tomography in the presence of heterogeneities. *Optics Letters*, 38(11):1903–1905, 2013.

[242] Ihsan Mohd Yassin, Mohd Nasir Taib, and Ramli Adnan. Recent advancements & methodologies in system identification: A review. *Scientific Research Journal*, 1(1):14–33, 2013.

[243] E E Vidal-Rosas, S A Billings, Y Zheng, J E Mayhew, D Johnston, A J Kennerley, and D Coca. Reduced-order modeling of light transport in tissue for real-time monitoring of brain hemodynamics using diffuse optical tomography. *Journal of Biomedical Optics*, 19(2), 2014.

[244] A T Eggebrecht, B R White, S L Ferradal, Y Zhan, A Z Snyder, H Dehghani, and J P Culver. A quantitative spatial comparison of high-density diffuse optical tomography and fMRI cortical mapping, 2012.

[245] M J Saikia, K Rajan, and R M Vasu. 3-D GPU based real time Diffuse Optical Tomographic system. In *Souvenir of the 2014 IEEE International Advance Computing Conference, IACC 2014*, pages 1099–1103, Department of Physics, Indian Institute of Science, Bangalore, 560012, India, 2014.

[246] M J Saikia, R Kanhirodan, and R Mohan Vasu. High-speed GPU-based fully three-dimensional diffuse optical tomographic system. *International Journal of Biomedical Imaging*, 2014, 2014.

[247] Owen Yang, David Cuccia, and Bernard Choi. Real-time blood flow visualization using the graphics processing unit. *Journal of Biomedical Optics*, 16(1):016009, 2011.

[248] M Freiberger, H Egger, M Liebmann, and H Scharfetter. High-performance image reconstruction in fluorescence tomography on desktop computers and graphics hardware. *Biomedical Optics Express*, 2(11):3207–3222, 2011.

[249] M E Eames, B W Pogue, P K Yalavarthy, and H Dehghani. An efficient jacobian reduction method for image reconstruction using diffuse optical tomography. In *Biomedical Optics, BIOMED 2008*, School of Physics, University of Exeter, Stocker Road, United Kingdom, 2008.

[250] S Wojtkiewicz, T Durduran, and H Dehghani. Time-resolved near infrared light propagation using frequency domain superposition, 2018.

[251] S Chen, S A Billings, C F Cowan, and P M Grant. Practical identification of narmax models using radial basis functions, 1990.

[252] E E Vidal-Rosas. *Advanced tomographic reconstruction methods for diffuse optical imaging of cerebral haemodynamic response.* PhD thesis, The University of Sheffield, 2011.

[253] P G Young, T B H Beresford-West, S R L Coward, B Notarberardino, B Walker, and A Abdul-Aziz. An efficient approach to converting three-dimensional image data into highly accurate computational models. *Philosophical Transactions of the Royal Society A: Mathematical, Physical and Engineering Sciences*, 366(1878):3155–3173, 2008.

[254] SA Billings, S Chen, and MJ Korenberg. Identification of MIMO non-linear systems using a forward-regression orthogonal estimator. *International Journal of Control*, 49(6):2157–2189, 1989.

[255] S Chen, S A Billings, and W Luo. Orthogonal least squares methods and their application to non-linear system identification. *International Journal of Control*, 50(5):1873–1896, 1989.

[256] S Brigadoi, S Powell, R J Cooper, L A Dempsey, S Arridge, N Everdell, J Hebden, and A P Gibson. Evaluating real-time image reconstruction in diffuse optical tomography using physiologically realistic test data. *Biomedical Optics Express*, 6(12):4719–4736, 2015.

[257] H Dehghani, B W Pogue, S P Poplack, and K D Paulsen. Multiwavelength three-dimensional near-infrared tomography of the breast: Initial simulation, phantom, and clinical results, 2003.

[258] A X Cong and G Wang. A finite-element-based reconstruction method for 3D fluorescence tomography. *Optics Express*, 13(24):9847–9857, 2005.

[259] N Ducros, A Da Silva, J M Dinten, and F Peyrin. Fluorescence diffuse optical tomography: A simulation-based study comparing time-resolved and continuous wave reconstructions performances. In *2008 5th IEEE International Symposium on Biomedical Imaging: From Nano to Macro, Proceedings, ISBI*, pages 388–391, 2008.

[260] R C Benson and H A Kues. Fluorescence properties of indocyanine green as related to angiography. *Physics in Medicine and Biology*, 23(1):159–163, 1978.

[261] B Yuan, N Chen, and Q Zhu. Emission and absorption properties of indocyanine green in Intralipid solution. *Journal of Biomedical Optics*, 9(3):497–503, 2004.

[262] Thomas D O'Sullivan, Albert E Cerussi, David J Cuccia, and Bruce J Tromberg. Diffuse optical imaging using spatially and temporally modulated light. *Journal of Biomedical Optics*, 17(7):713111, 2012.

[263] Matteo Caffini, Davide Contini, Rebecca Re, Lucia M Zucchelli, Rinaldo Cubeddu, Alessandro Torricelli, and Lorenzo Spinelli. Functional Near Infrared Spectroscopy and Diffuse Optical Tomography in Neuroscience. In *Advances in Brain Imaging*, pages 51–76. 2012.

[264] D A Boas, A M Dale, and M A Franceschini. Diffuse optical imaging of brain activation: Approaches to optimizing image sensitivity, resolution, and accuracy. *NeuroImage*, 23(SUPPL. 1):S275–S288, 2004.

[265] Sylvain Gioux, Amaan Mazhar, Bernard T Lee, Samuel J Lin, Adam M Tobias, David J Cuccia, Alan Stockdale, Rafiou Oketokoun, Yoshitomo Ashitate, Edward Kelly, Maxwell Weinmann, Nicholas J Durr, Lorissa a

Moffitt, Anthony J Durkin, Bruce J. Tromberg, and John V Frangioni. First-in-human pilot study of a spatial frequency domain oxygenation imaging system. *Journal of biomedical optics*, 16(8):086015, 2011.

[266] D J Cuccia, F Bevilacqua, A Li, A J Durkin, R Frostig, and B J Tromberg. Modulated imaging: Advancements in diffuse optical tomography and spectroscopy. In *Optics InfoBase Conference Papers*, Beckman Laser Institute, University of California, Irvine, United States, 2006.

[267] J R Weber, D J Cuccia, F Ayers, J S You, A J Durkin, and B J Tromberg. Towards functional optical imaging in layered tissues using modulated imaging. In *Optics InfoBase Conference Papers*, Beckman Laser Institute, University of California, Irvine, United States, 2006.

[268] J R Weber, D J Cuccia, and B J Tromberg. Modulated imaging in layered media. In *Annual International Conference of the IEEE Engineering in Medicine and Biology - Proceedings*, pages 6674–6676, Beckman Laser Institute and Medical Clinic, University of California, Irvine, Irvine, CA 92692, United States, 2006.

[269] M van de Giessen, J P Angelo, and S Gioux. Real-time, profile-corrected single snapshot imaging of optical properties. *Biomedical Optics Express*, 6(10):4051–4062, 2015.

[270] Rolf B. Saager, Alex Truong, David J. Cuccia, and Anthony J. Durkin. Method for depth-resolved quantitation of optical properties in layered media using spatially modulated quantitative spectroscopy. *Journal of biomedical optics*, 16(7):077002, 2011.

[271] Rolf B. Saager, Clement Kondru, Kendrew Au, Kelly Sry, Frederick Ayers, and Anthony J. Durkin. Multilayer silicone phantoms for the evaluation of quantitative optical techniques in skin imaging. In *SPIE 7567, Design and Performance Validation of Phantoms Used in Conjunction with Optical Measurement of Tissue II*, volume 7567, pages 756706–756706–8, 2010.

[272] J R Weber, D J Cuccia, A J Durkin, and B J Tromberg. Noncontact imaging of absorption and scattering in layered tissue using spatially modulated structured light. *Journal of Applied Physics*, 105(10), 2009.

[273] J R Weber, D J Cuccia, W R Johnson, G H Bearman, A J Durkin, M Hsu, A Lin, D K Binder, D Wilson, and B J Tromberg. Multispectral imaging

of tissue absorption and scattering using spatial frequency domain imaging and a computed-tomography imaging spectrometer. *Journal of Biomedical Optics*, 16(1):11015, 2011.

[274] Adrien Ponticorvo, Eren Taydas, Amaan Mazhar, Thomas Scholz, Hak-Su Kim, Jonathan Rimler, Gregory R D Evans, David J Cuccia, and Anthony J Durkin. Quantitative assessment of partial vascular occlusions in a swine pedicle flap model using spatial frequency domain imaging. *Biomedical Optics Express*, 4(2):298–306, 2013.

[275] Amr Yafi, Thomas S Vetter, Thomas Scholz, Sarin Patel, Rolf B Saager, David J Cuccia, Gregory R Evans, and Anthony J Durkin. Postoperative Quantitative Assessment of Reconstructive Tissue Status in Cutaneous Flap Model using Spatial Frequency Domain Imaging. *Plastic and reconstructive surgery*, 127(1):117–130, jan 2011.

[276] Ashley M Laughney, Venkataramanan Krishnaswamy, Elizabeth J Rizzo, Mary C Schwab, Richard J Barth, David J Cuccia, Bruce J Tromberg, Keith D Paulsen, Brian W Pogue, and Wendy A Wells. Spectral discrimination of breast pathologies in situ using spatial frequency domain imaging. *Breast Cancer Research*, 15(4):R61, 2013.

[277] Ashley M Laughney, Venkataramanan Krishnaswamy, Tyler B Rice, David J Cuccia, Richard J Barth, Bruce J Tromberg, Keith D Paulsen, Brian W Pogue, and Wendy A Wells. System analysis of spatial frequency domain imaging for quantitative mapping of surgically resected breast tissues. *Journal of Biomedical Optics*, 18(3):036012, 2013.

[278] Sylvain Gioux, Amaan Mazhar, David J. Cuccia, Anthony J. Durkin, Bruce J. Tromberg, and John V. Frangioni. Three-Dimensional Surface Profile Intensity Correction for Spatially-Modulated Imaging. *Journal of biomedical optics*, 14(3):034045, 2009.

[279] Soren D Konecky, Amaan Mazhar, David Cuccia, Anthony J Durkin, John C Schotland, and Bruce J Tromberg. Quantitative optical tomography of sub-surface heterogeneities using spatially modulated structured light. *Optics express*, 17(17):14780–90, 2009.

[280] Jin Chen, Vivek Venugopal, Frederic Lesage, and Xavier Intes. Time-resolved diffuse optical tomography with patterned-light illumination and detection. *Optics letters*, 35(13):2121–2123, 2010.

[281] Cosimo D'Andrea, Nicolas Ducros, Andrea Bassi, Simon Arridge, and Gianluca Valentini. Fast 3D optical reconstruction in turbid media using spatially modulated light. *Biomedical Optics Express*, 1(2):471–481, 2010.

[282] Y Zhou, K K H Chan, T Lai, and S Tang. Characterizing refractive index and thickness of biological tissues using combined multiphoton microscopy and optical coherence tomography. *Biomedical Optics Express*, 4(1):38–50, 2013.

[283] S Bélanger, M Abran, X Intes, C Casanova, and F Lesage. Real-time diffuse optical tomography based on structured illumination. *Journal of Biomedical Optics*, 15(1), 2010.

[284] Nicolas Ducros, Cosimo D'Andrea, Andrea Bassi, Gianluca Valentini, and Simon Arridge. A virtual source pattern method for fluorescence tomography with structured light. *Physics in Medicine and Biology*, 57(12):3811, 2012.

[285] Rolf B. Saager, David J. Cuccia, Steve Saggese, Kristen M. Kelly, and Anthony J. Durkin. Quantitative fluorescence imaging of protoporphyrin IX through determination of tissue optical properties in the spatial frequency domain. *Journal of Biomedical Optics*, 16(12):126013, 2011.

[286] Amaan Mazhar, David J Cuccia, Sylvain Gioux, Anthony J Durkin, John V Frangioni, and Bruce J Tromberg. Structured illumination enhances resolution and contrast in thick tissue fluorescence imaging. *Journal of biomedical optics*, 15(February):010506, 2010.

[287] Marco Pilz, Sibylle Honold, and Alwin Kienle. Determination of the optical properties of turbid media by measurements of the spatially resolved reflectance considering the point-spread function of the camera system. *Journal of Biomedical Optics*, 13(5):054047, 2008.

[288] David J Cuccia, Frederic Bevilacqua, Anthony J Durkin, Frederick R Ayers, and Bruce J Tromberg. Quantitation and mapping of tissue optical properties using modulated imaging. *Journal of Biomedical Optics*, 14(2):024012, 2009.

[289] N Dögnitz and G Wagnières. Determination of tissue optical properties by steady-state spatial frequency-domain reflectometry. *Lasers in Medical Science*, 13(1):55–65, 1998.

[290] P K Yalavarthy, B W Pogue, H Dehghani, and K D Paulsen. Weight-matrix structured regularization provides optimal generalized least-squares estimate in diffuse optical tomography. *Medical Physics*, 34(6):2085–2098, 2007.

[291] A Mazhar, S Dell, D J Cuccia, S Gioux, A J Durkin, J V Frangioni, and B J Tromberg. Wavelength optimization for rapid chromophore mapping using spatial frequency domain imaging. *Journal of Biomedical Optics*, 15(6), 2010.

[292] A Bassi, D J Cuccia, A J Durkin, and B J Tromberg. Spatial shift of spatially modulated light projected on turbid media. *Journal of the Optical Society of America A: Optics and Image Science, and Vision*, 25(11):2833–2839, 2008.

[293] Rolf B Saager, David J Cuccia, and Anthony J Durkin. Determination of optical properties of turbid media spanning visible and near-infrared regimes via spatially modulated quantitative spectroscopy. *Journal of biomedical optics*, 15(1):017012, 2014.

[294] X Cheng and D A Boas. Diffuse optical reflection tomography with continuous-wave illumination. *Optics Express*, 3(3):118–123, 1998.

[295] F Fantoni, L Hervé, V Poher, S Gioux, J I Mars, and J M Dinten. Background fluorescence reduction and absorption correction for fluorescence reflectance imaging. In *Progress in Biomedical Optics and Imaging - Proceedings of SPIE*, volume 8935, CEA, Leti, MINATEC Campus, 17 rue des Martyrs, F38054 Grenoble, cedex 9, France, 2014.

[296] Dax S Kepshire, Scott C Davis, Hamid Dehghani, Keith D Paulsen, and Brian W Pogue. Subsurface diffuse optical tomography can localize absorber and fluorescent objects but recovered image sensitivity is nonlinear with depth. *Applied Optics*, 46(10):1669–1678, 2007.

[297] Dax S. Kepshire. *Sub-surface diffuse fluorescence tomography: system development and feasibility studies*. PhD thesis, Dartmouth College, 2006.

[298] H Obrig. NIRS in clinical neurology - a 'promising' tool?, 2014.

[299] X Wu, A T Eggebrecht, S L Ferradal, J P Culver, and H Dehghani. Fast and efficient image reconstruction for high density diffuse optical imaging of the human brain, 2015.

[300] P Pinti, C Aichelburg, S Gilbert, A Hamilton, J Hirsch, P Burgess, and I Tachtsidis. A Review on the Use of Wearable Functional Near-Infrared Spectroscopy in Naturalistic Environments, 2018.

[301] H Zhao and R J Cooper. Review of recent progress toward a fiberless, whole-scalp diffuse optical tomography system, 2018.

[302] Y Zhan, A T Eggebrecht, J P Culver, and H Dehghani. Image quality analysis of high-density diffuse optical tomography incorporating a subject-specific head model, 2012.

[303] S Fantini, B Frederick, and A Sassaroli. Perspective: Prospects of non-invasive sensing of the human brain with diffuse optical imaging, 2018.

[304] P Pinti, C Aichelburg, F Lind, S Power, E Swingler, A Merla, A Hamilton, S Gilber, P Burgess, and I Tachtsidis. Using fiberless, wearable fnirs to monitor brain activity in real-world cognitive tasks, 2015.

[305] M Schweiger. GPU-accelerated finite element method for modelling light transport in diffuse optical tomography, 2011.

[306] T Dragojević, H M Varma, J L Hollmann, C P Valdes, J P Culver, C Justicia, and T Durduran. High-density speckle contrast optical tomography (SCOT) for three dimensional tomographic imaging of the small animal brain, 2017.

[307] H M Varma, C P Valdes, A K Kristoffersen, J P Culver, and T Durduran. Speckle contrast optical tomography: A new method for deep tissue three-dimensional tomography of blood flow, 2014.